

**Thermo-Hydro-Mechanical
Processes in the Nearfield
around a HLW Repository
in Argillaceous Formations**

Volume II
**In-situ-Investigations and
Interpretative Modelling**



Gesellschaft für Anlagen-
und Reaktorsicherheit
(GRS) mbH

**Thermo-Hydro-Mechanical
Processes in the Nearfield
around a HLW Repository
in Argillaceous Formations**

Volume II
**In-situ-Investigations and
Interpretative Modelling**
May 2007 to May 2013

Chun-Liang Zhang
Oliver Czaikowski
Michael Komischke
Klaus Wieczorek

June 2014

Remark:

This report was prepared under contract No. 02 E 10377 with the German Federal Ministry of Economics and Technology (BMWi).

The work was conducted by the Gesellschaft für Anlagen- und Reaktorsicherheit (GRS) mbH.

The authors are responsible for the content of this report.

GRS - 313
ISBN 978-3-939355-92-2

Keywords

Bure, Clay Host Rock, In-situ Measurements, Mont Terri, THM-coupled Modelling, Validation Process

Foreword

Deep disposal of heat-emitting high-level radioactive waste (HLW) in clay formations will inevitably induce thermo-hydro-mechanical-chemical disturbances to the host rock and engineered barriers over very long periods of time. The responses and resulting property changes of the natural and engineered barriers are to be well understood, characterized, and predicted for assessing the long-term performance and safety of the repositories.

In accordance with the R&D programme defined by the German Federal Ministry of Economics and Technology (BMWi), GRS has intensively performed site-independent research work on argillaceous rocks during the last decade. Most of the investigations have been carried out on the Callovo-Oxfordian argillite and the Opalinus clay by participation in international research projects conducted at the underground research laboratories at Bure in France (MHM-URL) and Mont-Terri in Switzerland (MT-URL). The THM-TON project, which was funded by BMWi under contract number 02E10377, investigated the THM behaviours of the clay host rock and clay-based backfill/sealing materials with laboratory tests, in situ experiments and numerical modelling.

The clay rocks were experimentally studied with respect to the following THM behaviour:

- Short-term deformation, damage and induced permeability change, which will be produced by excavation of a repository;
- Long-term deformation, which controls the closure process of the repository openings and the integrity of the geological and engineered barriers;
- Swelling capability, which may dominate the long-term sealing process of the damaged zone surrounding the openings when water arrives;
- Self-sealing of fractures in the damaged zone, which is presently one of the highest concerns in the assessment of the long-term performance and safety of the repository because it has direct impact on the hydraulics and mechanics in the nearfield;
- Thermal impact on the hydro-mechanical behaviour and the integrity of the natural host rock and engineered barriers.

Excavated claystone and claystone-bentonite mixtures were characterized as backfill and sealing materials with regard to the barrier functions in repositories:

- Compaction behaviour of the backfill/sealing materials, which controls the interactions with support linings and the surrounding rock, and also determines the evolution of the backfill porosity and hydraulic conductivity;
- Permeability in relation with porosity, which controls the fluid transport and thus the hydraulic long-term barrier function of the backfill;
- Water retention capacity, which influences the water saturation process and storage, water/gas two-phase flow, and buildup of swelling pressure in the backfill and seals;
- Swelling pressure in compacted claystone-bentonite mixtures is required for sealing of possibly remaining gaps within the seals and seal/rock interfaces and for supporting the surrounding rock against damage propagation;
- Thermal conductivity of buffer surrounding HLW containers, which controls the heat transfer and temperature distribution in the multi-barrier-system.

In the frame of the Mine-By (MB) experiment in the MT-URL, the hydro-mechanical responses of the Opalinus clay to the excavation of the gallery G08 was monitored with measurement of porewater pressure in the surrounding rock. Additionally, the long-term deformation of a borehole and the porewater pressure in the surrounding rock (DM-A experiment) were also measured.

The coupled hydro-mechanical processes in the Opalinus clay during the in situ experiments were simulated using the finite element programme CODE_BRIGTH developed by the Technical University of Catalonia (UPC) in Barcelona. In addition to that, the coupled thermo-hydro-mechanical processes occurring in the Callovo-Oxfordian argillite during a heating experiment conducted by ANDRA at the MHM-URL were also modelled.

The in situ experiments and the numerical modelling work are summarized in this second volume, while the most important results and conclusions from the laboratory investigations on the clay rocks and clay-based backfill/sealing materials have been already reported in volume 1.

Table of contents

1	Introduction.....	1
1.1	THM processes in the nearfield of a HLW repository	1
1.1.1	Key processes during the operation phase	1
1.1.2	Key processes during the post-closure phase.....	3
1.2	Research programme and objectives.....	5
2	Mont Terri Rock Laboratory	9
2.1	Site description	9
2.2	Pore water pressure measurements during Gallery 08 excavation	12
2.2.1	Test design.....	12
2.2.2	Test procedure	14
2.2.3	Measurement results	15
2.2.4	Conclusions drawn from the in-situ experiment.....	18
2.3	Mine-by (MB) experiment.....	18
2.3.1	Test design.....	19
2.3.2	Test procedure	21
2.3.3	Measurement results	22
2.3.4	Conclusions drawn from the in situ-experiment.....	30
2.4	EZ-G experiment	30
2.4.1	Test design.....	31
2.4.2	Test procedure	33
2.4.3	Measurement results	33
2.4.4	Conclusions drawn from the in situ-experiment.....	38
2.5	DM-A experiment.....	38
2.5.1	Test design.....	38
2.5.2	Test procedure	39
2.5.3	Measurement results	40
2.5.4	Conclusions drawn from the in situ-experiment.....	43

3	Meuse/Haute-Marne underground research laboratory	45
3.1	Site description	45
3.2	Test Design of the second in-situ heating experiment (TED)	48
3.3	Test procedure	49
3.4	Measurement results	50
3.5	Conclusions drawn from the in-situ-experiment	61
4	Modelling.....	63
4.1	Physical modelling	63
4.1.1	Theoretical framework	63
4.1.2	Balance equations	64
4.1.3	Equilibrium restrictions.....	65
4.1.4	Constitutive equations	66
4.1.5	Material parameters.....	70
4.2	MB experiment	72
4.2.1	Numerical model.....	72
4.2.2	Modelling results.....	73
4.2.3	Modelling calibration and interpretative calculations	74
4.3	EZ-G experiment	76
4.3.1	Numerical model.....	76
4.3.2	Modelling results.....	78
4.3.3	Model calibration and interpretative calculations.....	82
4.4	DM-A experiment.....	84
4.4.1	Numerical model.....	84
4.4.2	Modelling results.....	85
4.4.3	Model calibration and interpretative calculations.....	88
4.5	TED experiment.....	91
4.5.1	Numerical model.....	91
4.5.2	Modelling results.....	93
4.5.3	Model calibration and interpretative calculations.....	95
4.6	Conclusions drawn from physical modelling and numerical simulation...	105

Summary and conclusions	107
Acknowledgement	109
References	111
List of Tables	117
List of Figures.....	119

1 Introduction

All over the world, clay formations are being investigated as host medium for geologic disposal of radioactive waste because of their favourable properties, such as very low hydraulic conductivity against fluid transport, good sorption capacity for retardation of radionuclides, and high potential of self-sealing of fractures. The construction of a repository, the disposal of heat-emitting high-level radioactive waste (HLW), the backfilling and sealing of the remaining voids, however, will inevitably induce mechanical (M), hydraulic (H), thermal (T) and chemical (C) disturbances to the host formation and the engineered barrier system (EBS) over very long periods of time during the operation and post-closure phases of the repository. The responses and resulting property changes of the clay host rock and engineered barriers are to be well understood, characterized, and predicted for assessing the long-term performance and safety of the repository.

1.1 THM processes in the nearfield of a HLW repository

According to the French and Swiss disposal concepts designed by ANDRA /AND 05/ and NAGRA /NAG 02/, respectively, the potential repositories will be located in the over-consolidated Callovo-Oxfordian and Opalinus argillaceous formations at depths of 500 to 650 m below the ground surface. The corresponding lithostatic stress is in a range of 12 to 18 MPa. The highly-indurated clay rocks are initially saturated with formation water. The designed thermal load from HLW is limited below 90 °C in the host rock. The repository openings will be backfilled and sealed with suitable materials. The main functions of the EBS are to stabilize the repository structures and to prevent release of radionuclides into the biosphere. The design of the repository systems is site dependent. During the repository operation and post-closure phases, complex THMC coupled processes will take place in the natural and engineered barriers. Key processes in the nearfield around a HLW disposal borehole are schematically illustrated in Fig. 1.1 for the operation and post-closure phases. The processes affect the properties of the host rock and the EBS.

1.1.1 Key processes during the operation phase

The operation phase is initiated with excavation of the access shafts, drifts and boreholes and lasts until the closure of a repository. Excavation leads to a redistribution of

the rock stress and the porewater pressure around the openings, particularly to a sharp gradient of the pore pressure and a high concentration of the deviatoric stress near the opening walls after relief of the radial stress component. This results in micro- and macro-fractures in the surrounding rock where the damage and failure criteria of the rock are violated. According to, /DAV 03/, /TSA 05/, the perturbed area may be divided into two zones: excavation damaged zone (EDZ) and disturbed zone (EdZ). The hydraulic conductivity of the EDZ near the opening walls may increase by several orders of magnitude up to the point where the barrier function of the host rock with respect to radionuclide migration will be affected. The EdZ outside the EDZ will be disturbed but less damaged without significant changes in flow and transport properties. Convergence of the openings and damage intensity and extent of the EDZ/EdZ are mainly dependent on the mechanical properties of the rock mass, depth of the excavation or local stress state, applied excavation technology, opening size and geometry, and support measures (shotcrete, bolting, steel arches, concrete lining, etc.). The rock deformation and damage develop with time. Moreover, the anisotropic nature of the sedimentary clay rocks and the anisotropic stress state has also considerable influences on the development of the EDZ/EdZ.

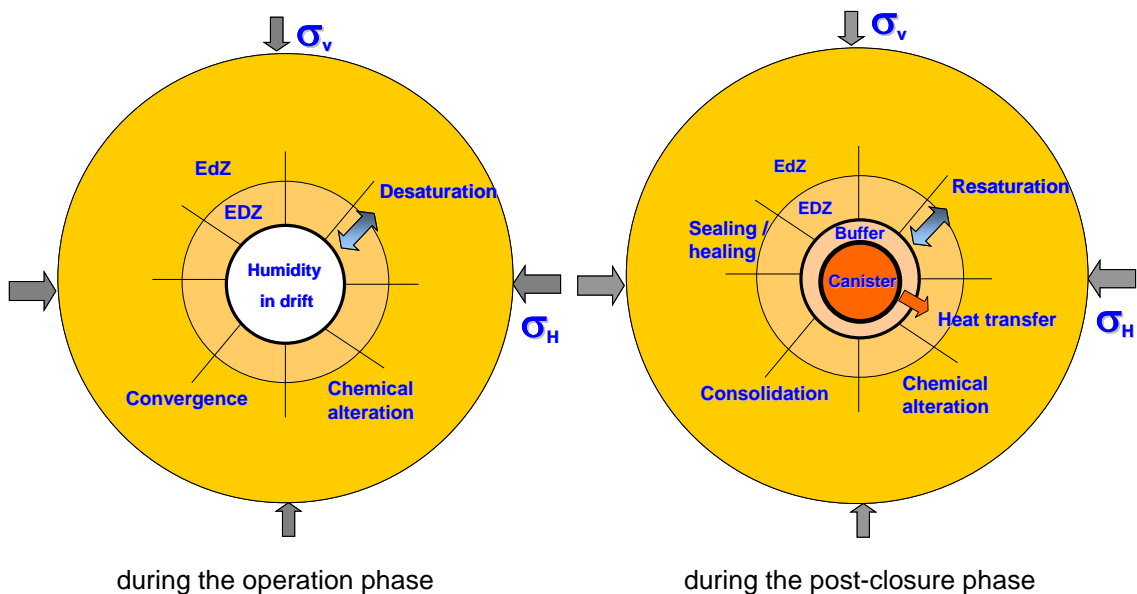


Fig. 1.1 Coupled THM processes in the nearfield around a HLW disposal borehole

The repository openings in deep clay formations normally need to be supported to limit the convergence and the EDZ propagation. The rock-support interaction leads to buildup of back-pressure against the rock deformation and damage. During the opera-

tion phase, the openings will be ventilated. The relatively low humidity of the circulating air will cause desaturation of the surrounding rock. Desaturation in turn gives rise to capillary forces and hence an increase in cohesion and strengthening of the rock mass, while at the same time the release of bound porewater results in collapse of the pore structure and generates microcracks propagating along bedding planes mainly. As stress-bearing element, the release of bound porewater also causes a change in the stress state in the rock mass.

After emplacement of HLW containers and backfilling of the disposal cells decay heat from the waste is transferred away through the buffer to the nearfield rock and then to the farfield. Heating will induce complex THMC processes in the EBS and the host rock. Heating accelerates the rheological deformation of the rock into the openings. For openings supported by rigid linings, a high pressure may build up on the linings. A sufficient thermal resistance of the linings is needed. Heating will cause a transient buildup of excess porewater pressure in the saturated nearfield, reducing the local effective mean stress. In the extreme case when the local minimum principal stress is exceeded, rock fracturing may occur. At high temperatures, the porewater in the buffer and the surrounding rock will evaporate and become more mobile, so that the water migration in liquid and gas phase will be accelerated. Additionally, heating may also affect the properties of the buffer and rock materials, such as transition of clay minerals, alteration of swelling capacity, thermally-induced consolidation and hence increase in stiffness and strength. In spite of these effects the barrier functions of the natural and engineered barriers have to be kept up.

Finally, the boreholes, drifts and shafts will be sealed with plugs consisting of compacted clay-based mixtures and concrete to prevent access of groundwater to the repository and releases of radionuclides via drifts and shafts. Certain degrees of mechanical stiffness and strength, swelling capability during wetting, and low hydraulic conductivity of the seals/plugs enhance the sealing and healing process of the surrounding EDZ/EdZ and hence provide a water-tight sealing system. The whole operation phase could last for a period of time in the order of 100 years /BOC 10/.

1.1.2 Key processes during the post-closure phase

After closing the repository, the THMC processes in the EBS and the host rock will continue. The support system of the openings will degrade gradually. Under effects of wa-

ter pressure gradients in the saturated rock and suction potentials in the unsaturated backfill, the formation water will move toward the backfilled openings, resulting in a re-saturation process in the EDZ and the backfill. With increasing water content, clay minerals in the clay rock and the clay-based backfill tend to swelling. The pre-existing fractures in the EDZ and the large pores in the backfill will be sealed and swelling pressure may build up, mainly depending on the amount of expansive clay minerals, water saturation, and density or porosity of the backfill/seal materials and the host rock. Additionally, wetting also results in weakening of the clay rock and accelerates the rock creep deformation into the backfilled openings. The hydro-mechanical processes and the interactions between the backfill, the support lining, the EDZ, and the farfield rock, enhance the consolidation of the EDZ and the porous backfill materials and thus the confining function of the whole multi-barrier-system. In the nearfield around HLW containers, thermal impact on the processes is one of the most important concerns for the long-term safety assessment of a repository. Thermally-accelerated rock deformation and porewater migration may enhance the compaction of the EDZ and the backfill. With time, the heated rock and backfill are cooling down to the original rock temperature. The hydro-mechanical processes will become slower and tend to a new steady state. Establishment of a new equilibrium in a repository will take a very long time of tens of thousands of years.

Water resaturation may cause long-term geochemical processes in the nearfield involving EDZ, buffer, waste containers, and other support/lining materials. Dissolution of chemical species, their transport, and precipitation may occur, creating potentially a “geochemical damage zone – GDZ” /TSA 12/.

Degradation and corrosion of the metallic components and containers will produce gas. Gas may migrate preferably through the porous backfill, the re-sealed EDZ, and the interfaces between them. Gas migration may be controlled by advection-diffusion of dissolved gas, two-phase flow, dilatancy-controlled flow, and flow in macroscopic tensile fractures /MAR 08/, /BOC 10/, FOR 13/. The last gas migration mechanism is only possible when the gas pressure becomes sufficiently high to generate fractures. Nevertheless, the gas production and migration has to be verified so that the integrity of the multi-barrier system is not impaired.

Generally, progressive closure of repositories in clay formations is to be expected due to creep of the surrounding host rock. Consolidation of both the EDZ and the backfill will lead to permanent confinement of the radioactive waste from the biosphere.

1.2 Research programme and objectives

For the last two decades, the feasibility of the disposal concepts has been intensively investigated in the Underground Research Laboratories (URLs) in the Callovo-Oxfordian argillite at Meuse-/Haute-Marne in France (MHM-URL) and in the Opalinus clay at Mont-Terri in Switzerland (MT-URL). The most important scientific activities are the investigations of the THMC properties and processes of the natural and engineered barriers by large/full-scale experiments under realistic repository conditions. The in situ experiments are supported by laboratory tests on samples for providing robust data-base for the host rock and the backfill/seal. On the basis of the knowledge from the experiments, constitutive models and computing codes have been developed for prediction of the coupled processes in the multi-barrier system. Results of the investigations serve as input for the long-term safety assessments of the potential repositories. GRS has participated in a great number of the international research projects in accordance with the German R&D programme /BMW 07/.

Following “Dossier 2005” /AND 05/, in which the most important outcomes of ANDRA’s programme during the time period from 1999 to 2005 are summarized and evaluated, ANDRA launched a new geomechanical laboratory programme (called GL-programme) in early 2007 /AND 06/, /DEL 09/, /LEB 10/. The general objective of this programme is to provide more comprehensive and realistic models of the repository behaviour for the operation and the post-closure periods. It was divided into the following sub-objectives.

For the operating phase:

- Quantification of the efficiency of support bolts from excavation through to possible removal of lining, taking anchor and rock behaviour into account;
- Characterization of hydro-mechanical disturbance resulting from excavation and their evolution until the end of the operation phase;
- Characterization of the effects of the rheological deformation of the clay host rock (creep, micro-mechanisms, constitutive models);
- Determination of the conceptual model of the EDZ around the openings;
- Modelling of damage and rupture location (intensity and extent of the EDZ).

For the post-closure phase:

- Description of various physical and chemical processes of deformation taking hydrological conditions into account;
- Evaluation of the macroscopic deformation rate on the basis of the various deformation mechanisms;
- Clarification of relationships between long-term deformation and damage;
- Quantification of the thermal effects on rock behaviour;
- Quantification of mechanical and hydraulic sealing of the EDZ.

For the interactions between the host rock and EBS components:

- Characterisation of the swelling and transport properties and nonsaturated hydro-mechanical properties of compacted claystone backfill under consideration of effects of cementitious water and backfill installation techniques;
- Specification of the geotechnical properties of the backfill under consideration of effects of alkaline disturbance and long-term rock behaviour;
- Model prediction of the long-term performance of a drift in the potential repository involving the major phenomena of rock-plug interaction, alkaline disturbance, effects on fluid transport, and impact on the long-term safety.

As a partner, GRS has contributed to the ANDRA's GL-programme with the THM-TON research project funded by the German Federal Ministry of Economics and Technology (BMWi) under contract 02E10377 /THM 07/. At that time, a mine-by experiment was also foreseen to be conducted by excavation of a new gallery G08 in the MT-URL to investigate hydro-mechanical responses of the Opalinus clay to excavation /TD 06/.

The first part of the THM-TON programme was carried out from May 2007 to May 2013 with laboratory experiments, in situ measurements and numerical modelling covering most of the objectives mentioned above:

- Laboratory investigations on the Callovo-Oxfordian and Opalinus clay rocks
 - Examination of effective stress and swelling pressure in indurated clay rock by taking bound porewater into account

- Short-term deformation, damage and induced permeability change in the clay host rock, which will be produced by excavation of a repository
- Long-term deformation of the clay host rock, which controls the closure process of the repository openings and the integrity of the geological and engineered barriers
- Swelling capability of the clay host rock, which may dominate the sealing process of the EDZ when water flows through
- Recovery and self-sealing of fractures in the clay host rock, which is one of the most concerns in the assessment of the long-term performance and safety of the repository
- Thermal impact on the hydro-mechanical behaviour and the integrity of the clay host rock
- Laboratory investigations on excavated claystone and claystone-bentonite mixtures as backfill/sealing material
 - Compaction behaviour of claystone backfill, which controls the mechanical interactions with support linings (if existing) and the surrounding rock, and in turn determines the evolution of the backfill porosity and hydraulic conductivity
 - Permeability in relation with porosity, which dominates the fluid transport and thus the barrier function of the backfill/seal
 - Water retention and saturation, which determines the water saturation process, water storage capacity, water/gas two-phase flow, and buildup of swelling pressure in clay-based backfill/ seal
 - Swelling pressure in compacted claystone-bentonite mixtures as seal material, which is required for sealing of possibly remaining gaps within the seals and seal/rock interfaces and for supporting the surrounding rock against damage propagation
 - Thermal conductivity of buffer surrounding HLW containers, which controls the heat transfer and temperature distribution in the multi-barrier-system
- In situ investigation of hydro-mechanical responses of the Opalinus clay to the excavation of the gallery G08 within the mine-by (MB) experiment in the MT-URL

- Monitoring of long-term deformation of a borehole in the Opalinus clay at MT-URL (DM-A experiment)
- Numerical modelling and analysis of coupled hydro-mechanical processes in the Opalinus clay rock during the MB and DM-A experiments performed at MT-URL and coupled THM processes in the Callovo-Oxfordian argillite during the TED heating experiments conducted at MHM-URL.

Since September 2012, the THM-TON project has been merged into the EC DOPAS project – Full Scale Demonstration of Plugs and Seals /DOP 12/, to continue the investigations on the excavated claystone aggregate as backfill material and compacted claystone-bentonite mixtures as seal material.

In this report, main results obtained during the first project period (05.2007 – 05.2013) are presented. Whereas, in Volume I, laboratory experiments and results obtained on the clay rocks and claystone-based backfill/seal mixtures are presented and discussed, in this Volume II, the in situ experiments and the accompanying numerical modelling work are reported. In Chapter 2 and 3, on-going situ experiments are described and selected results are interpreted in terms of THM coupling effects. In Chapter 4 the related modelling work is introduced and discussed. Preliminary conclusions drawn from the research activities are summarized in Chapter 5.

2 Mont Terri Rock Laboratory

2.1 Site description

The Mont Terri Rock Laboratory (MTRL) is situated in the north-western part of Switzerland, where it has been excavated parallel to the security gallery of the Mont Terri motorway tunnel on the south-western slope of the Mont Terri anticline (Fig. 2.1 and Fig. 2.2). It is located in the Opalinus clay formation consisting of three main facies: the sandy facies, the shaly facies, and the sandy carbonate-rich facies. More details about the different lithologies can be found in /THU 99/. The bedding planes plunge towards the south-east with an azimuth of $140^{\circ} - 150^{\circ}$. The apparent thickness of the Opalinus clay is about 160 m. Its current overlay varies between 250 and 320 m, while it is estimated to have reached at least 1000 m in the past. The clay rock is saturated with water, but water circulations are practically negligible due to its very low permeability and pressure gradient. In the regions far from the openings in the MTRL the pore-water pressure amounts to values around 2 MPa and the rock temperature is about 15°C .



Fig. 2.1 Mont Terri motorway tunnel and location of the Mont Terri Rock Laboratory (left centre of the picture)

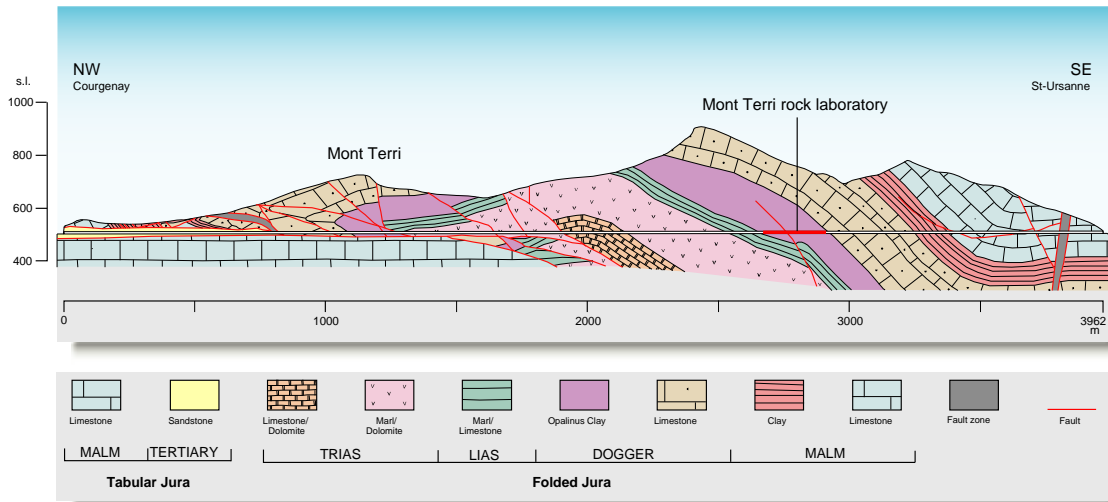


Fig. 2.2 Geological profile along the motorway tunnel showing the location of the Mont Terri Rock Laboratory

The state of stress at the MTRL is estimated according to /BOS 03/:

- the maximum principal stress σ_1 with a magnitude range of 6 – 7 MPa and a sub-vertical direction of 210° azimuth and 70° dip,
- the intermediate principal stress σ_2 with a magnitude range of 4 – 5 MPa and a sub-horizontal direction of 320° azimuth and 10° dip (sub-parallel to the motorway tunnel and the security gallery), and
- the minimum principal stress σ_3 with a magnitude range of 2 – 3 MPa and a sub-horizontal direction of 50° azimuth and 20° dip (more or less normal to the motorway tunnel and the security gallery).

The MB and DM-A test sites are located in the shaly facies, whereas the EZ-G test site is located in the sandy facies. A geometrical overview of the rock laboratory /MTP 10/ with the locations of the MB, EZ-G and DM-A experimental sites is shown in Fig. 2.3.

Fig. 2.4 shows the geological map of the Mont Terri Rock Laboratory with the location of main boreholes /MTP 10/ and the location of the aforementioned experimental sites.

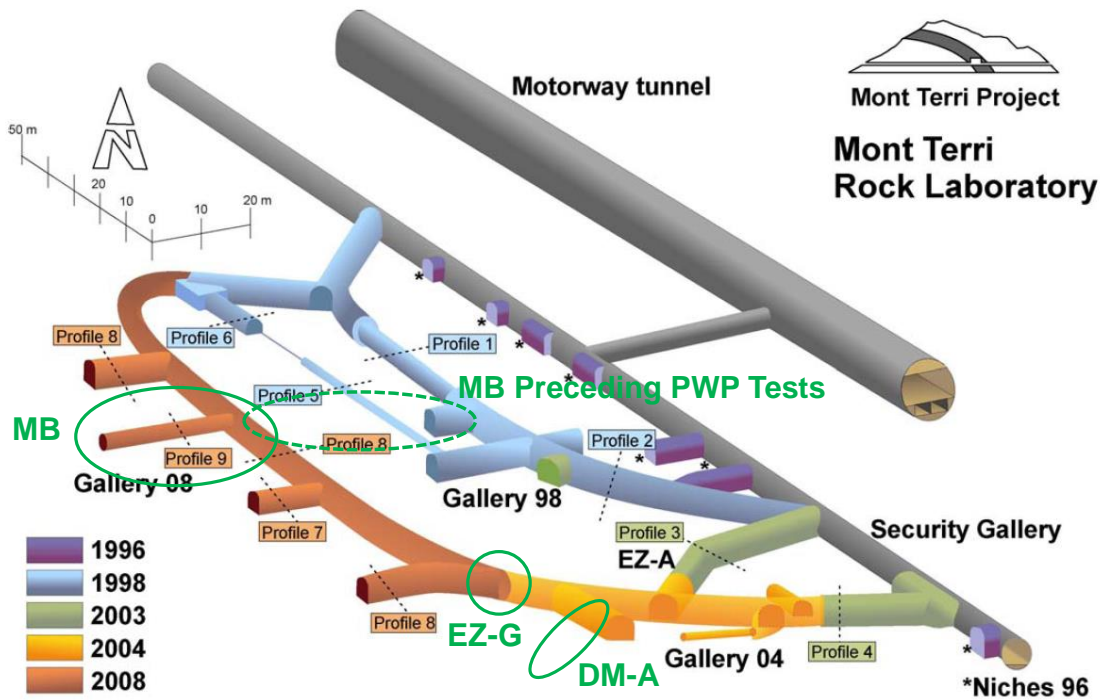


Fig. 2.3 Geometry of the Mont Terri Rock Laboratory, perspective view /MTP 10/, showing the location of the MB, EZ-G and DM-A experimental sites (MB preceding pore water pressure measurements were performed during Gallery 08 excavation)

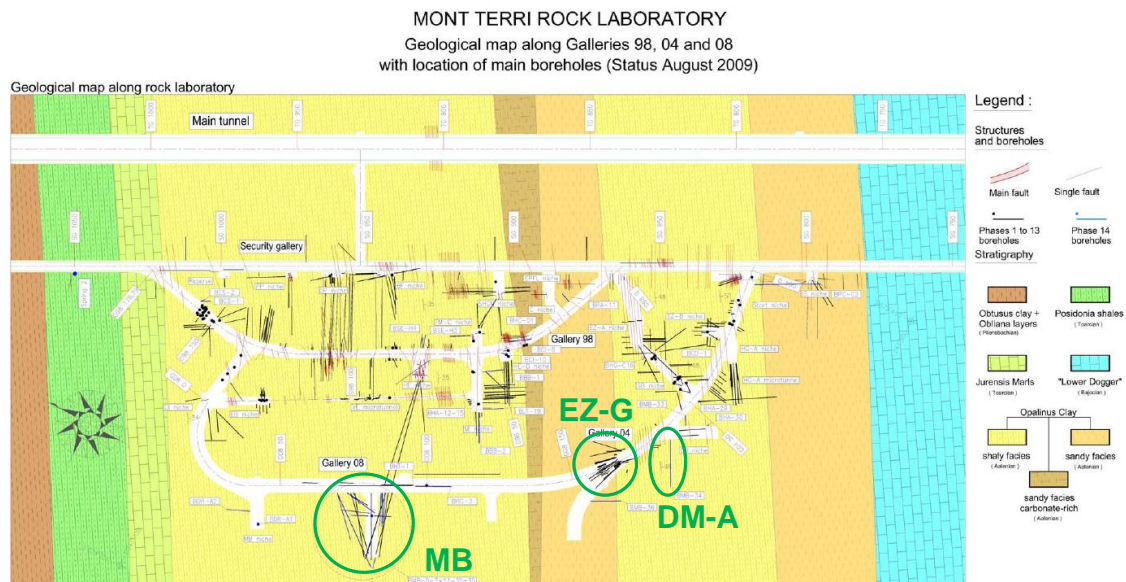


Fig. 2.4 Geological map of the Mont Terri Rock Laboratory with location of main boreholes /MTP 10/ showing the location of the MB, EZ-G and DM-A experimental sites

2.2 Pore water pressure measurements during Gallery 08 excavation

At the end of 2006 it became evident that the space for new experiments in the Mont Terri URL was limited. It was decided to expand the URL by advancing a 165-m-long gallery with 4 niches. The niches followed the strike of the bedding while the gallery was approximately perpendicular to the bedding strike.

The key variable in the hydraulic-mechanical coupled behaviour of the claystone is pore pressure. On the one hand, pore pressure is directly affected by any mechanical process in the rock. On the other hand, changes in pore pressure influence time-dependent rock deformation. In order to monitor pore water pressure (PWP) evolution during the gallery excavation, four long boreholes were drilled and instrumented with minipacker probes prior to mining of Gallery 08. The work was performed in the organisational frame of the Mine-by experiment (see Section 2.3), which was later performed in the MB niche (Fig. 2.3).

2.2.1 Test design

The four 42-mm boreholes BMB 1 – BMB 4 were drilled in October 2007 as preparatory work for the MB experiment. Two 37 m and 38 m long boreholes (BMB 1 and BMB 2) were drilled subhorizontally into the region of the planned Gallery 08 in order to measure pore pressure changes during the gallery excavation (Fig. 2.5). Two additional boreholes (BMB 3 and BMB 4) with a length of 24 m each were drilled 45° inclined downward into the region below the centre of the pillar below the existing Gallery 98 and the future Gallery 08 (Fig. 2.5). These two boreholes were used for reference measurements in the region positively undisturbed by the gallery excavation. In the frame of the BET project /MIH 10/ they were later used for additional measurements.

The boreholes were instrumented with sliding-end minipacker probes as shown in Fig. 2.6. Each minipacker was equipped with a Pt100 temperature sensor. The borehole voids above the minipackers were backfilled with synthetic resin. The injection and return tubes (steel capillaries) were connected to transducer racks and the test intervals of the boreholes filled with synthetic pore water (Pearson water). The pressure transducers and the temperature sensors were connected to a stand-alone GeoMonitor data acquisition system with connection to GRS via telephone line.

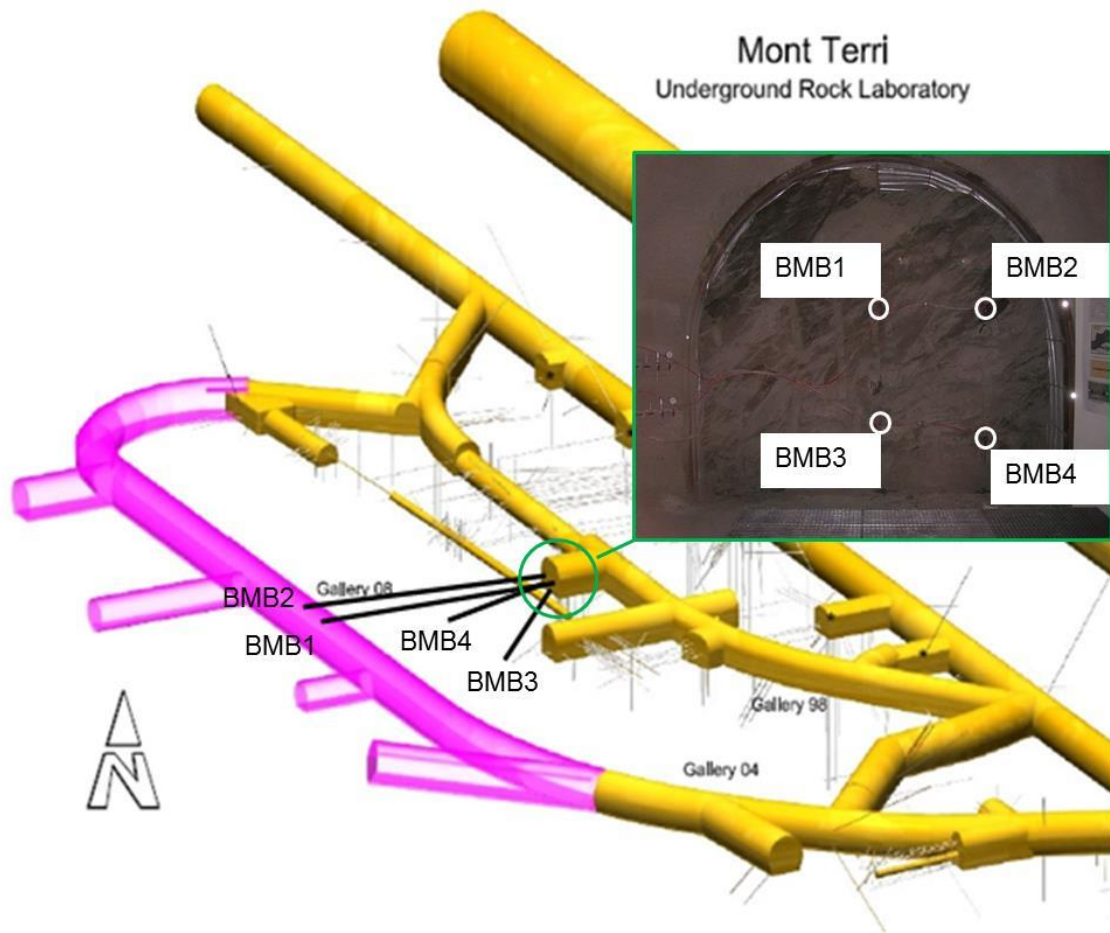


Fig. 2.5 Perspective view of the MTRL showing the locations of the four long PWP boreholes drilled from the HE-E niche (yellow: existing galleries, pink: planned Gallery 08 with niches)



Fig. 2.6 Sliding-end minipackers used for the PWP measurements in the long boreholes during Gallery 08 excavation

2.2.2 Test procedure

The boreholes were drilled in September/October 2007. On October 10, 2007 the pressure and temperature monitoring was started. After six weeks of pressure equilibration, water injection tests were performed in the test intervals of the boreholes to characterise the state of the rock adjacent to the probes in terms of permeability. Pearson water was injected by a manual pump causing an increased pressure of 0.5 MPa to 0.9 MPa in the respective interval, depending on the original pore pressure. The injected amount of water was measured using a precision balance. After injection, the valves were closed and the pressure decay by flow into the rock was recorded.

For evaluating the pressure decay curves in terms of permeability, the code WELTEST 200 was used. WELTEST 200 provides means to calculate the analytic solution to the diffusion equation or to numerically model pressure distribution in one- or two-dimensional models, and to iteratively minimize the deviation between the measured and calculated pressure data.

The parameters affecting the calculated pressure evolution are the rock permeability, the rock porosity, the wellbore storage coefficient, and the skin factor. The skin factor accounts for an increased or decreased permeability of a zone close to the borehole wall, which can be due to the drilling procedure. For the tests performed here, no skin factor was regarded.

The calculated pressure curves are rather insensitive to changes in porosity. The porosity was held constant at 10 %; changing the porosity in a wide range has no significant influence on the best fit permeability. Wellbore storage is important during the injection phase and controls the peak pressure reached during injection. The pressure curve form, especially during the shut-in phase, is controlled by the permeability. The best-fit permeability was determined by two-dimensional isotropic calculation, hydraulic anisotropy was not considered for the evaluation.

After liquid injection the pressure and temperature monitoring continued, and the response during excavation of Gallery 08 was assessed.

In September 2009, one year after completion of Gallery 08, water injection tests were repeated in the reference boreholes BMB 3 and BMB 4 in the frame of the BET project /MIH 10/.

2.2.3 Measurement results

The pressure and temperature data recorded until end of 2008 are shown in Fig. 2.7 and Fig. 2.8, respectively. Three time periods have been marked in yellow in the figures.

The first period is characterized by pressure equilibration and permeability testing. It can be seen that, from start-up of the measurements, the pressures at BMB 1, 2, and 3 are steadily increasing, while BMB 4 is showing a problematic behaviour. A realistic pressure is only reached after the injection testing and further equilibration towards the end of the yellow marked period. Usually, a slow pressure build-up can be attributed to gas remaining in the test interval. The pressure fluctuations during early equilibration, however, seem to indicate that some hydro-mechanic processes (damage?) are taking part. This seems to be supported by the fluctuations in temperature which are visible at BMB 4.

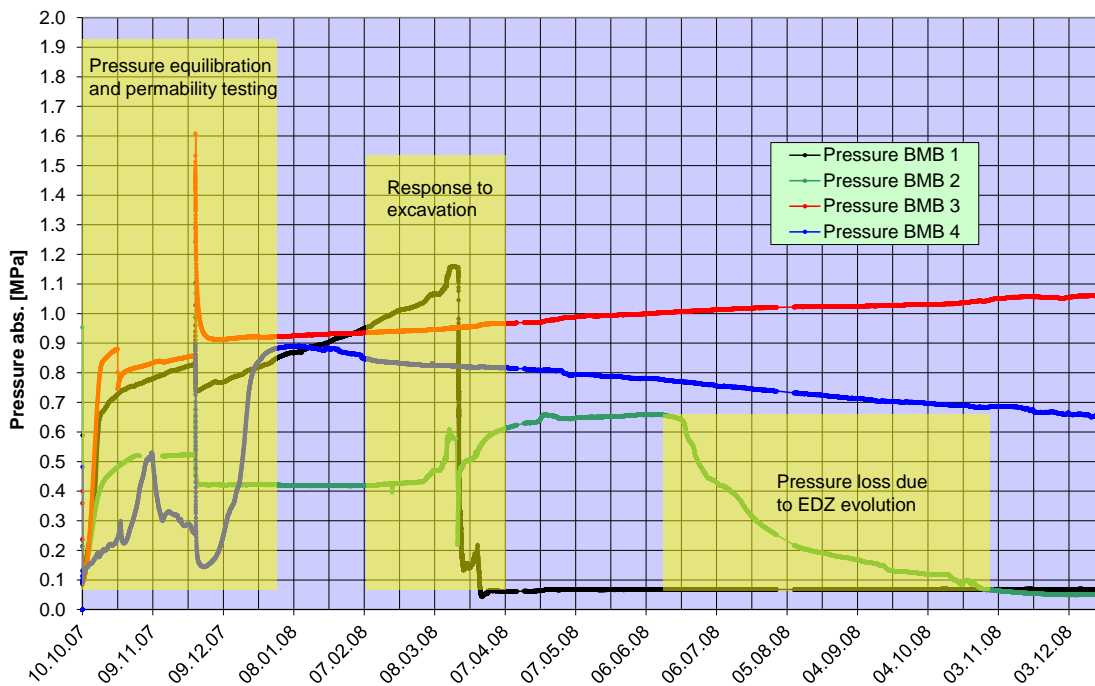


Fig. 2.7 Pressure recordings of BMB 1 – BMB 4

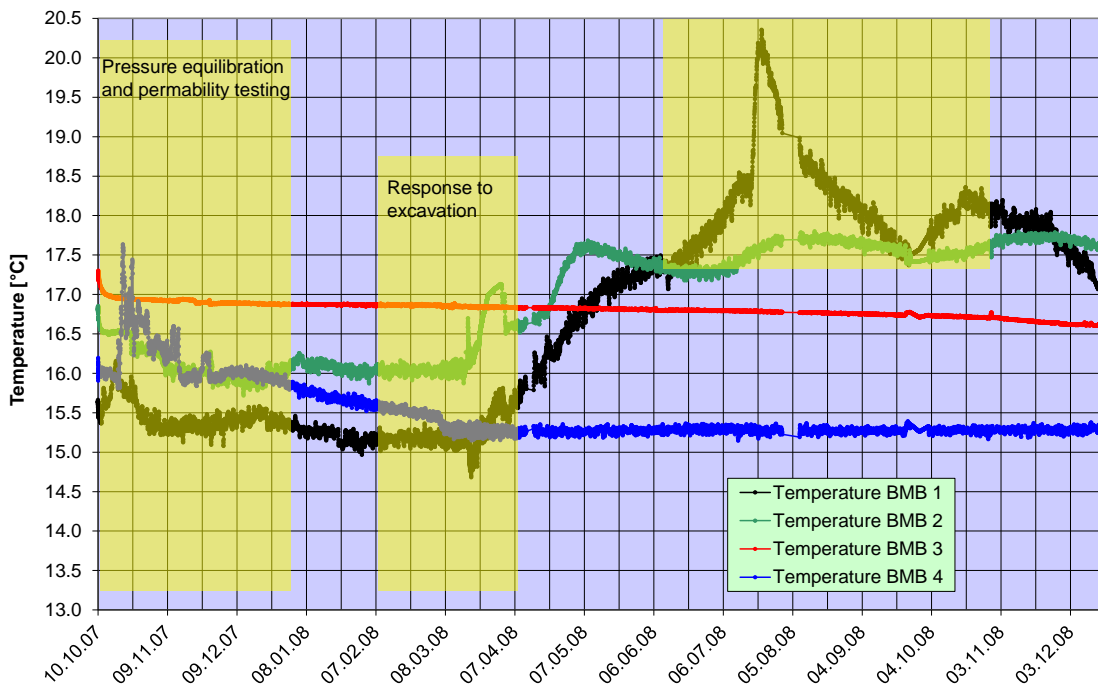


Fig. 2.8 Temperature recordings of BMB 1 – BMB 4

After the injection tests on November 27, 2007 the pressures at BMB 1 and BMB 4 first dropped, but then started rising again. This shows that the intervals were not in pressure equilibrium prior to the injection tests, introducing some uncertainty with respect to the permeability evaluation of the tests (see further down). The other two test intervals, however, show stable pressures after the injection tests, although the BMB 2 value of 0.4 MPa is surprisingly low compared to the others which range between 0.8 MPa and 1.0 MPa.

The second marked period in Fig. 2.7 and Fig. 2.8 is the response to excavation of Gallery 08. The pressure evolution at BMB 1 and BMB 2 is shown in more detail in Fig. 2.9, together with the actual excavation progress. The following statements can be made:

- When excavation progresses (phases of increasing tunnel length in the figure), pore pressure increases near the test intervals: see for instance first half of March.
- When excavation is stopped (constant tunnel length), pore pressure stabilizes: see March 8 – 10 or March 15 – 17.

- Pressure at BMB 2 (BMB 1) drops when tunnel metre 87 (89) is reached. This can be roughly attributed to the tunnel front passing the measurement cross section.

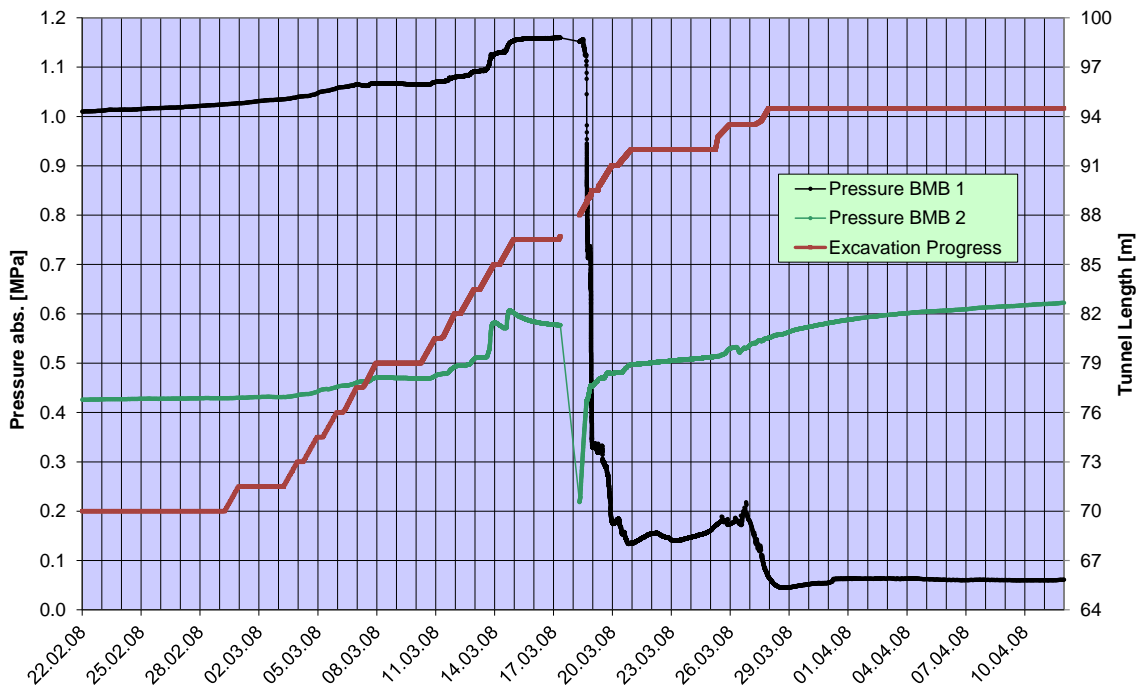


Fig. 2.9 Pressure evolution at BMB 1 and BMB 2 during Gallery 08 excavation, together with excavation progress

Due to the low diameter of the boreholes, they could not be surveyed. With their high length, there is some uncertainty regarding the actual position of the test interval. The boreholes had been designed so that they would actually be intersected by the tunnel excavation. None of the two boreholes were, however cut. It is assumed that both test intervals are located below the floor of Gallery 08. After the excavation front passed the test cross sections, the pressure recordings showed some recovery which is much more pronounced for BMB 2.

BMB 1 shows only slight recovery and, when excavation is resumed at the end of March, quickly drops below atmospheric pressure, which means the rock around BMB 1 is no longer saturated. It can be deduced that BMB 1 is located in the EDZ close to the surface of Gallery 08.

BMB 2, on the other hand, recovers to a pore pressure of 0.6 MPa, which is even higher than the value measured before excavation. Therefore, BMB 2 is most likely further

away from the gallery surface. In early July 2007, however, pressure at BMB 2 starts decreasing slowly and reaches suction in October (third period in Fig. 2.7). At the same time, temperature at BMB 1 increases significantly (Fig. 2.8). This is explained by the excavation work of the MB niche starting at that time, which resulted in mechanical disturbance and further evolution of the EDZ.

The permeability measurements by injection testing were, as mentioned before, influenced by the fact that pressure equilibration had not been reached in all intervals. The results lay between $3 \cdot 10^{-21} \text{ m}^2$ and $4 \cdot 10^{-18} \text{ m}^2$. The measurements performed in September 2009 yielded results of $4 \cdot 10^{-19} \text{ m}^2$ (BMB 3) and $8 \cdot 10^{-21} \text{ m}^2$ (BMB 4).

2.2.4 Conclusions drawn from the in-situ experiment

The pressure measurements show that stress concentrations beyond the excavation result in an increase of pore pressure, which drops quickly when the front passes the measurement cross section. Close to the excavation surface, EDZ formation leads to desaturation and suction.

Pore pressure prior to excavation and/or in the reference boreholes far from the excavation is not homogeneous and considerably lower than expected. Instead of about 2 MPa as postulated from theoretical considerations for the undisturbed saturated rock, values below 1.1 MPa were measured. This is possibly due to a far-reaching influence of the tunnel system of the rock laboratory.

A certain drawback for the evaluation of the response to excavation is the fact that the exact location of the test intervals is unknown. In the EZ-G experiment (Section 2.4), similar measurements were performed with a clear notion of sensor locations. The results shown here were confirmed.

2.3 Mine-by (MB) experiment

The Mine-by experiment was carried out to investigate the deformation and the coupled hydro-mechanical behaviour of the Opalinus Clay around an excavation parallel to the bedding, which is the orientation representative for a disposal gallery in the Suisse concept. The experiment was organized and managed by Nagra, ANDRA, GRS, BGR, and Obayashi /VIE 10/. The excavation of the MB niche was carried during October

and November 2008. In September 2009 the University of Alberta was contracted to provide a summary of the interpretation results /MAR 10/.

In this section 2.3 selected measurement results and the interpretation of the sensor response provided by /MAR 10/ and /VIE 10/ will be described shortly.

2.3.1 Test design

The MB niche is located near the centre of Gallery 08, Fig. 2.4. It consists of a 24.1 m-long and 4.5 m diameter circular opening. Excavation was carried out using a 14 ton hydraulic excavator (Cat 312) with the bucket removed and replaced with a road header, and all spoil was removed using a rubber tire skid steer. The advance was subparallel to the average strike of the bedding planes. Excavation of the face was planned to occur in 1.3 m increments followed by placement of the annular support during the pauses in the excavation of the face. The actual rate of excavation ranged from 0.6 to 1.9 m/day and averaged 1.3 m per day of construction. Support consisted of a total of six anchors installed approximately 0.8 m behind the face of the MB; 100 mm spaced wire mesh reinforcement affixed to the entire circumference of the MB; and two layers of shotcrete, the first was placed immediately following installation of the wire mesh and consisted of a 50 mm thick layer followed by an additional 100 mm final cover that was placed following completion of the MB. The anchors were installed prior to the placement of the wire mesh and the initial layer of shotcrete and prior to the application of the final layer of shotcrete. Following completion of the excavation activities, the roof of Gallery 08 was repaired and a 300 mm layer of concrete was placed on the floor along the entire length of the niche. The repairs included the removal of approximately 5 m² of the 50 mm thick layer of shotcrete near the connection of the niche with Gallery 08 and the placement of additional wire mesh reinforcement around the crown and upper sidewalls of the niche. Fig. 2.10 gives the actual start-stop dates for the excavation and support installation. A schematic sketch showing the MB support system is presented in Fig. 2.11.

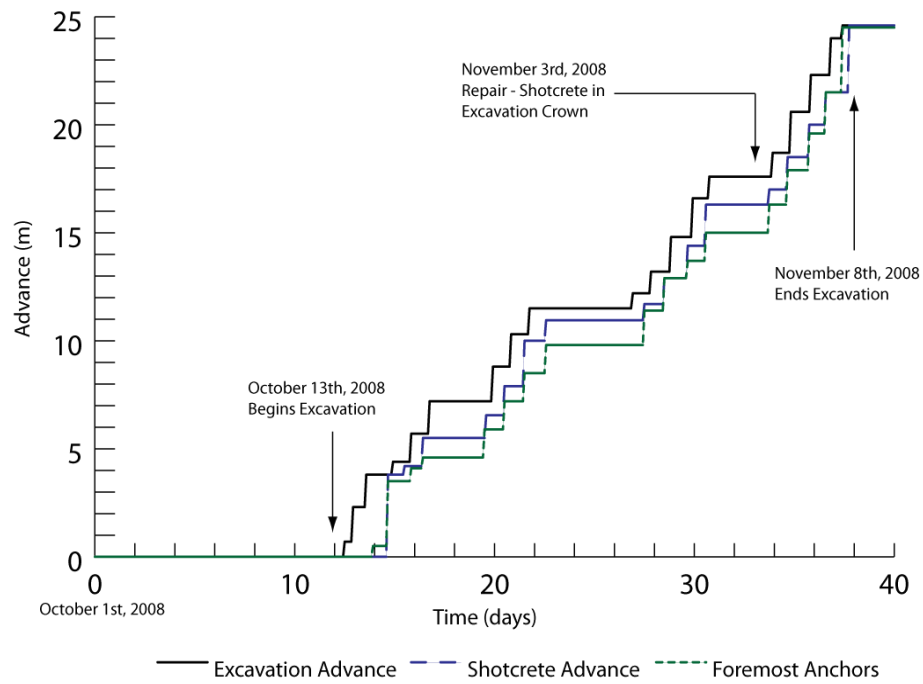


Fig. 2.10 Excavation sequence and support installation

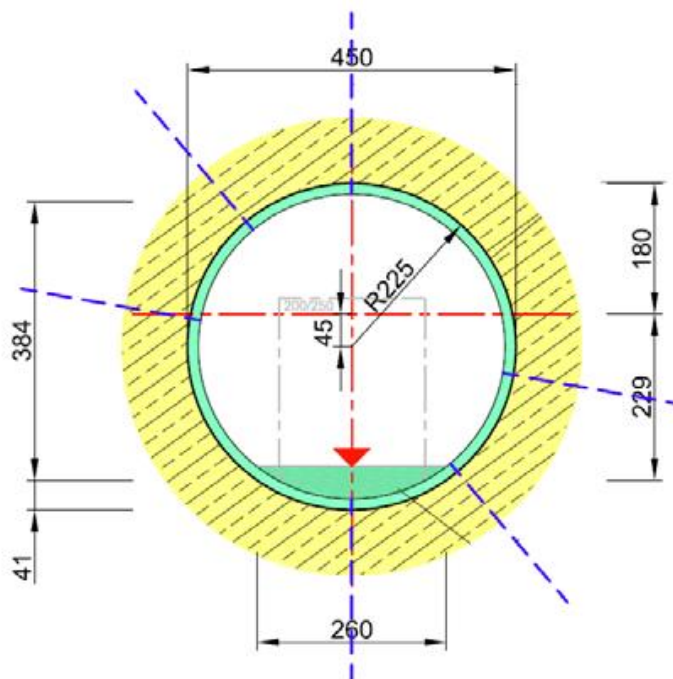


Fig. 2.11 Typical configuration of the MB support system

Prior to the excavation of the MB Niche, a number of instruments were installed at various locations around the proposed alignment from Gallery 08. In addition, a number of instruments were installed within the MB Niche throughout the course of the tunnel advance. The instruments were installed to measure the displacement fields and in-situ

pore pressures of the bedrock surrounding the niche as excavation advanced and after excavation was completed. The instrumentation used to monitor the excavation response consisted of piezometers (BMB-7/15/16/21-23), magnetic extensometers (BMB-17/18) sub-parallel to the tunnel axis, radial extensometers (BMB-28-31) installed at tunnel chainage, 15.3 m, a mineable face extensometer (BMB-13) installed parallel to the tunnel axis, and inclinometer chains (BMB-19/20) oriented sub-parallel to the tunnel axis, Fig. 2.12.

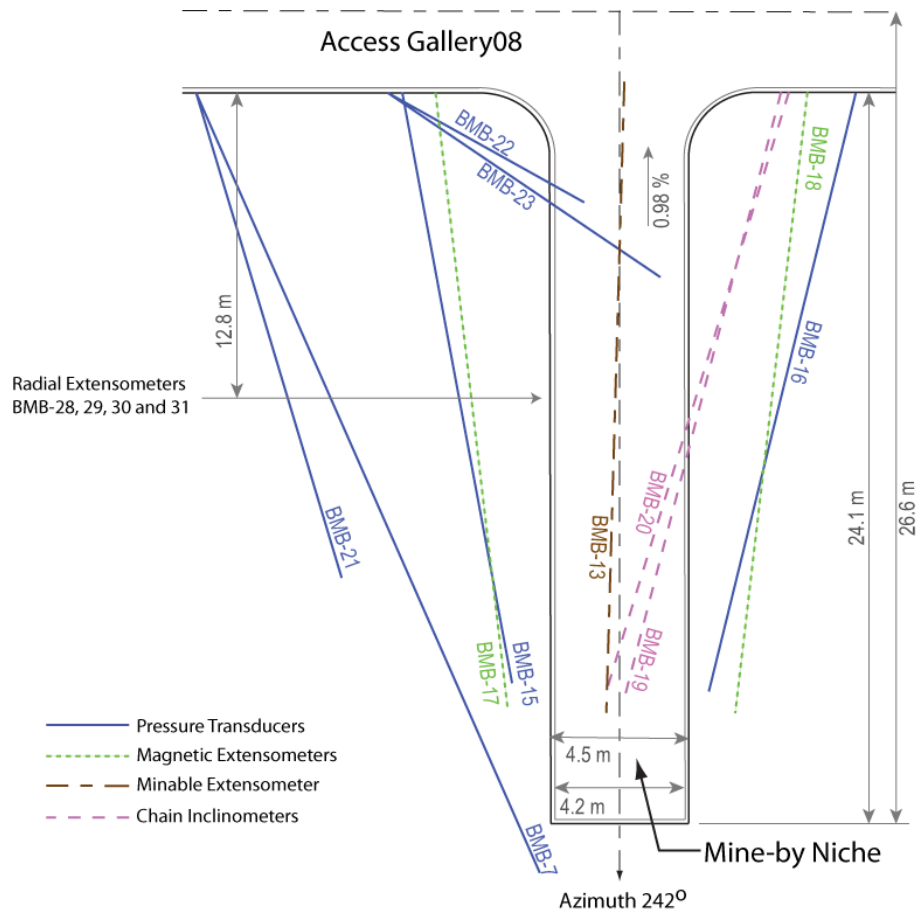


Fig. 2.12 Plan view of Mine-by Niche showing the layout of the instrumentation

2.3.2 Test procedure

The geological mapping during the excavation of Mine-by Niche was carried out as excavation progressed. The detailed mapping report by /MAD 10/ describes the characteristics of the bedding planes, the fractures that formed during the excavation process, as well as observations around the advancing excavation front and its relation to niche face stability and wet spot occurrences. The tunnel mapping clearly identified various

forms of face instability during niche excavation. In addition to this face instability a fracture set was observed that consisted of sub-vertical rough fractures of variable strike, but predominately-oriented perpendicular to the excavation direction. No significant shear movement seems to have occurred along this type of fractures and their repetitive pattern around the niche front indicates that they formed during the excavation works. Similar fractures were observed in the wall of Gallery 08, Fig. 2.13.



Fig. 2.13 Example of the excavation-induced fractures, /MAD 10/ (observed during the excavation of Gallery08 as well as in the face of niche excavation; but perpendicular to the tunnel axis)

2.3.3 Measurement results

As indicated in chapter 2.3.1 only summaries of the measured response are provided here.

Pore pressure response

Two strings of piezometers BMB-15/16 were used to monitor the excavation-induced pore pressure response. According to /VIE 10/ the piezometers show a characteristic response of an increase in pore pressure as the excavation advances and at some distance from the tunnel face the piezometers suddenly drains and losses all its pore pressure. All the piezometers go to essentially zero pore pressure. The actual pore

pressure may be negative as these piezometers cannot read negative pore pressures, Fig. 2.14.

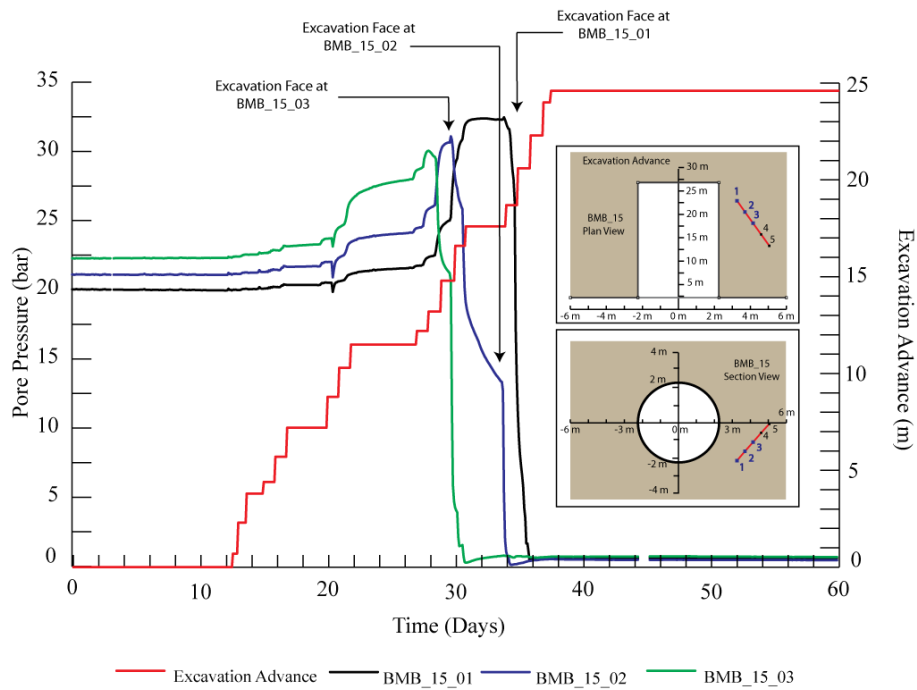


Fig. 2.14 Pore pressure response and excavation advance over time /VIE 10/

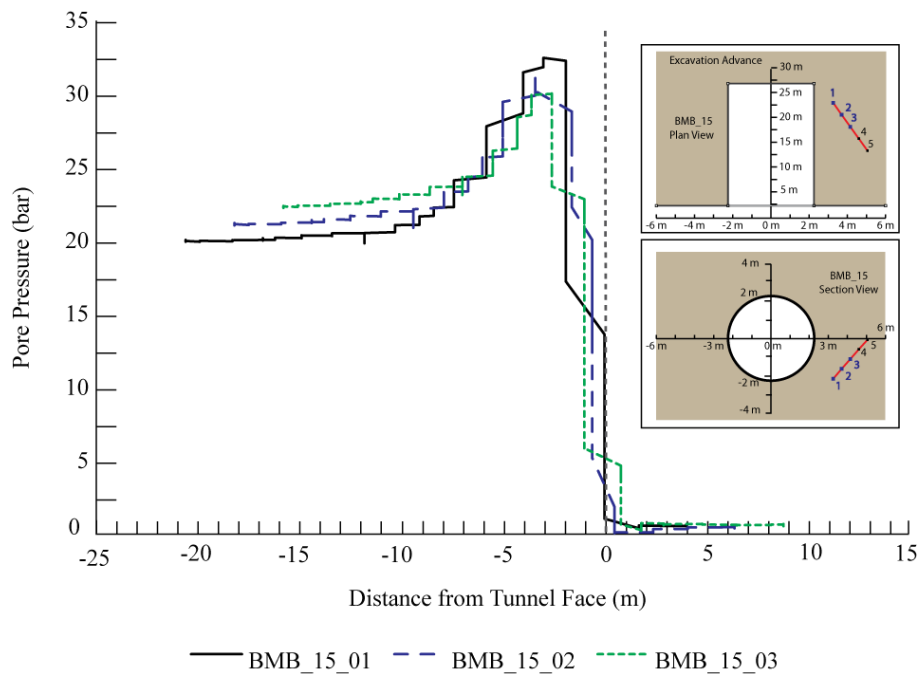


Fig. 2.15 Pore pressure response related to excavation advance /VIE 10/

The response is different for each piezometer depending on its location relative to the tunnel, Fig. 2.15. In general the piezometers closest to the tunnel start to show an increase in pore pressure due to the excavation advance when the tunnel is approximately 10 m from the tunnel face. When the tunnel face is approximately 2 to 3 m from the tunnel face the pressure rapidly decreases to essentially zero /VIE 10/.

Radial extensometer

The radial deformations were measured by 4 radial extensometers located at approximate chainage 12.8 m. These extensometers were installed to borehole depths up to 8 m. Extensometer BMB-28 was installed approximately parallel to bedding while BMB-30 was installed normal to bedding. The remaining extensometers BMB-29 and BMB-31 were installed crossing the bedding at approximately 35 to 45 degrees. Fig. 2.16 shows the response measured in the selected extensometer normal to bedding, Fig. 2.17 the response parallel to bedding, respectively.

At BMB-28 the extensometer response shows only marginal displacement in the first 2 points that are located approx. 2 m inside the rock. This typical behaviour indicates a certain detachment between 2 and 4 m from contour, whereas the 4 points at BMB-30 show the more or less characteristic response of rapidly increasing displacements with excavation advance, with its maximum value depending on the distance to the contour/ extensometer head.

Regarding the total deformation there does not appear to be any difference in the results parallel to bedding or perpendicular bedding, i. e., the total displacements measured at the deepest sensors (no.1) are up to 11 mm, regardless of orientation.

With regard to the complete displacements in the rock, elastic analyses suggest that at 4 diameters the measured displacements would be less than 10 % of the total radial displacements. To capture 90 % of the response the extensometers would have had to extend to a radial depth of approximately 18 m. Hence the radial extensometers were never intended to capture the complete response. This has to be kept in mind for interpreting the radial extensometer measurement results because the deepest anchor is normally used as the reference anchor and it usually assumed that this anchor is not moving MAR 10/ and /VIE 10/.

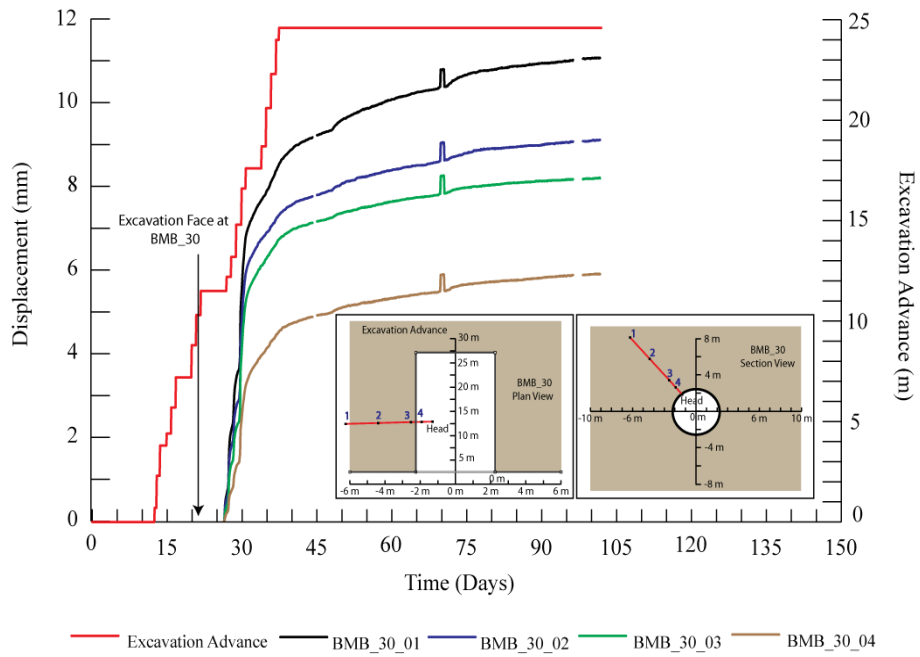


Fig. 2.16 Radial extensometer response normal to bedding at BMB-30 related to excavation advance /VIE 10/

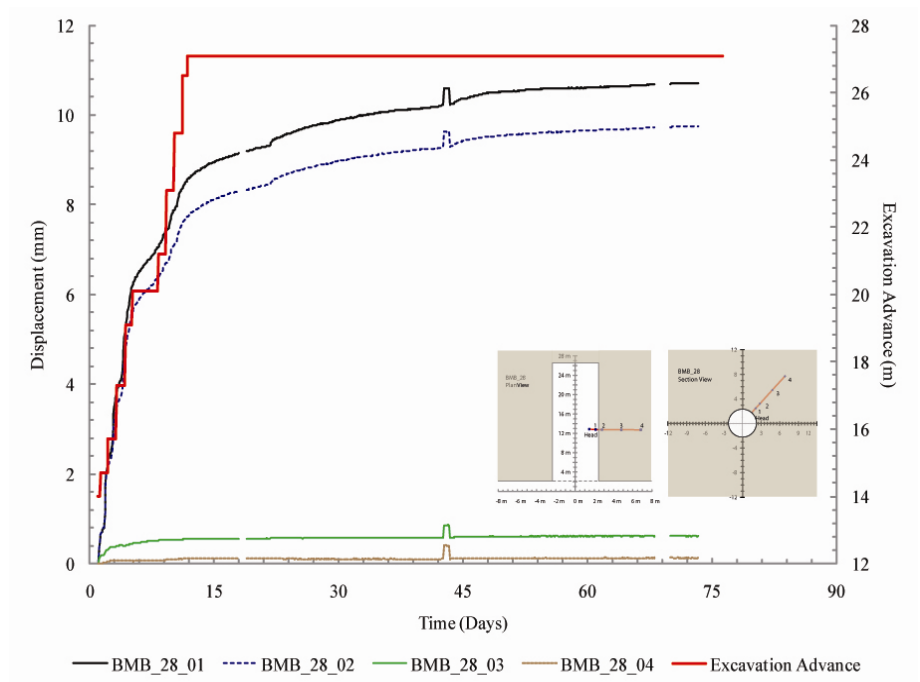


Fig. 2.17 Radial extensometer response sub-parallel to bedding at BMB-28 related to excavation advance /VIE 10/

Reverse head extensometer

A mineable extensometer was installed in the general direction of the centerline of the tunnel in BMB-13. This extensometer recorded the displacement that occurred ahead of the tunnel face in the general direction of the strike of the bedding. With each excavation step a portion of the extensometer is mined out. Fig. 2.18 shows the Reverse head extensometer response related to excavation advance. Deformation starts as axial shortening at a distance of about 15 m before mine-by and tends to reverse to extension at 10 m before mine-by. When first point of segment is excavated this segment becomes inactive.

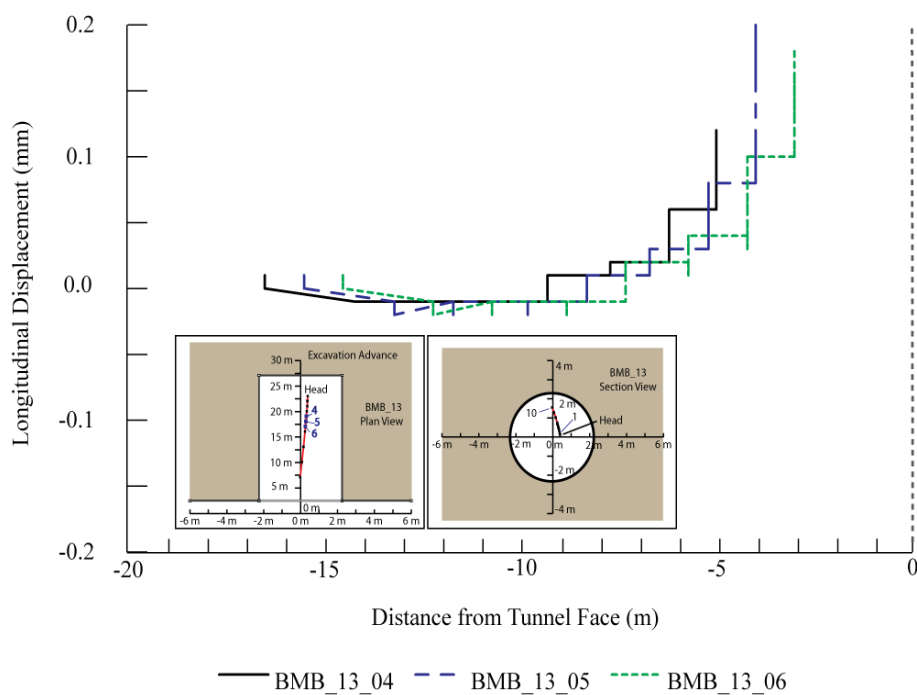


Fig. 2.18 Reverse head extensometer response related to excavation advance
/VIE 10/

Magnetic head extensometer

Two magnetic extensometers, BMB-17 and BMB-18, were installed adjacent to the tunnel and prior to excavation. The extensometers generally follow the tunnel center-line alignment, with a slight inclination towards the tunnel invert. Each instrument consists of a chain of extensometers, providing the ability to plot the axial deformation profile of the instrument for each excavation step.

Figure 2.19 shows that the measured response at BMB-18 follows the general trend of the expected response ahead of the tunnel face during the early advances of the tunnel. Due to stress redistribution and rock compression the shortening of extensometer segments starts 12 m before mine-by. When the excavation advance is about 1 – 2 m before mine-by, there is a clear change in the ground behaviour and the extensometer segments reverse to extension.

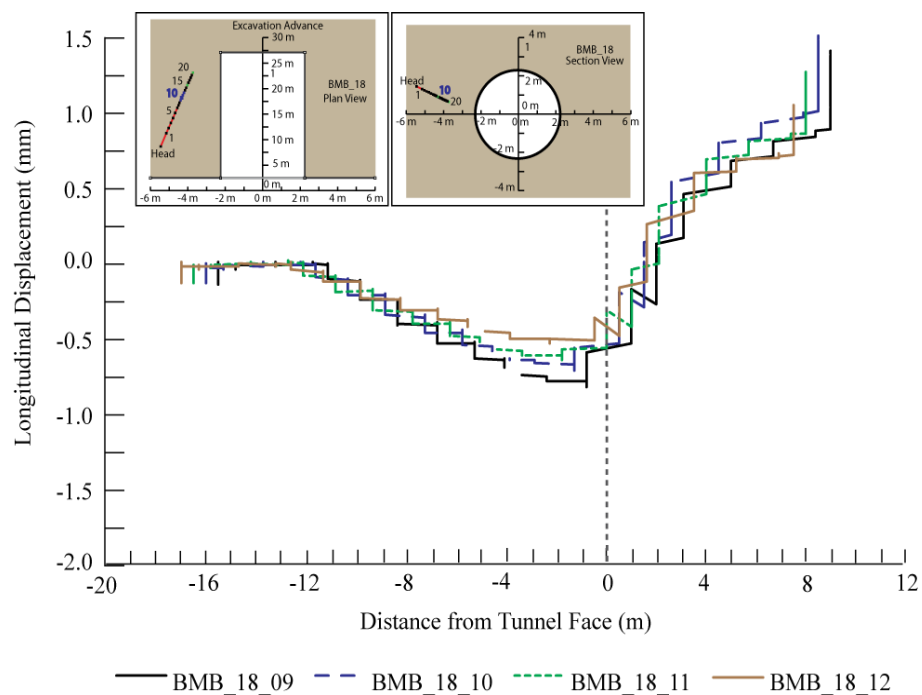


Fig. 2.19 Magnetic head extensometer response related to excavation advance /VIE 10/

Chain inclinometers (vertical deformation profiles)

Two chain inclinometers, BMB-19 and BMB-20, were installed prior to tunnel excavation. The extensometers layouts generally follow the general direction of the tunnel advance and cross the tunnel axis towards the end of the tunnel. Each instrument consists of a chain of inclinometers, measuring the angular deformation at each chain element. The array was installed so that angular deformations are measured in the vertical plane. These provide both cumulative and incremental vertical deformation profiles of the instrument at each excavation step.

Figure 2.20 shows the cumulative vertical displacement profiles for BMB-19 and BMB-20, respectively. The results are presented for several excavation steps where the farthest measuring point of the instrument is considered fixed (not influenced by excavation) and so absolute cumulative displacements can be estimated. In general, the response for the chain inclinometer is similar to the responses observed for the minable face extensometer and magnetic extensometer.

As the excavation face approaches the instrument, the instantaneous measured response still follows the expected elastic behaviour, but a time-dependent component of the measured deformations becomes significant and results in the increase of the total response.

Similar to the magnetic extensometer data, the magnitude of the chain inclinometer response with excavation advance is influenced by its distance to the tunnel face and its radial distance to the tunnel centerline, which is not the same for all measuring points as shown in Fig. 2.20. Interpreting the response measured by the chain inclinometer is challenging because the inclinometers cross the tunnel axis at an angle, and hence the deformation response is not symmetrical about the tunnel axis. What can be observed is the same characteristic behaviour observed in the radial extensometer response, i. e., the Time-dependent deformations become greater than the Instant deformations as more of the instrument is intersected by the tunnel profile.

BMB-19 is located above the tunnel roof and BMB-20 is located below the tunnel invert and both intersect the bedding at different angles. The deformations measured in BMB-20 are considerably smaller than those BMB-19. Regardless of the effects inside the tunnel, both inclinometers clearly show a similar response ahead of the tunnel face, Fig. 2.21.

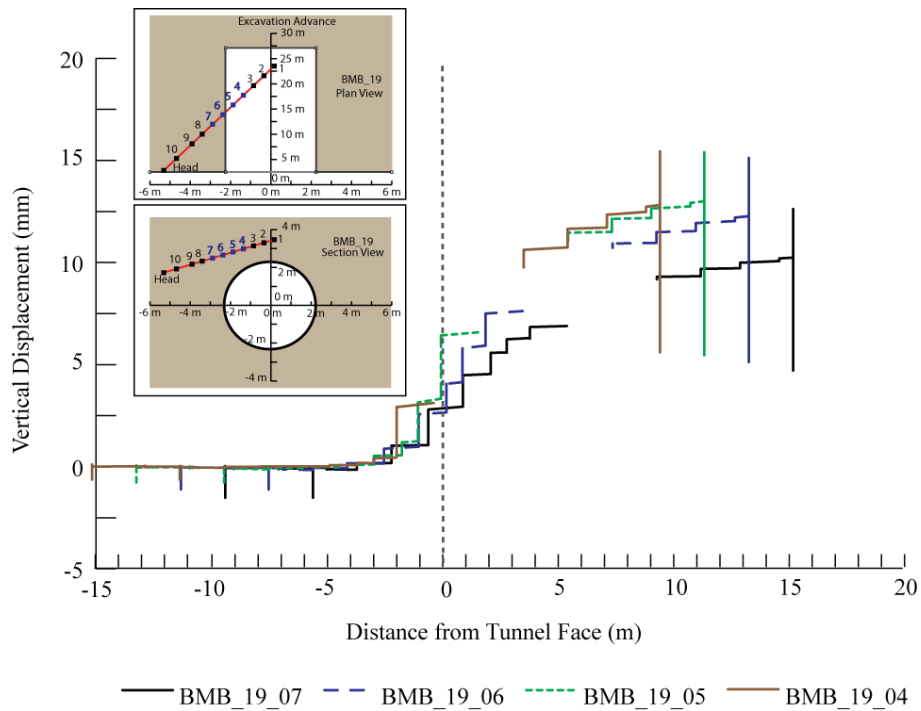


Fig. 2.20 Chain inclinometer response related to excavation advance (inclination changes converted into vertical displacements) /VIE 10/

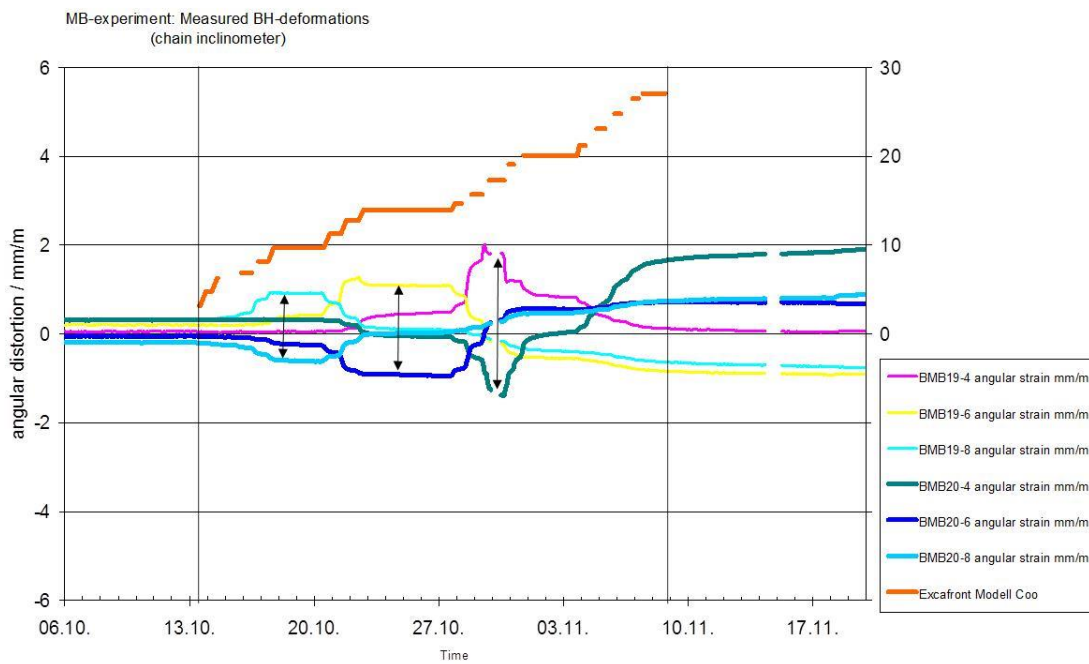


Fig. 2.21 Chain inclinometer response related to excavation advance - Symmetric evolution of angular strain in segments near entrance /VIE 10/

2.3.4 Conclusions drawn from the in situ-experiment

The instrumentation used to monitor the excavation-induced response associated with the excavation of the Mine-by Niche has shown that the measured response is made up of two components: (1) an elastic component and (2) a nonlinear time-dependent component. All the instrumentations used to measure the plane-strain response indicate that the time-dependent response is far greater than the elastic response. The radial extensometers were used to measure the plane strain response and the bottom to anchors measured the response between radial distances of 5 to 10 m. Even these extensometers suggest that yielding is occurring to depths greater than 5 m. The radial extensometers also suggest that the amount of yielding around the tunnel is relatively uniform. However, this is contradicted by the convergence measurements, which has highly variable displacements at different locations around the tunnel perimeter. When combining all the radial displacements for the conditions of plane strain there is no evidence to suggest that the displacement fields are different perpendicular or parallel to bedding. This conclusion may be influenced by the limitations of the radial extensometers, i. e., the radial distance and spacing of the anchors. The face extensometer showed that in the vicinity of the tunnel face the 3-dimensional effect limits the amount of nonelastic response to a distance of about 2 to 3 m ahead of the tunnel face /MAR 10/.

2.4 EZ-G experiment

The EZ-G experiment was designed for investigating the rock response to excavation with the geophysical methods. The idea was to instrument the tunnel front of the Gallery 04 (see Fig. 2.3) prior to the excavation of Gallery 08 and observe the pillar between the two galleries while it is excavated. GRS supported the experiment with pore pressure monitoring which is presented here.

2.4.1 Test design

An overview of the three test boreholes for pore pressure monitoring in the EZ-G is given in Fig. 2.22. The boreholes had a diameter of 20 mm and were drilled from the front (EZ-G6, EZ-G7) or the wall (EZ-G8) of Gallery 04. EZ-G6 and EZ-G7 were designed so that they would be cut by the excavation front after it passed them. EZ-G8 drilled from the Gallery 04 wall would remain intact even when the two galleries were joined. Figure 2.23 gives the exact information about borehole dimensions and orientations.

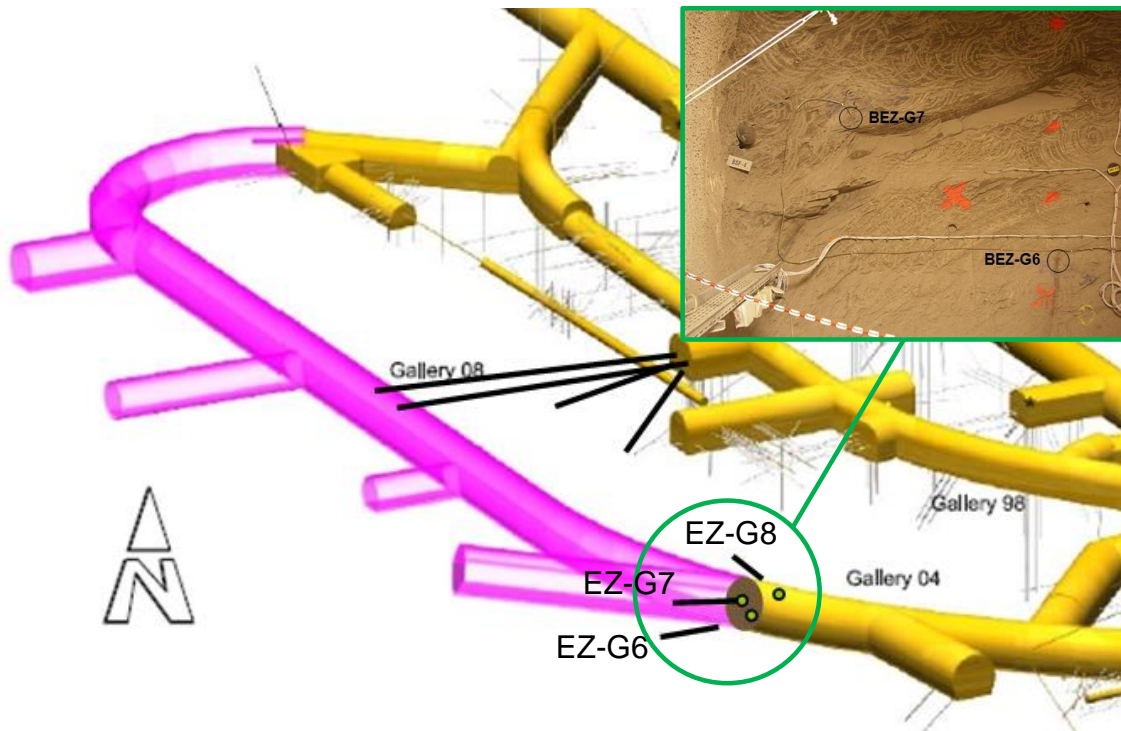


Fig. 2.22 EZ-G test site showing the pore pressure measurement boreholes (yellow: existing galleries, pink: planned Gallery 08 with niches)

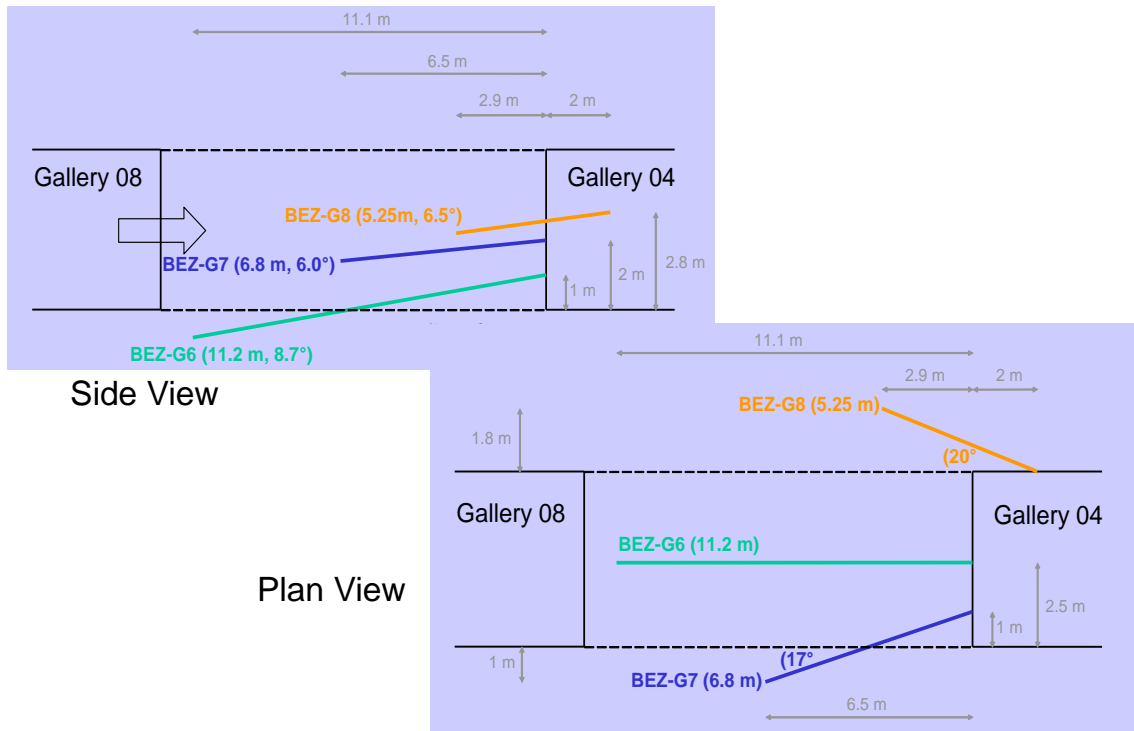


Fig. 2.23 Orientation of boreholes for pore pressure measurement

For the EZ-G pore pressure measurements GRS minipiezometers (Fig. 2.24) were used. Due to their dimensions very small boreholes are needed, which reduces disturbance and increases sensitivity of the measurements. The minipiezometers feature a pair of coaxial capillaries enabling removal of air from the system when water is injected.



Fig. 2.24 GRS minipiezometer for pore pressure measurement

In each of the test boreholes a minipiezometer was placed at maximum depth. Pt100 temperature sensors were placed in each borehole above behind the piezometer. After mechanical straining the minipacker the remaining borehole void behind each piezome-

ter was backfilled with synthetic resin (Sikadur 52) in order to completely seal the piezometer in the rock.

The capillaries of the piezometers were connected to transducer racks equipped with pressure gauges and pressure transducers located on the gallery wall. After finishing the installation, the measuring intervals of the piezometer probes were filled with artificial pore water (Pearson water). The pressure transducers and the temperature sensors were connected to a GeoMonitor data acquisition system with connection to GRS via telephone line.

2.4.2 Test procedure

The boreholes were drilled and instrumented in November 2007. On November 21, 2007 the pressure and temperature monitoring was started. After one week of pressure equilibration, water injection tests were performed in the test intervals of the boreholes to characterise the state of the rock adjacent to the probes in terms of permeability. Pearson water was injected by a manual pump causing an increased pressure of about 0.5 MPa in the respective interval, depending on the original pore pressure. The injected amount of water was measured using a precision balance. After injection, the valves were closed and the pressure decay by flow into the rock was recorded.

For evaluating the pressure decay curves in terms of permeability, the code WELTEST 200 was used, as described in Section 2.2.2.

After liquid injection the pressure and temperature monitoring continued. In July/August 2008, the excavation front of Gallery 08 passed the piezometers, and the pore pressure response was assessed.

2.4.3 Measurement results

The pressure evolution in the test intervals during the first weeks after start-up of measurement is shown in Fig. 2.25. After one week of pressure equilibration, injection tests were performed in all intervals. While at EZ-G6 and EZ-G7 a rather stable pressure of 1.3 to 1.5 MPa had been reached at that time, the pressure at EZ-G8 had remained at a very low value. After the injection tests, EZ-G6 and EZ-G7 returned to the pressure before injection, while EZ-G8 now remained at a pressure around 0.45 MPa,

still increasing slowly. This is a clear sign of air remaining in the interval of EZ-G8 at installation, which was then expelled during the injection test.

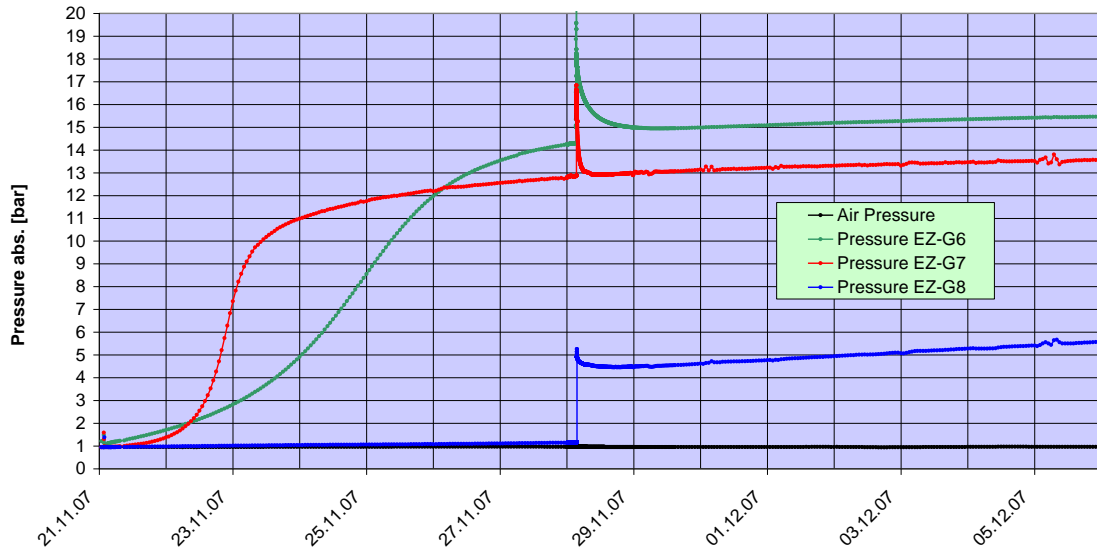


Fig. 2.25 Early pressure evolution in the test intervals: equilibration phase and water injection testing

The injection tests were evaluated in terms of permeability to water using WELTEST. As an example, Fig. 2.26 shows the shut-in phase pressure data for the test at EZ-G6 together with the WELTEST fit.

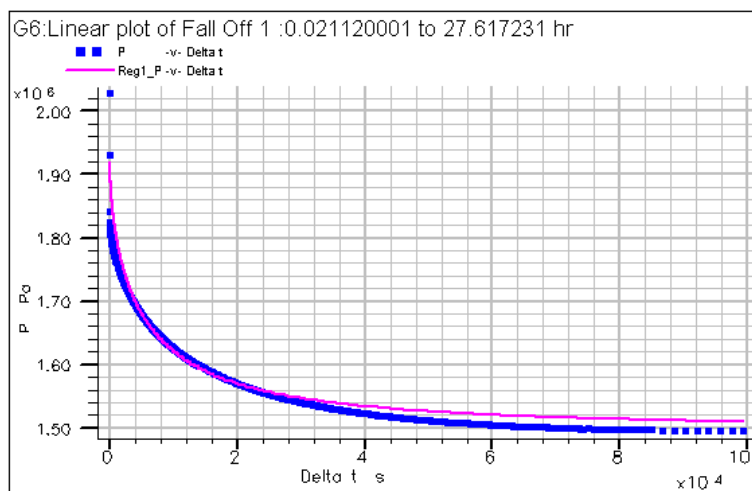


Fig. 2.26 Measured pressure data and WELTEST fit for the shut-in phase of the injection test at EZ-G6

The permeability values derived for EZ-G6 and EZ-G7 are $2 \cdot 10^{-18} \text{ m}^2$ and $1 \cdot 10^{-18} \text{ m}^2$, respectively. While this is somewhat higher than usual, it has to be mentioned that the EZ-G site is located in the sandy facies of the Opalinus clay and not in the shaly facies where most measurements have been taken up to now. The measurement at EZ-G8 was compromised by the air in the test interval. Consequently, an unrealistically high value of $1 \cdot 10^{-16} \text{ m}^2$ was obtained.

Figure 2.27 shows the pressure evolution in the three test intervals over the whole monitoring time. A few weeks after the injection tests all pressures had stabilized, although at different values: 1.5 – 1.6 MPa for EZ-G6, 1.4 MPa for EZ-G7, and 0.6 MPa for EZ-G8. The explanation for these differences is the distance of the measurement locations to the Gallery 04 (see Fig. 2.23). EZ-G8 is only 3 m away from the gallery which had been open for four years, disturbing the pore pressure distribution. The other test intervals are 6.8 m and 11.2 m from the Gallery 04 face and, consequently, less influenced.

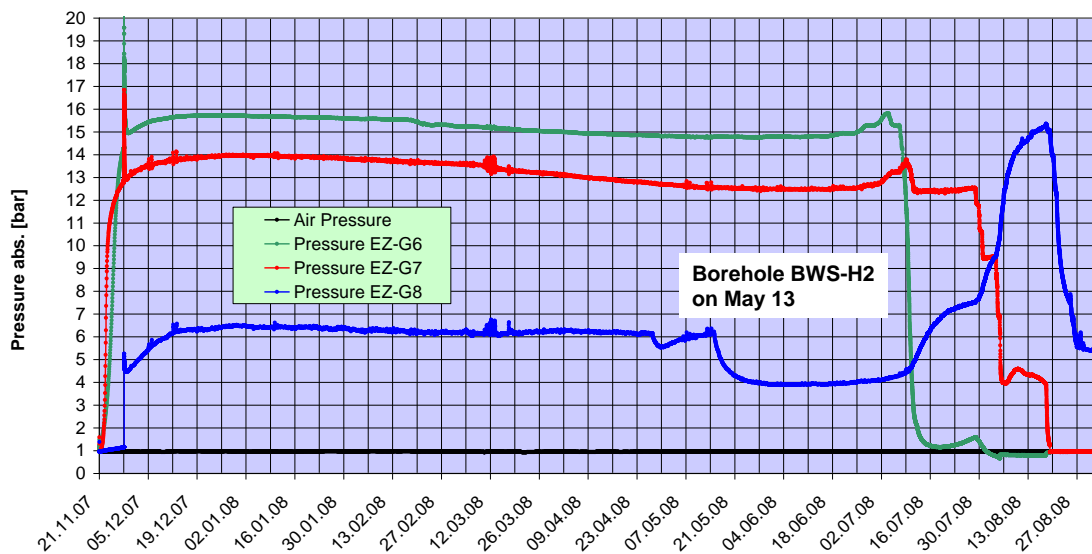


Fig. 2.27 Pressure evolution in the test intervals over the complete monitoring period

After nearly half a year of stable pressures the EZ-G8 pressure dropped to 0.4 MPa when, in the frame of the WS-H project, a borehole was drilled in the vicinity. Pressure stabilized again at the new level. From June 2008 on, the pressure response to excavation of Gallery 08 could be observed. This is shown in detail in Fig. 2.28.

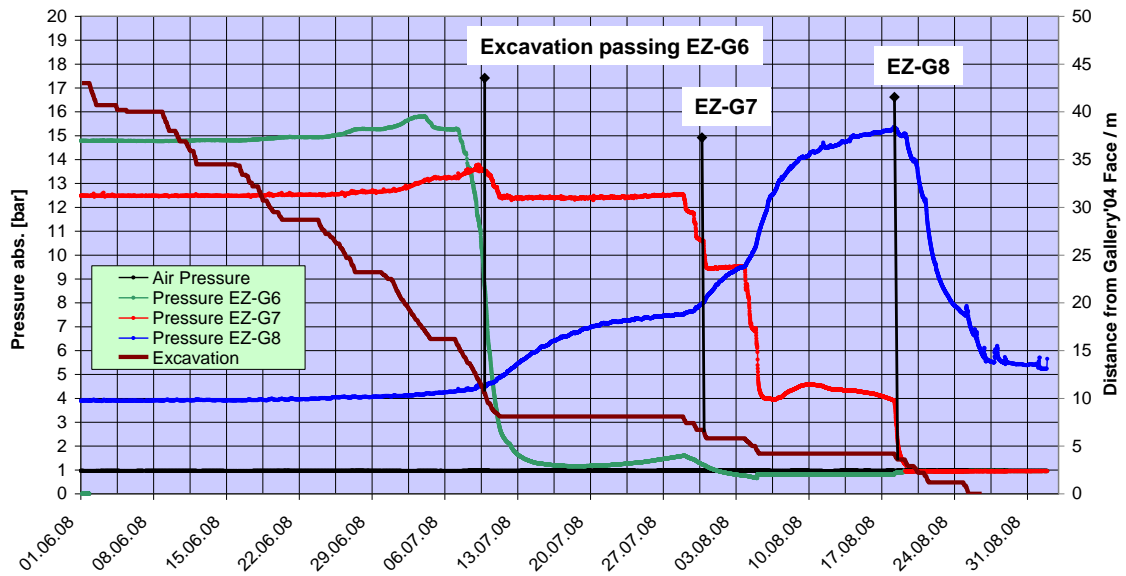


Fig. 2.28 Pressure evolution in the test intervals during excavation of the last 43 m of Gallery 08, together with excavation progress

The figure shows the pressure evolution in the test intervals during June, July, and August 2008, together with the Gallery 08 excavation progress which is shown as distance of the Gallery 08 face from the Gallery 04 face. On August 25, 2008, after two longer breaks at 8 m and 4 m pillar width between the galleries which were introduced to enable geophysical measurements, both galleries were joined.

All test intervals first showed an increase in pressure when the excavation front drew near, as was already observed in the long boreholes drilled from the HE-E niche (see Section 2.1). EZ-G6 pressure dropped already shortly before the excavation front passes the measurement location (marked in Fig. 2.28). Pressure then remained at a very low level (the test interval is only 1 m below the Gallery 08 floor), until the line was cut by the progressing excavation on August 5.

EZ-G7 pressure also dropped somewhat before the sensor was passed, but stabilized at a much higher level, which was then reduced with every excavation step. The difference to EZ-G6 can be explained by the fact that, although EZ-G7 is also only 1 m from the new gallery surface, it is located in the wall. With the pillar between the galleries becoming ever narrower, the surrounding rock had to take more and more load.

This is also the explanation for EZ-G8 which was reacting very strongly to the excavation. With the pillar becoming narrower, the pressure increased up to 1.5 MPa and decreased only when the sensor was passed. In contrast to the other sensors the pressure measurement continued after completion of the Gallery 08, because the pressure line was not cut by the excavation. Pressure stabilized to a value of about 0.5 MPa.

Temperature measurements during the excavation are shown in Fig. 2.29. Unfortunately, the temperature sensors were of poor quality, so that the EZ-G6 sensor failed early after instrumentation, and EZ-G7 showed a significant noise. It can, however, be observed that for both EZ-G7 and EZ-G8 temperature remained fairly constant until the sensors were passed by the excavation front. Then, temperature increased gradually by 2 °C, which is an effect of ventilation of the gallery.

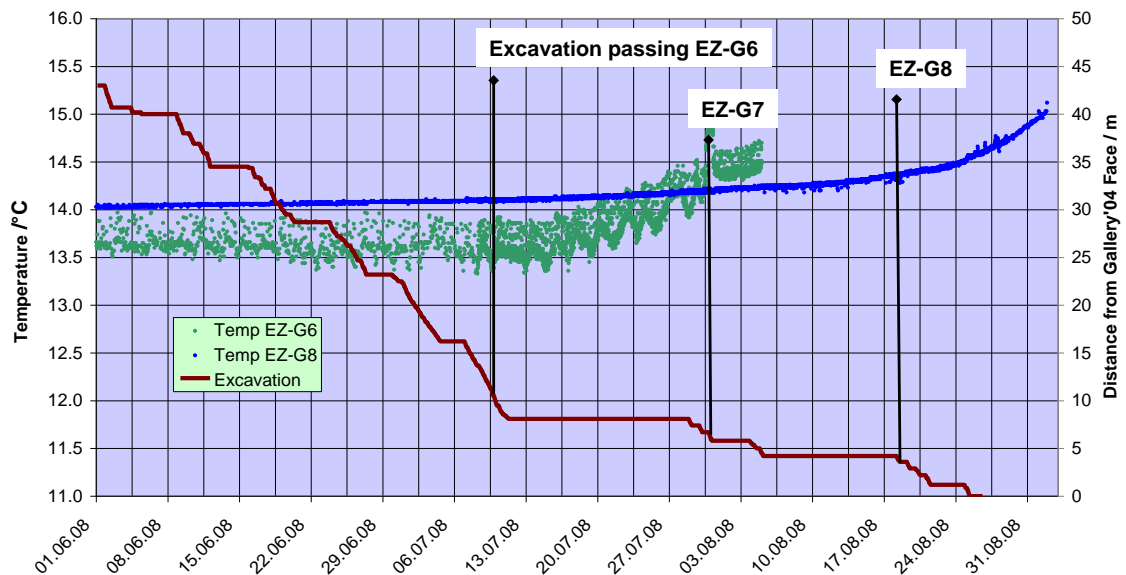


Fig. 2.29 Temperature evolution in the test intervals during excavation of the last 43 m of Gallery 08, together with excavation progress

2.4.4 Conclusions drawn from the in situ-experiment

The following conclusions can be drawn from the measurements in the frame of the EZ-G experiment.

- The pore pressure close to the Gallery 04 was reduced already before Gallery 08 excavation. Further away from Gallery 04, an initial pore pressure around 1.5 MPa seems probable.
- During excavation, a pressure concentration zone as elastic reaction evolves in front of the excavation face. Close to the excavation face, pore pressure is reduced as a consequence of unloading and potential damage.
- Temperature of the rock close to the excavation is increased by ventilation.
- Permeability of the sandy facies seems to be slightly higher than that of the shaly facies, at least at the EZ-G location.

2.5 DM-A experiment

2.5.1 Test design

In the frame of the Mine-By (MB) Experiment performed by Nagra, BGR, and GRS, the hydraulic-mechanical response of the clay rock to excavation has been investigated, see also Section 2.3. As a supplement to this experiment, GRS monitors the long-term deformation of the rock using a dilatometer probe installed in an 18 m deep horizontal borehole drilled parallel to the bedding from the DR Niche. Figure 2.30 shows a schematic sketch of the borehole dilatometer as well as some pictures taken during the installation process on-site.

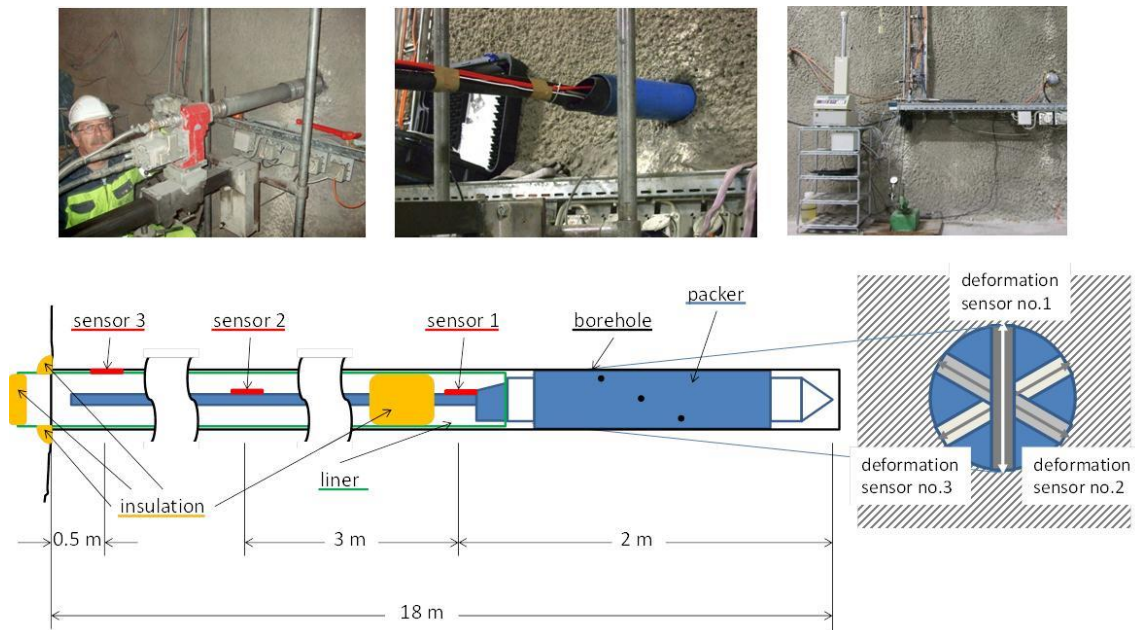


Fig. 2.30 Installation process of the borehole dilatometer on-site (above) and the schematic sketch of the probe (left: longitudinal view showing the packer and the temperature/humidity sensors, right: cross section showing the orientation of the deformation sensors, hatching = bedding plane position)

The borehole dilatometer consists of a 2 m long packer probe equipped with three deformation sensors measuring the borehole diameter change in three directions 60° apart. The borehole between the collar and the probe is lined with a plastic tube. Two combined temperature/humidity sensors are located inside the tube, sensor 1 directly behind the probe and sensor 2 at 3 m distance. A third temperature/humidity sensor is located between the tube and the borehole wall, about 0.5 m from the borehole collar

2.5.2 Test procedure

The probe was installed in June 2009, after considerable problems during drilling caused by borehole wall break-outs. The packer pressure was set to 0.5 MPa in order to hinder borehole convergence as little as possible while maintaining a secure coupling between deformation sensors and borehole wall. After probe installation it was found that the vertically oriented deformation sensor was stuck. A possible cause was the installation procedure itself: The probe had to be pushed along the borehole, which may have caused mechanical damage to the sensor. On July 15th and 16th, 2009 it was unsuccessfully tried to reactivate the sensor by a set of pressure pulses and reliefs on

the packer. Figure 2.31 shows the packer pressure tests of July 15th and 16th and the response of the two active deformation sensors in detail.

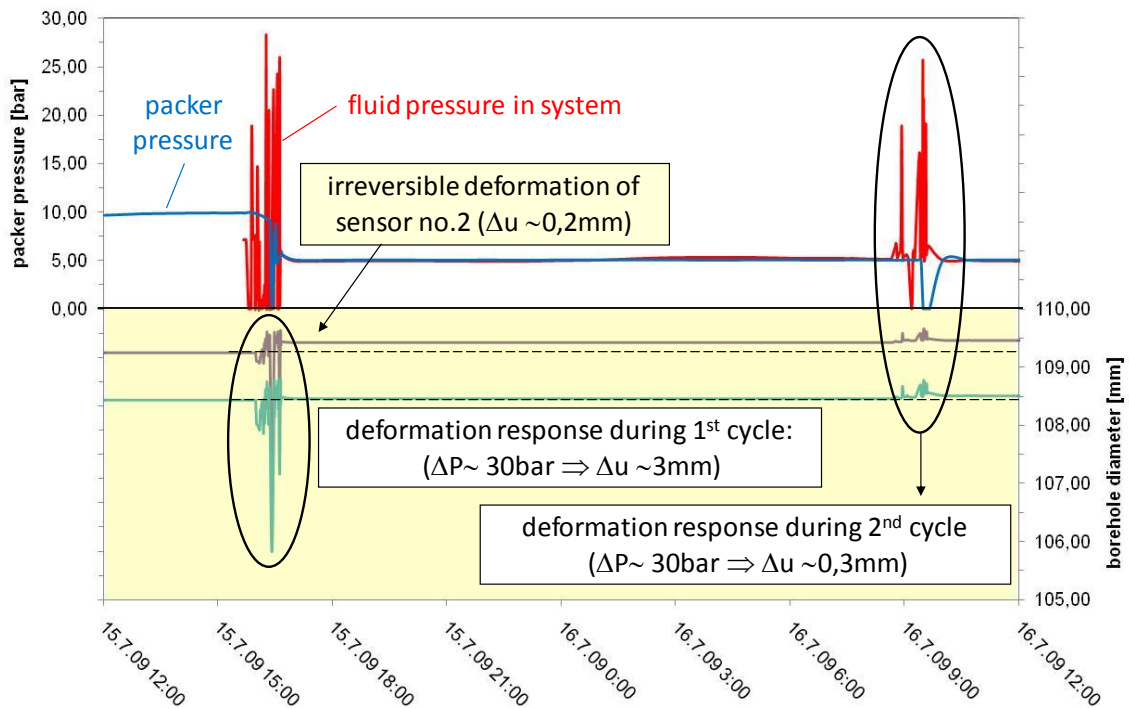


Fig. 2.31 Packer pressure tests on July 15th and 16th, 2009 and response of the borehole deformation sensors

A pressure change in the range of 3 MPa resulted in a borehole diameter change of about 3 mm on July 15th, with an irreversible deformation (diameter increase) of about 0.2 mm visible at sensor no. 2. A second test on July 16th with similar pressure changes resulted in a much smaller total deformation with no irreversible component. This difference is interpreted by a recompaction of the damaged borehole wall during the first pressure test. Afterwards the packer pressure was readjusted to 0.5 MPa and held constant by a pump.

2.5.3 Measurement results

Since the pressure tests did not result in reactivation of the vertical deformation sensor, the packer pressure was kept constant at 0.5 MPa afterwards, and borehole deformation was recorded using the remaining two sensors. An overview of the recorded data of packer pressure and the two remaining deformation sensors is given in Fig. 2.32.

An overview of the recorded data of pore water pressure is included in Fig. 2.32.

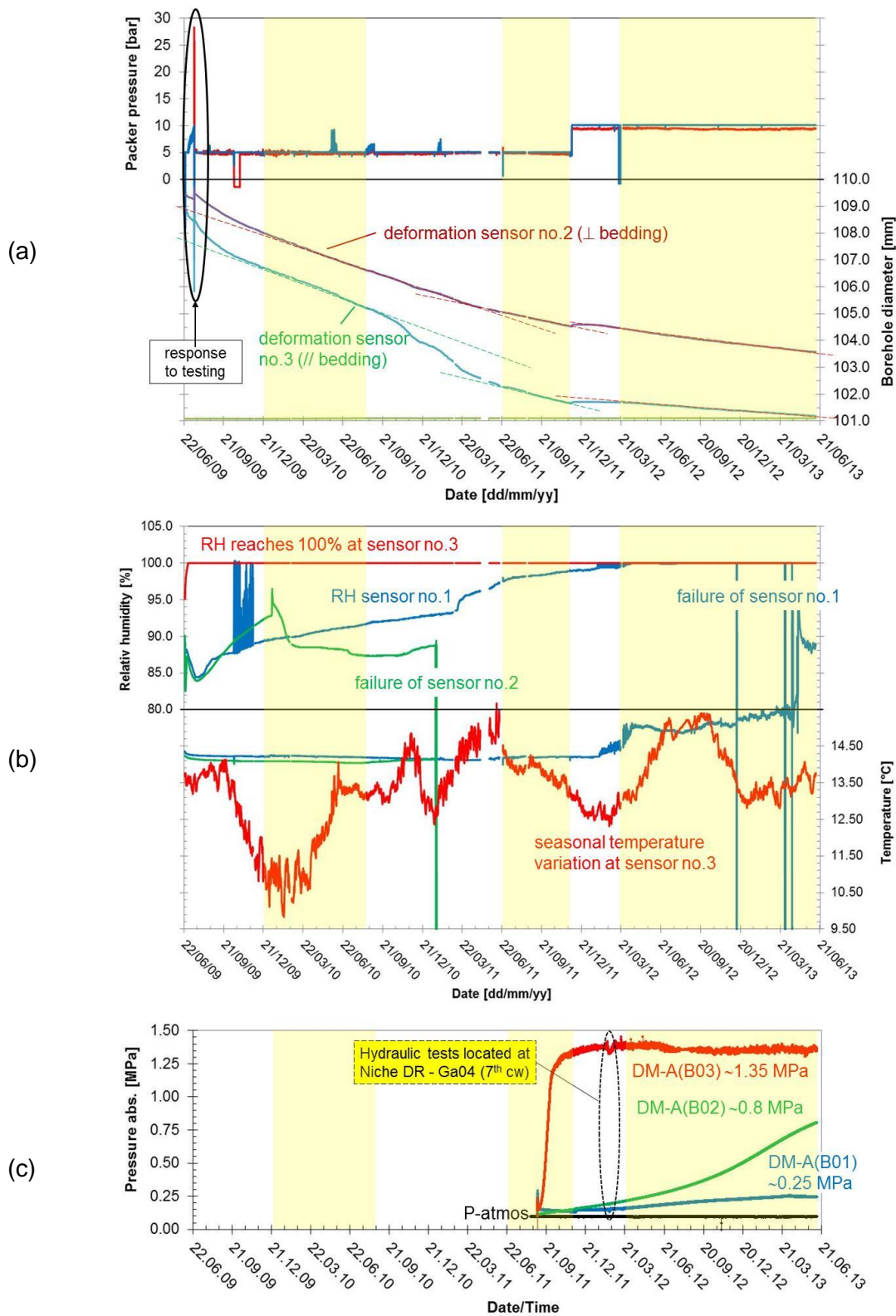


Fig. 2.32 Experimental results of the dilatometer probe: (a) packer pressure (above) and borehole deformation (below) as well as (b) relative humidity (above) and temperature (below); Experimental results of the minipiezometer in DM-A (B01-03) in (c) pore-water pressure

Note that deformation sensor no.2 is roughly perpendicular to the bedding (with a 15° deviation), while the angle between the bedding planes and sensor no.3 is rather small (again about 15°). The figure shows that after a transient period during the first months of measurement the borehole deformation rate has remained nearly constant since the end of 2009.

The results of the temperature / humidity sensors inside the borehole liner show a constant temperature and smooth relative humidity evolution, which implies that the deformation behaviour is not influenced by temperature or humidity changes. The sensor close to the borehole collar between the liner and the borehole wall shows an expected temperature variation similar to the drift temperature and a humidity of 100 % less than one week after installation, which can be attributed to a full re-saturation of the annulus between liner and borehole wall. Erroneous data of humidity sensor 1 in October and November 2009 are caused by electric problems, since beginning of December 2009 the data evolution has been smooth again.

In November 2011 the packer pressure was increased to prevent the deformation sensor no. 3 to reach minimum deformation. It was expected that the borehole would increase its volume as a consequence of the increase in packer pressure. Unexpectedly the response of the deformation sensors was very small. Both sensors show a small divergent deformation followed by a phase of three month of stress redistribution. From the End of March 2012 both deformation sensors show nearly constant deformation behaviour.

Accompanying physical modelling and numerical simulation work was performed, see Section 4.4. One of the general outcomes of this modelling work was that the in-situ experiment gives no information on the existence of pore water pressure gradients and their evolution with time. Therefore in September 2011 in total three small pore water pressure sensors were installed in the vicinity of borehole BMB-34, which contains the dilatometer probe. Figure 2.33 shows a sketch of the geometrical boundary conditions of the new boreholes DM-A (B01-03) and the orientation of the bedding planes.

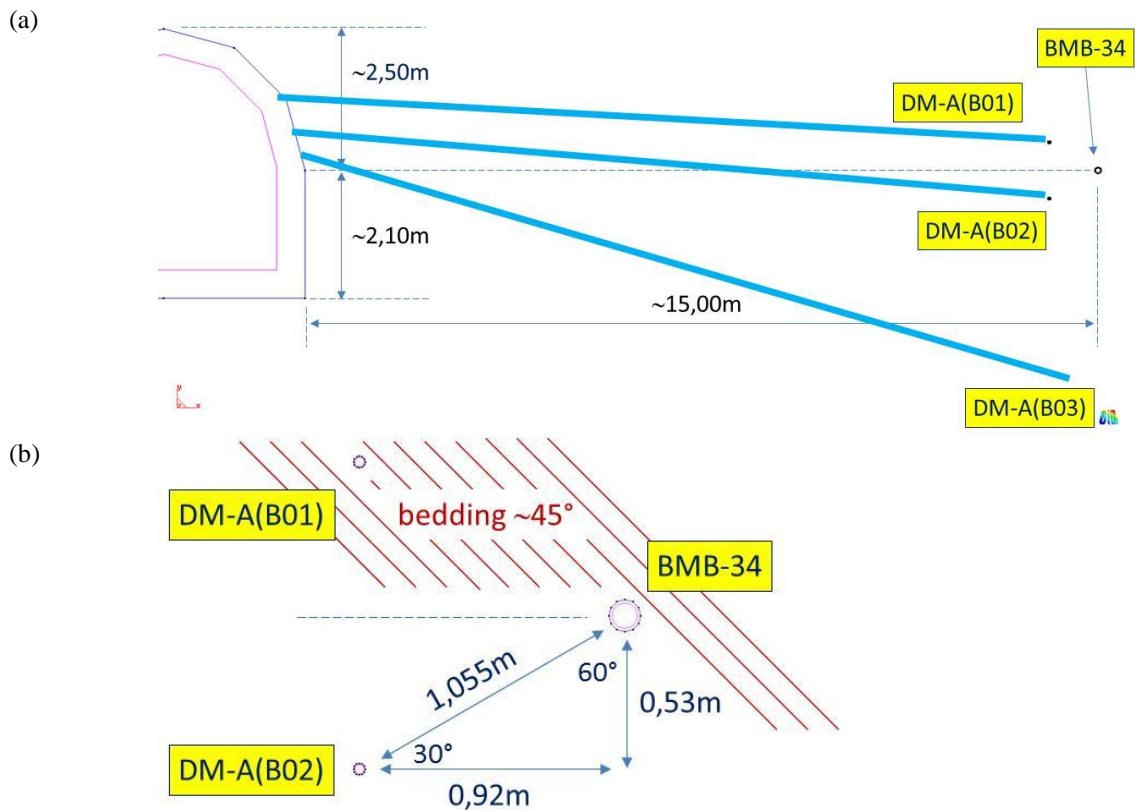


Fig. 2.33 Sketch of the geometrical boundary conditions of (a) the new boreholes DM-A (B01-03) and (b) the orientation of the bedding planes

2.5.4 Conclusions drawn from the in situ-experiment

Both deformation sensors parallel and perpendicular to bedding show constant deformation behaviour over several time periods from 3 month up to more than one year. From these periods it might be easy to identify stationary deformation rates to describe the viscous behaviour of the Opalinus clay.

Nevertheless the results from the pore water pressure sensors, especially the values that were measured perpendicular to bedding in DM-A(B02) show an on-going increase in pore pressure. Whereas the sensor DM-A(B01) parallel to the bedding planes and at short distance to the dilatometer probe in borehole BMB-34 might have reached equilibrium at low pressures of 0.25 MPa. The sensor DM-A(B03) is far away from the deformation sensor clearly shows pore water pressure equilibrium an constant pressure of 1.35 MPa. This value should be used as initial pore pressure value for numerical simulation.

Regarding both, the constant deformation rate and the increase in pore pressure, at this time it is hardly possible to identify the deformation effect that goes along with the drainage of the claystone porous structure (consolidation) and the long-term viscous “creep” behaviour of the rock material.

3 Meuse/Haute-Marne underground research laboratory

3.1 Site description

The underground research laboratory MHM-URL has been constructed in the Callovo-Oxfordian argillaceous formation on the eastern boundary of the Paris Basin, comprising a sequence of nearly horizontal limestone layers, marls and argillaceous rocks deposited at the bottom of former oceans (Fig. 3.1) /AND 05/. The formation represents over-consolidated sediments of the Jurassic Age (about 150 million years old). The homogeneous rock mass of about 130 m located at depths between 420 m to 550 m is investigated in the MHM-URL. The URL consists of two shafts, a large number of drifts and boreholes at depths between 445 m and 490 m. In accordance with the mineral composition and common mechanical characteristics, the COX formation is divided into three rheological zones or layers, the upper (A'), the median (B'), and the lower (C') zone. Fig. 3.2 illustrates the distribution of mineral components in these zones /AND99/, while the distribution of the geomechanical properties, such as water content (w), uniaxial compressive strength (R_c), and elastic modulus (E), is presented in Fig. 3.3 and in Table 3.1 /SU 07/.

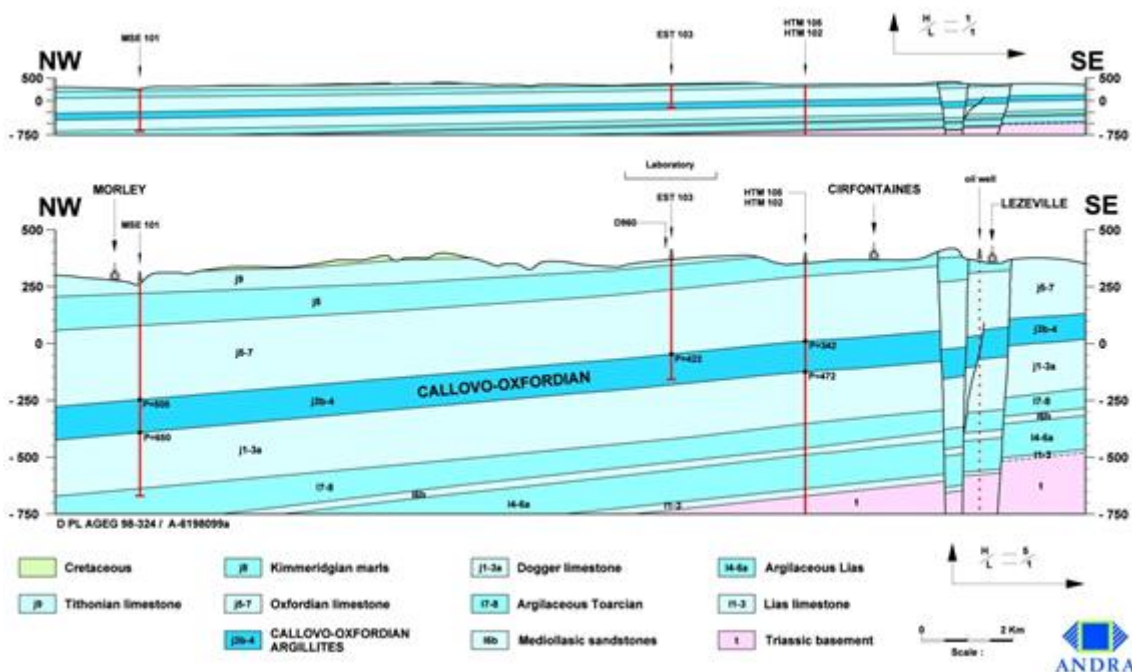


Fig. 3.1 Geological cross section of the Meuse/Haute Marne site /AND 05/

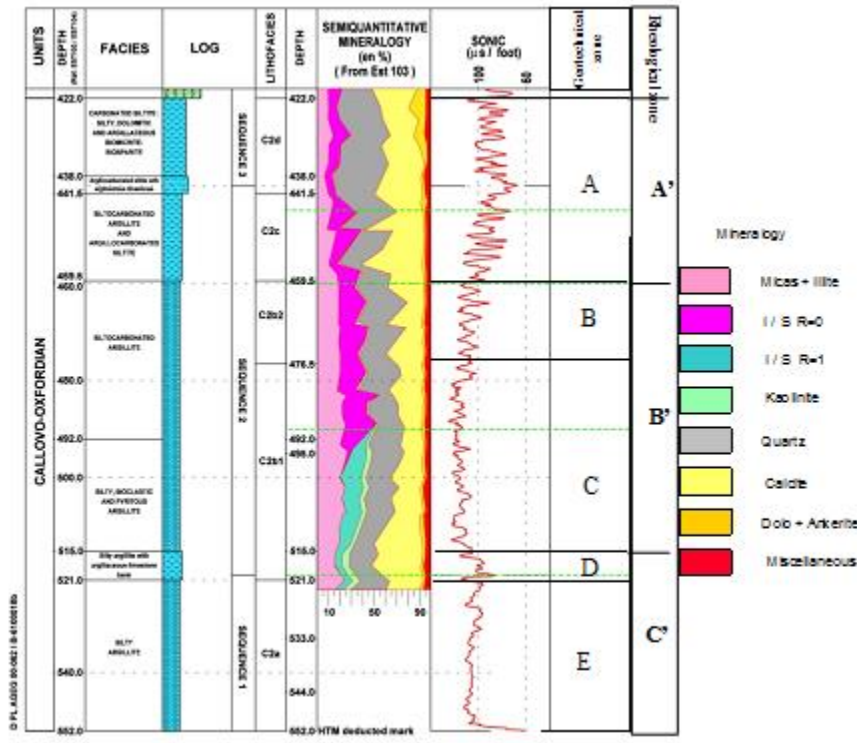


Fig. 3.2 Mineralogy of the Callovo-Oxfordian argillaceous formation /AND 05/

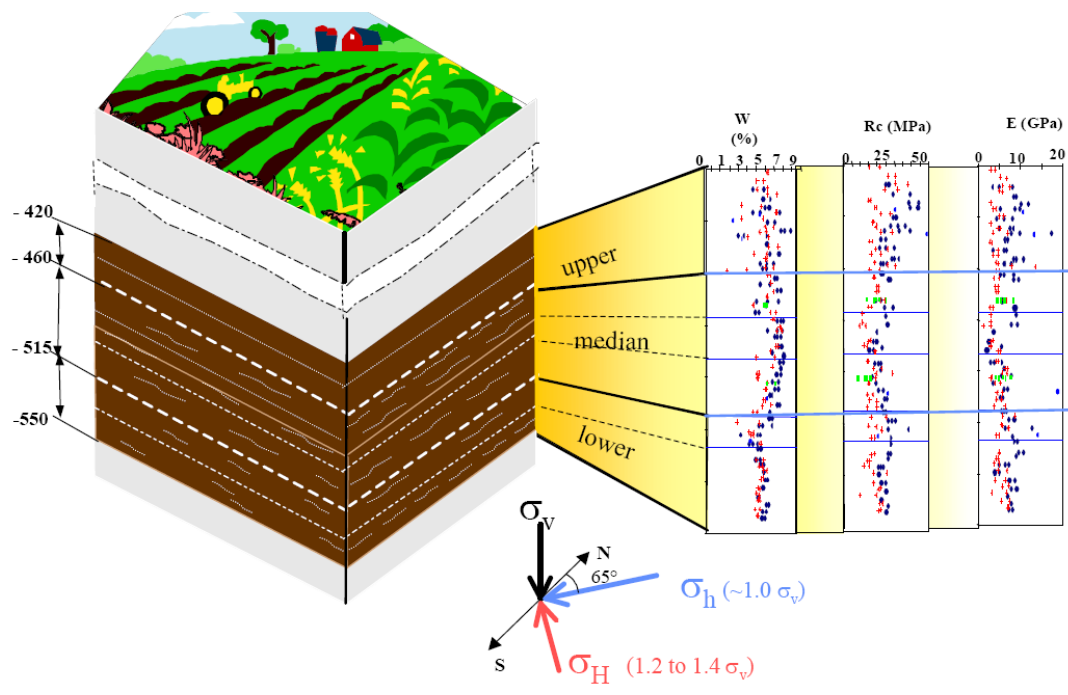


Fig. 3.3 Geomechanical properties of the Callovo-Oxfordian argillaceous formation /SU 07/

Tab. 3.1 Basic mechanical characteristics of the different geological zones of the Callovo-Oxfordian formation /AND 05/, /SU 07/

Characteristic	Rheological zone			Overall
	Upper	Median	Lower	
Depth (m)	420-455	455-515	515-550	420-550
Initial total stresses	12 – 16 MPa at -500 m			
Initial pore pressure	~5 MPa at -500 m			
Bulk density (g/cm ³)	2.42	2.42	2.46	2.40–2.45
Water content (%)	6.1	7.1	5.9	5.3-8.8
Porosity (%)	14.0	15.5	13.0	12.0-17.0
Young's modulus (GPa)	6.2	5.5	7.2	6.0
Uniaxial compressive strength (MPa)	30	21	21	24
Uniaxial tensile strength (MPa)				2.6
Hydraulic conductivity (m/s)	10 ⁻¹³ – 10 ⁻¹⁴			

On an average, the COX clay rock contains 25 – 55 % clay minerals, 20 – 38 % carbonates and 20 – 30 % quartz, 1 % feldspar, and small amounts of others /AND 05/. The three zones correspond to the three geological sedimentary sequences: two stiff zones (upper and lower) with higher carbonate contents surrounding a central less stiff zone (median) with more clay content. However, the transition from one zone to the other is progressive. The combined effect of the geological sedimentation, compaction and diagenesis has reduced the pore space to very low porosities of 12 – 17 %. The small pores lead to large resistance to fluid flow and correspondingly to very low hydraulic conductivities of 10⁻¹⁴ to 10⁻¹³ m/s. In the natural state, the clay rock is fully saturated with water and solutes (pore-water type: Na-Cl-SO₄) /MAZ 08/. The sedimentation has caused a preferential orientation of the clay foliation and consequently a stratification of the matrix structure. This however results in anisotropy of the rock

properties, for instance, the anisotropy factor of the hydraulic conductivity parallel versus normal to the bedding plane ranges from 2 to 10 /AND 05/. The *in situ* stress state at the -490 m main level of the MHM-URL is also anisotropic, the vertical component $\sigma_v = 12.7$ MPa, the minor horizontal component $\sigma_h = 12.4$ MPa (oriented $065^\circ \pm 10^\circ$), and the major horizontal component $\sigma_H = 14.8$ MPa (oriented $155^\circ \pm 10^\circ$).

3.2 Test Design of the second in-situ heating experiment (TED)

Heat released from high-level radioactive waste is dissipated through the buffer and the surrounding rock. The resulting temperature changes may affect the mechanical and hydraulic processes in the multi-barrier-system and even their barrier-properties.

To study the thermo-hydro-mechanical effects of the early thermal phase on the clay host rock, ANDRA has performed an in-situ heating test called TED experiment. The aim of the TED experiment is to measure the evolution of the temperature, deformation and pore pressure field around several heaters and to back-analyse the thermo-hydro-mechanical properties of the rock. The TED experiment was also designed to estimate the overpressure generated by heat in the zero flux plane between several heaters and to study the evolution of the damaged zone due to heating. The analysis of the experimental results should help in calibrating the numerical models which will be applied to the disposal cell cases (see chapter 4.5) /CON 12a/.

Fig. 3.4 shows the layout of the test at the main level of the MHM-URL /AND 09/. Three heaters were installed in horizontal boreholes parallel to each other. In these boreholes (TED1201, TED1202 et TED1203) there is a casing all along the borehole. The void between the casing and the rock is filled with grout. For more information please see /CON11/.

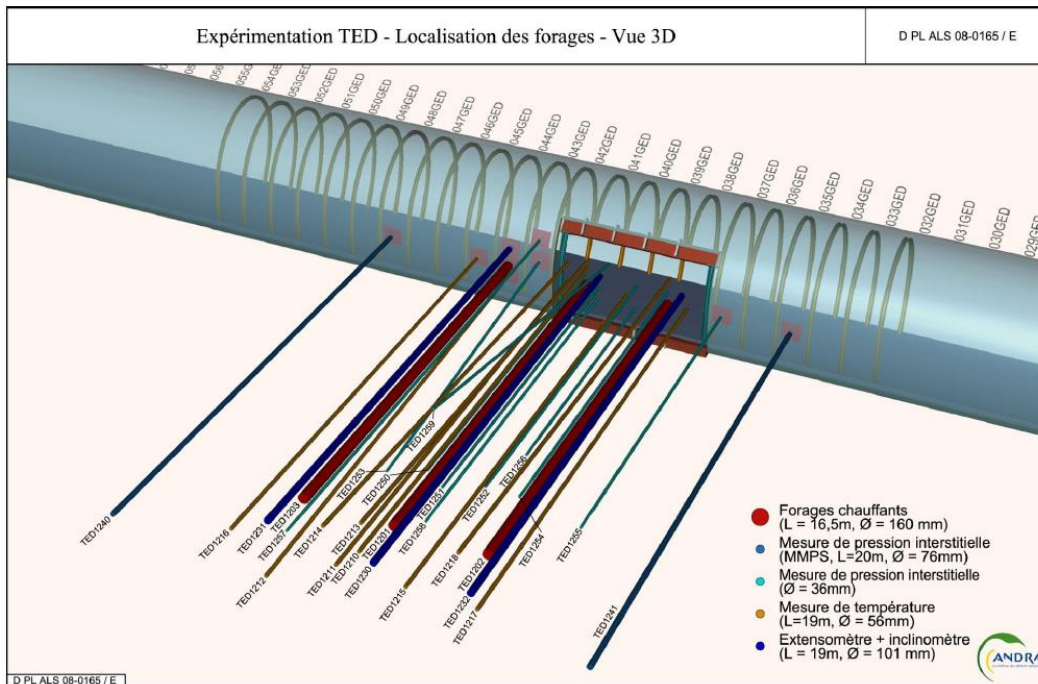


Fig. 3.4 Layout of the TED heating experiment with three heaters installed in horizontal boreholes showing also the measuring boreholes /AND 09/

In total, 23 boreholes have been instrumented to measure temperature, pore pressure and displacement. The main objectives were defined as 1) to enhance the knowledge about the THM behaviour of the clay rock, particularly thermal impact on EDZ development around HLW boreholes; 2) to validate the THM models and parameters; and 3) to provide a solid data base for design of a potential repository as well as for evaluation of the thermal impact on its long-term safety.

3.3 Test procedure

The first heating phase started in January 2010 with the stepwise power increase of the central heater TED 1201 for one year. The second heating phase followed in March 2011 with the two other heaters TED 1202 and TED 1203 to investigate effects of the additional thermal loads on pore-water pressure and deformation of the heated area. /CON 12a/.

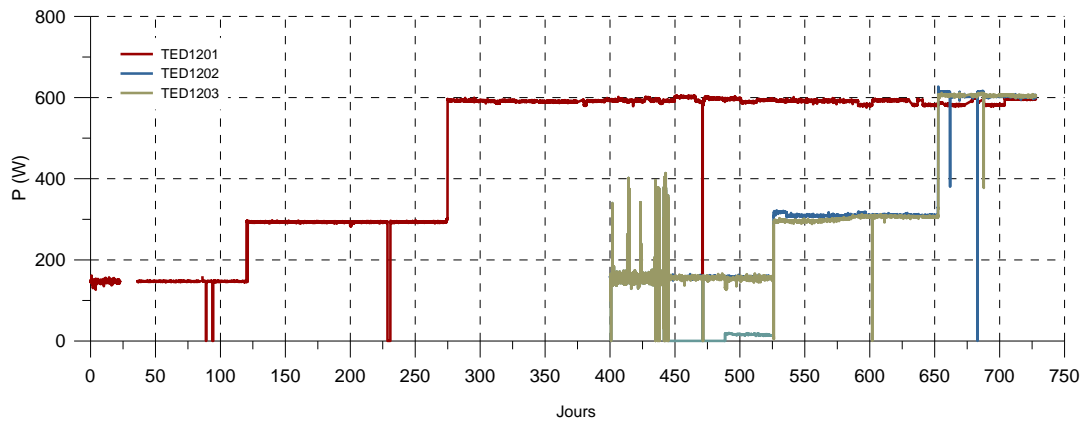
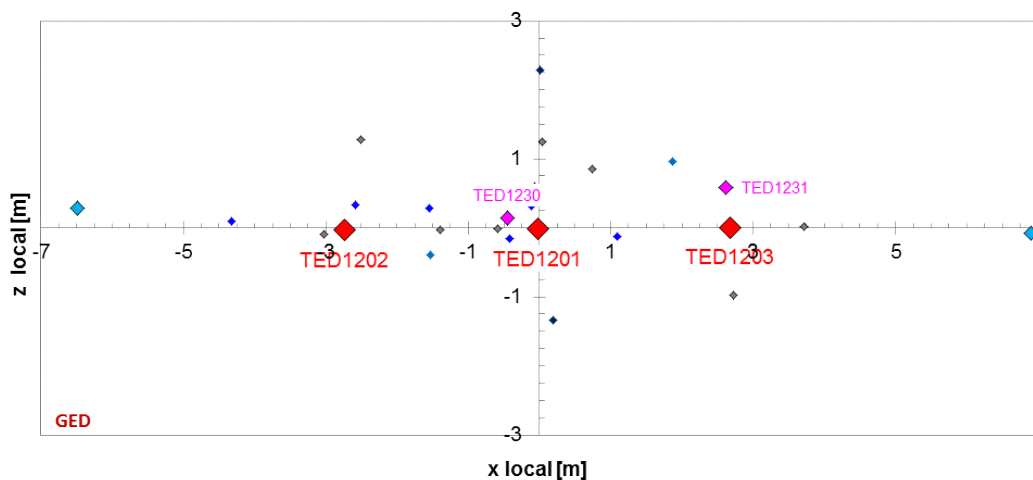


Fig. 3.5 TED heating procedure /CON 12a/

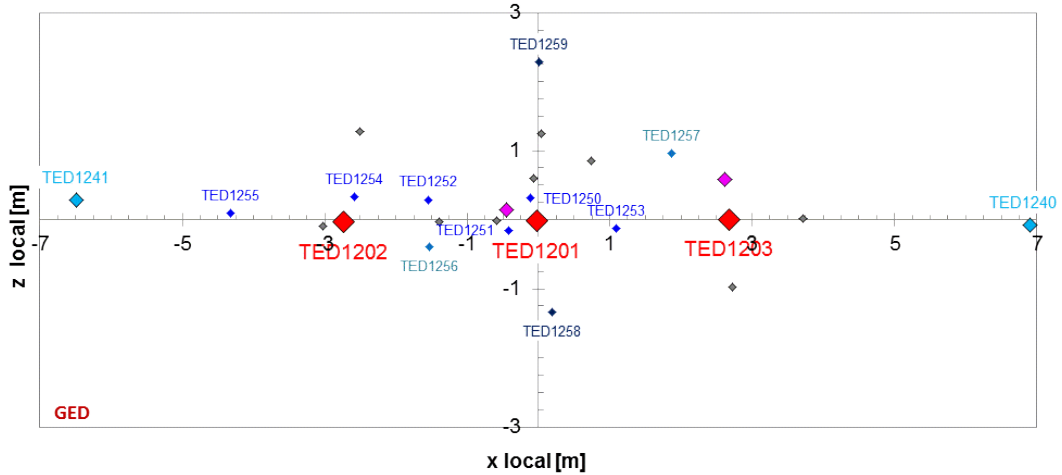
During the whole testing time several power cuts could be observed, Fig. 3.5. One uncertainty was clearly identified: the heating power in TED1203 is probably lower than expected between 29th May 2011 and 04th Sept. 2011. Finally, a cooling phase will be performed by switching off the heaters.

3.4 Measurement results

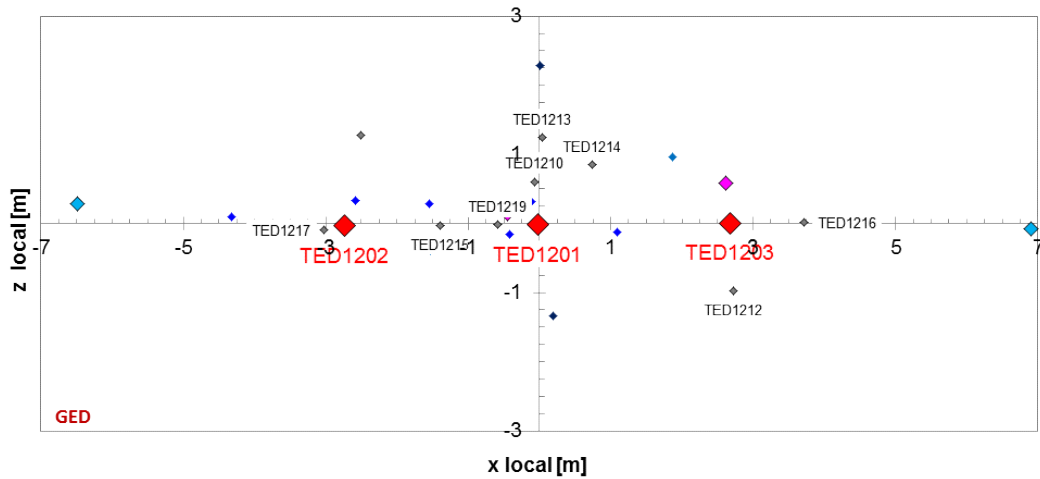
Figure 3.6 shows a sketch overview on the boreholes that were installed for measurement of temperature, pore pressure and deformation.



(a) Heating boreholes TED1201, 1202 and 1203 and boreholes TED1230 and 1231 with deformation measurements



(b) Boreholes TED1240 and 1241 with multi-packer-systems and boreholes TED1250 - 1259 with single packer system for pore pressure measurements



(c) Boreholes TED1210 and 1212 - 1219 for temperature measurements

Fig. 3.6 TED heating boreholes and boreholes for measurement of temperature, pore pressure and deformation

The following figures give an impression of the measurement data for the temporal evolution at the different heating boreholes TED1201 (Fig. 3.7), TED1202 (Fig. 3.8) and TED1203 (Fig. 3.9). With respect to the sensor location and the contact between the individual sensors and the casing along borehole TED1201, the temperature data show a deviation of 20 °C within the third heating phase and a maximum value of 120 °C. The sensors at greater distance to the heater element show values below 40 °C even after more than 700 days of heating.

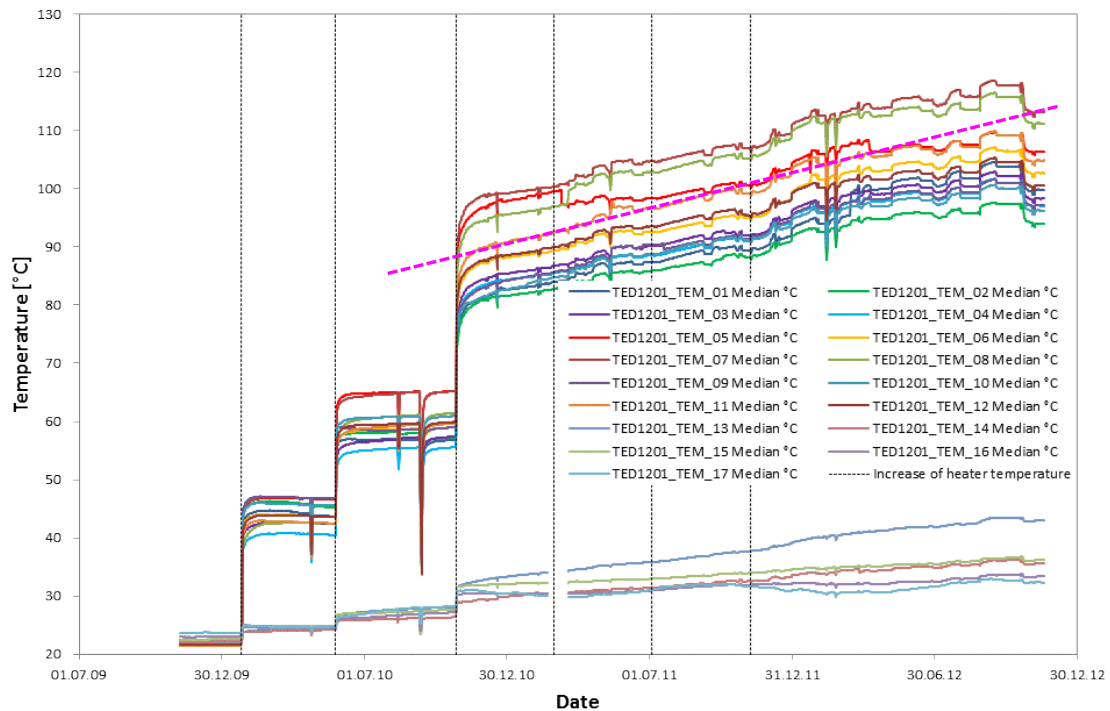


Fig. 3.7 In-situ measurement data for temperature evolution at heating borehole TED1201

From Fig. 3.7 it is not quite clear whether the temperature field reaches a steady state within the first two heating steps, but when additional thermal load is applied to the boreholes TED1202 and TED1203 the temperature values for TED1201 show a linear temperature increase, which could be identified within the third heating phase. Unfortunately, several power cuts occurred during the whole testing time, see also Fig. 3.5.

These events also affect the trend of the measured data, Fig. 3.8 and Fig. 3.9. Concerning borehole TED1202, it has to be noticed that from the beginning of the second thermal load level the sensors failed and the measured temperature values given in Fig. 3.8 do not reflect the actual temperature field in the surrounding rock. For more information please see /CON11/ and /CON 12b/.

Nevertheless, the measurement results for temperature and pore pressure evolution of selected sensors are given here to provide a first overview of the system evolution.

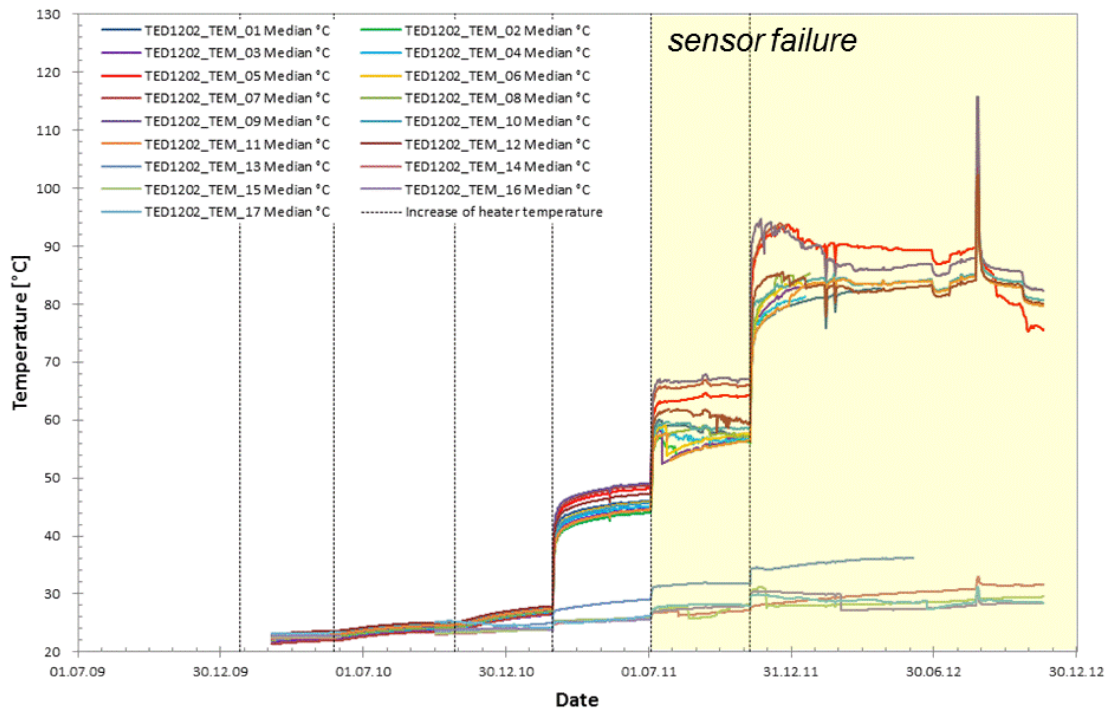


Fig. 3.8 In-situ measurement data for temperature evolution at heating borehole TED1202 (sensor failure during second thermal load level)

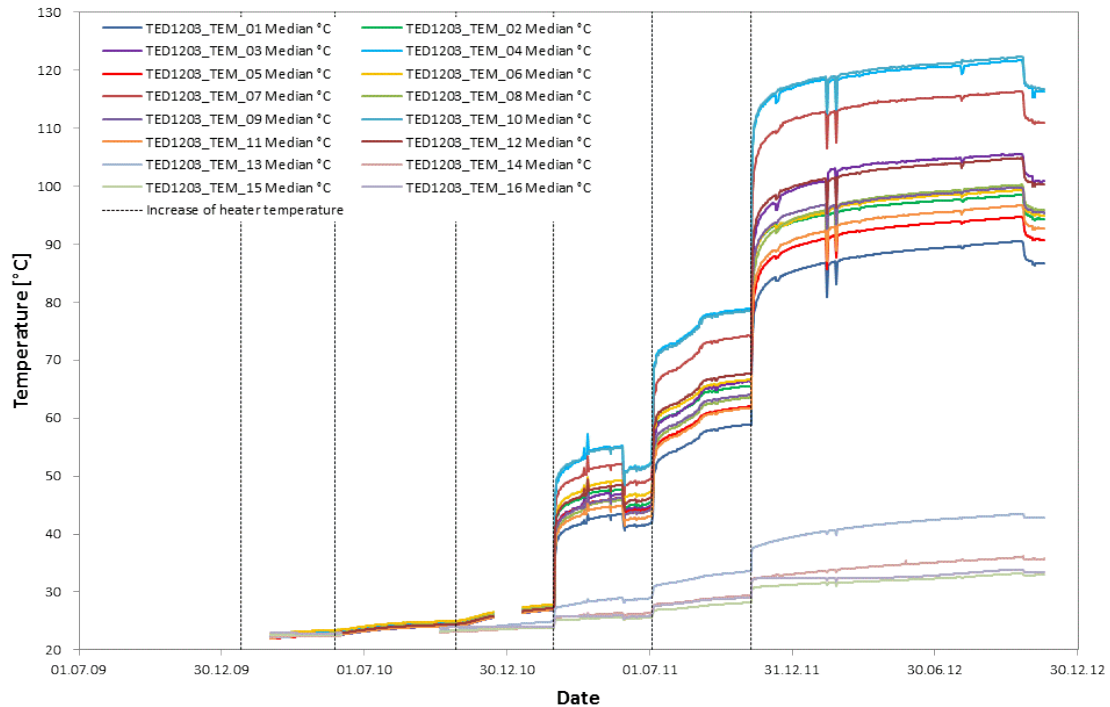


Fig. 3.9 In-situ measurement data for temperature evolution at heating borehole TED1203

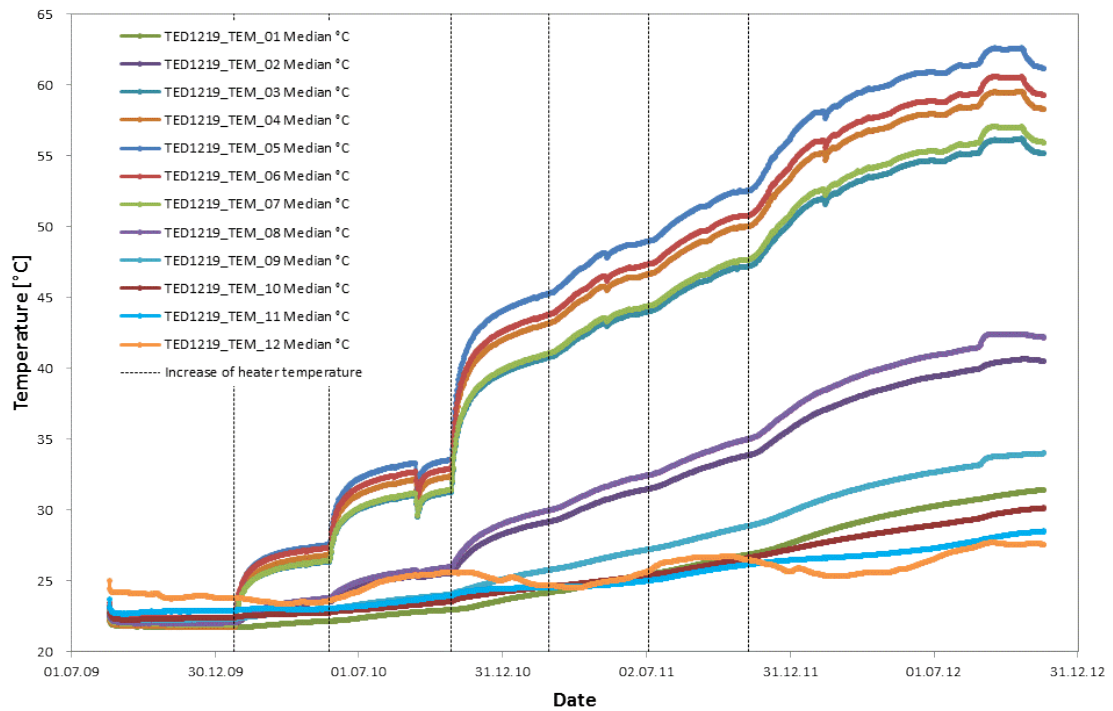


Fig. 3.10 In-situ measurement data for temperature evolution at borehole TED1219 (parallel to heating borehole TED1201)

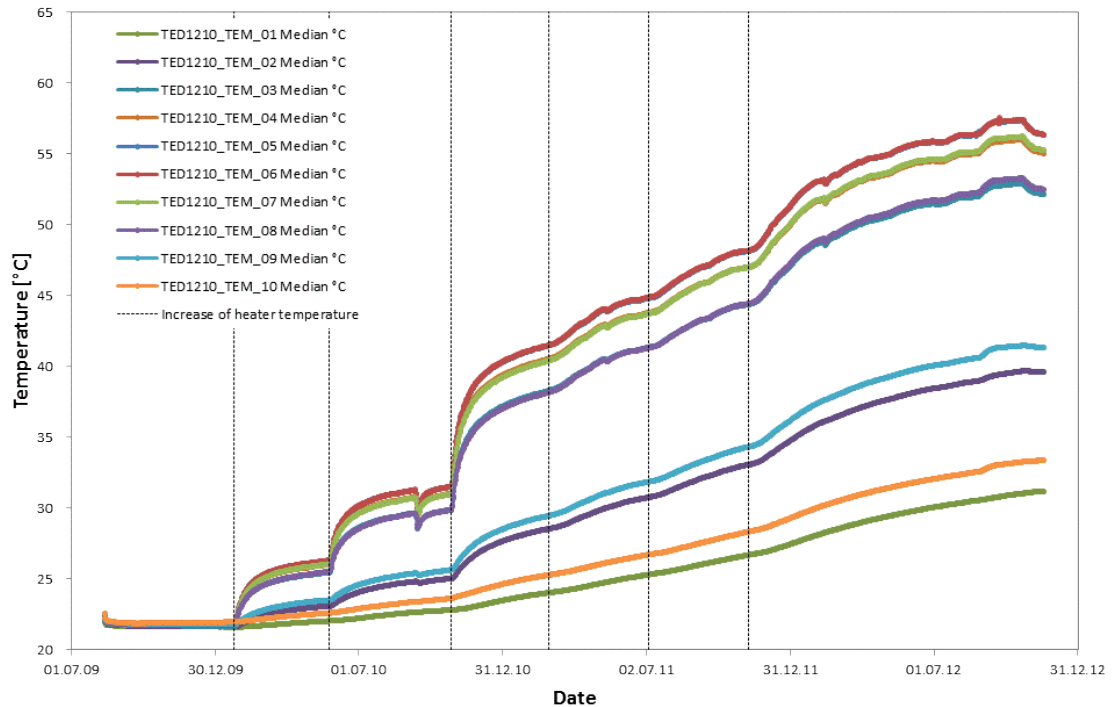


Fig. 3.11 In-situ measurement data for temperature evolution at borehole TED1210 (perpendicular to heating borehole TED1201)

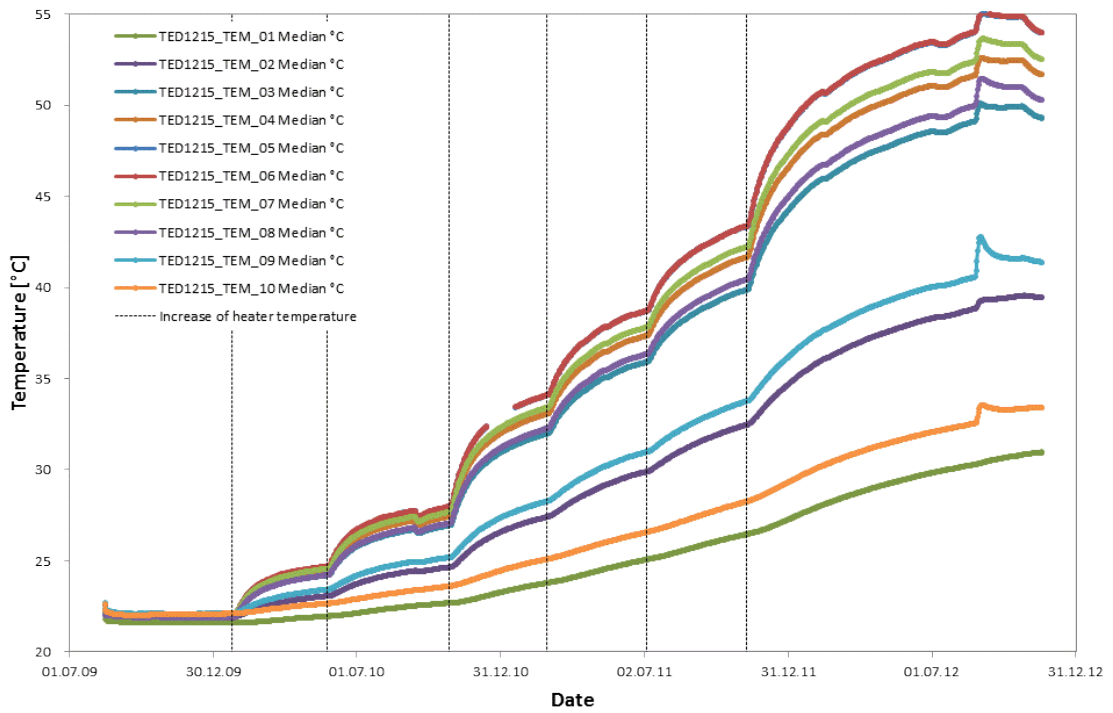


Fig. 3.12 In-situ measurement data for temperature evolution at borehole TED1215 (parallel to heating borehole TED1201)

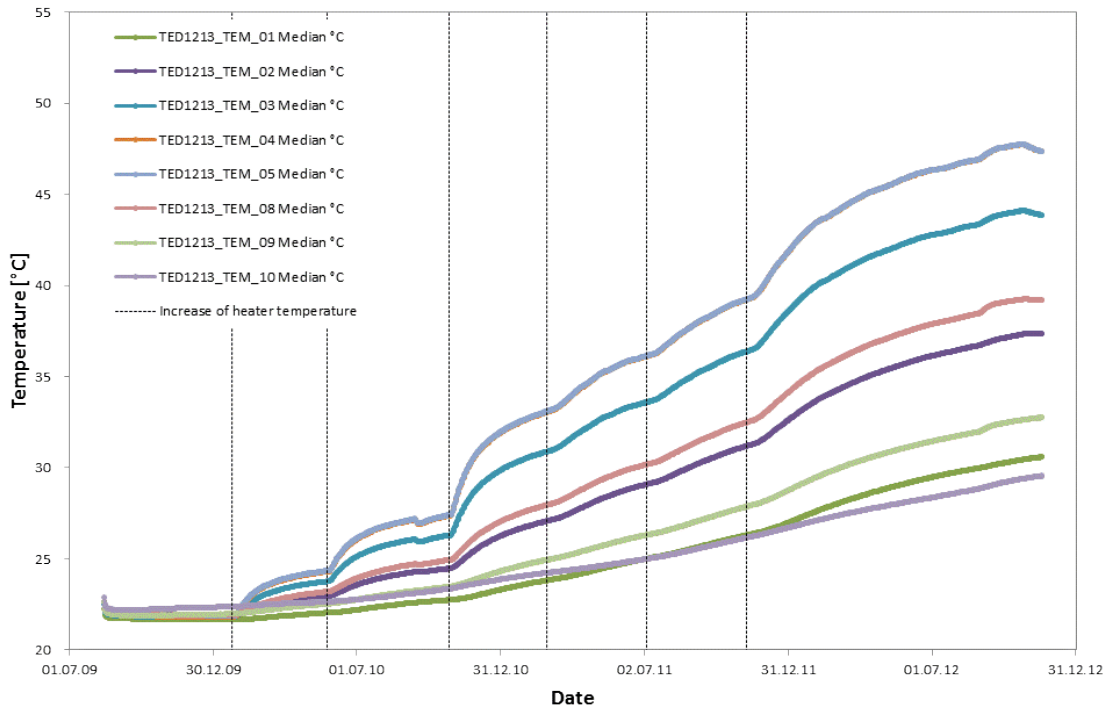


Fig. 3.13 In-situ measurement data for temperature evolution at borehole TED1213 (perpendicular to heating borehole TED1201)

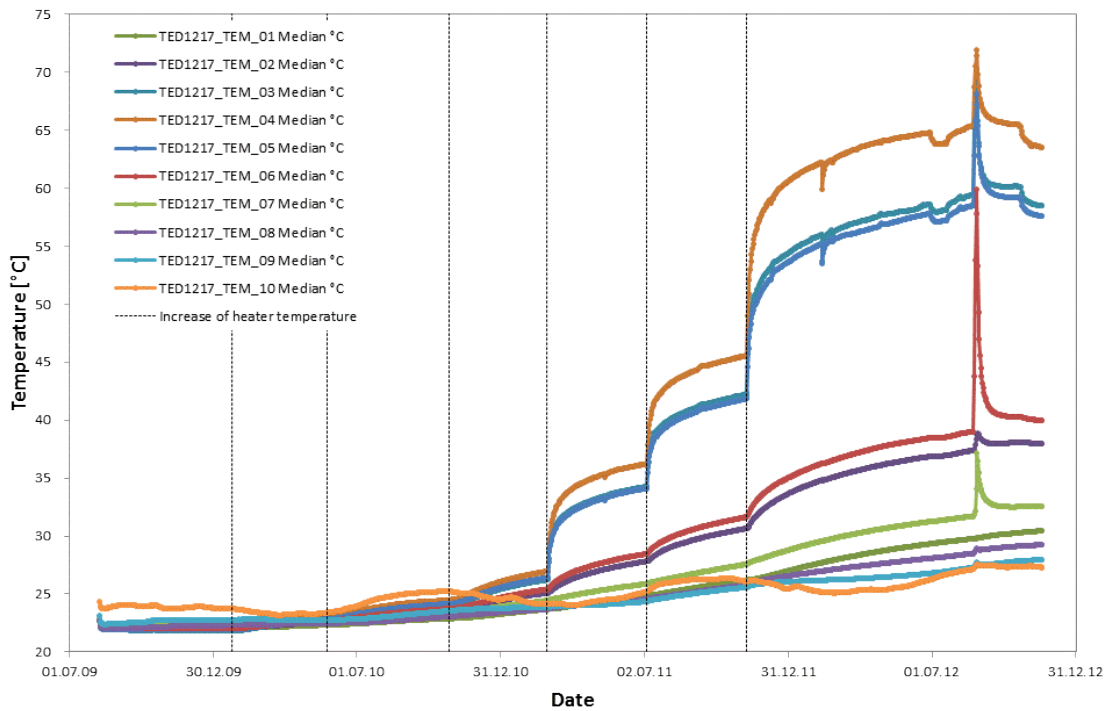


Fig. 3.14 In-situ measurement data for temperature evolution at borehole TED1217 (parallel to heating borehole TED1202)

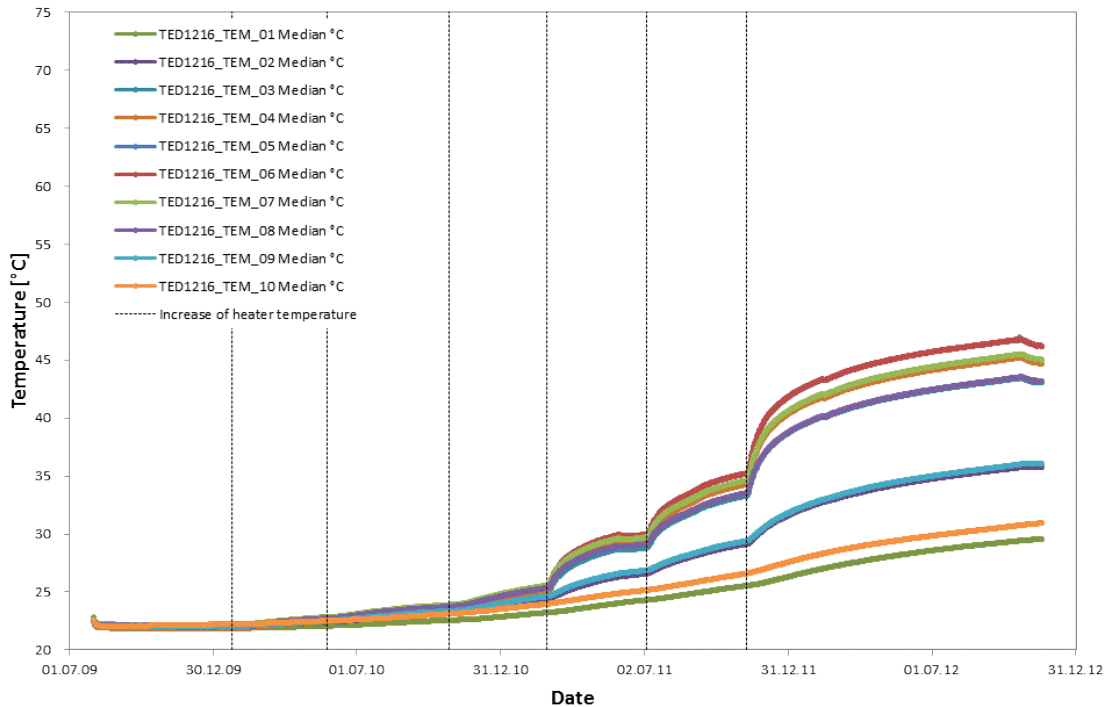


Fig. 3.15 In-situ measurement data for temperature evolution at borehole TED1216 (parallel to heating borehole TED1203)

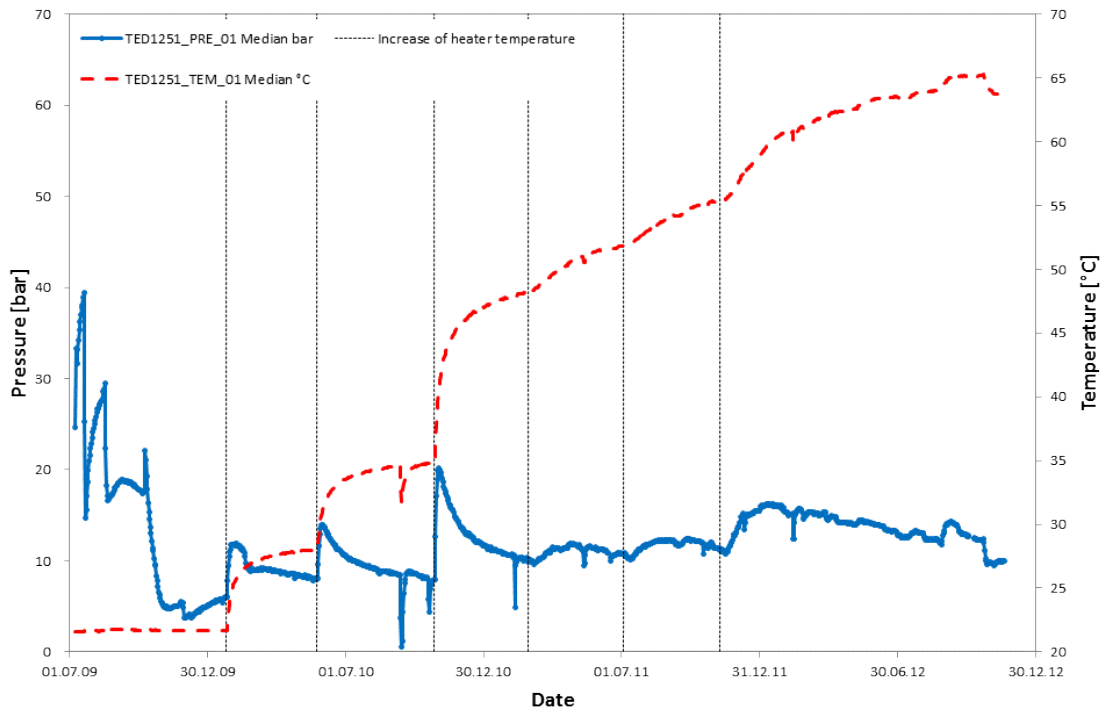


Fig. 3.16 In-situ measurement data for pore pressure/temperature evolution at borehole TED1251 (parallel to heating borehole TED1201)

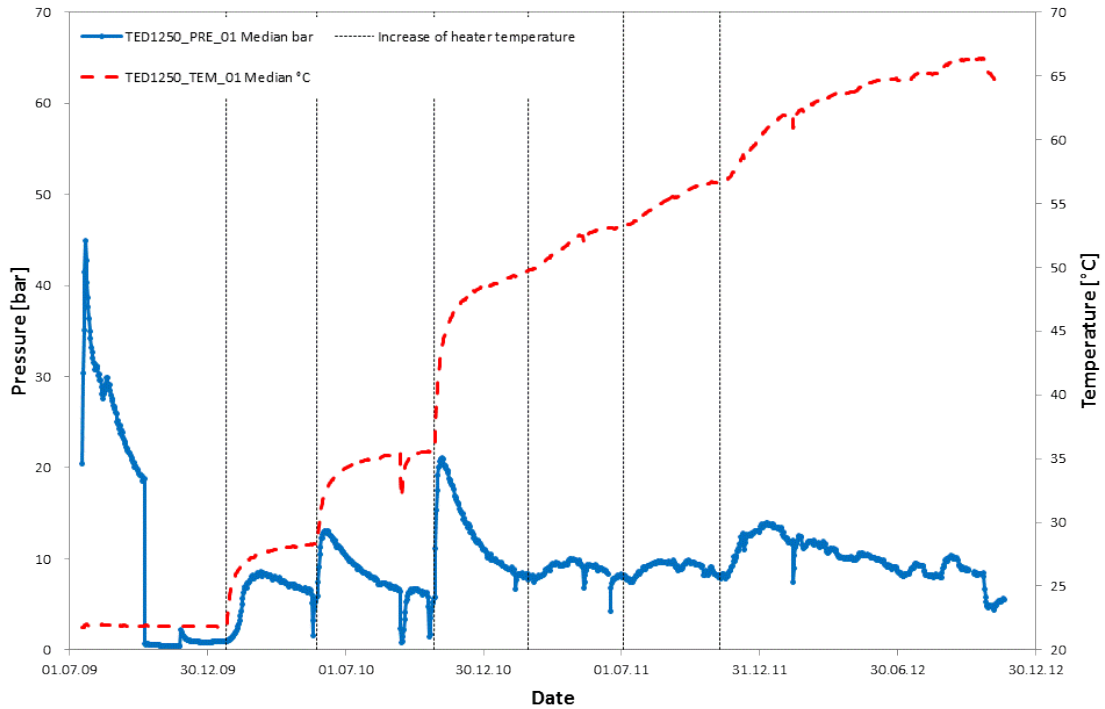


Fig. 3.17 In-situ measurement data for pore pressure/temperature evolution at borehole TED1250 (perpendicular to heating borehole TED1201)

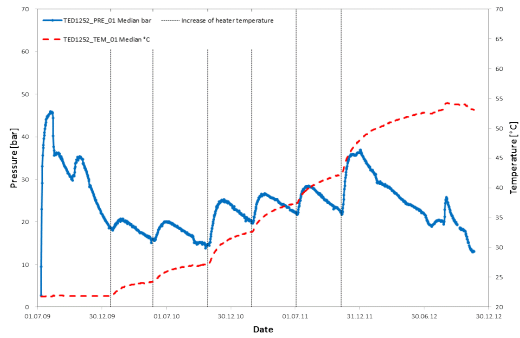


Fig. 3.18 TED1252 data

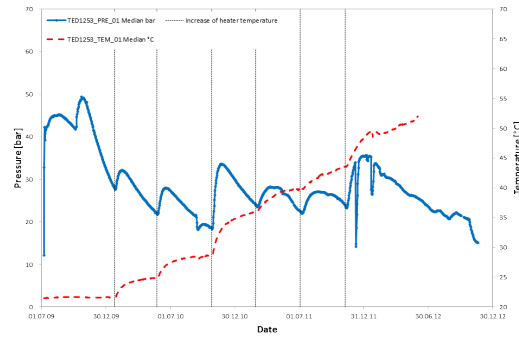


Fig. 3.19 TED1253 data

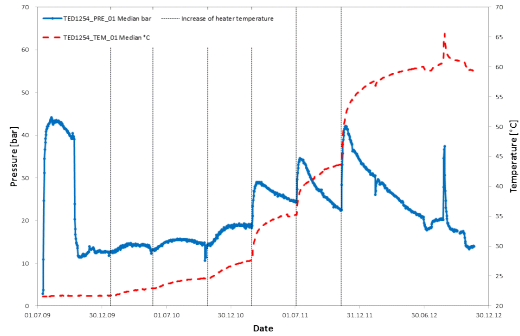


Fig. 3.20 TED1254 data

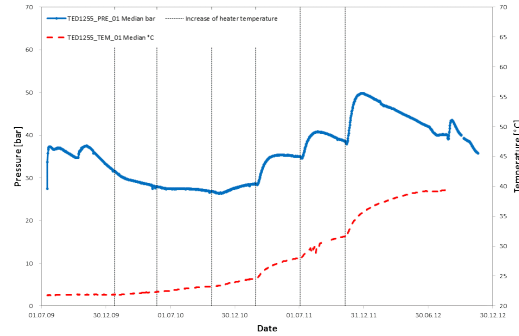


Fig. 3.21 TED1255 data

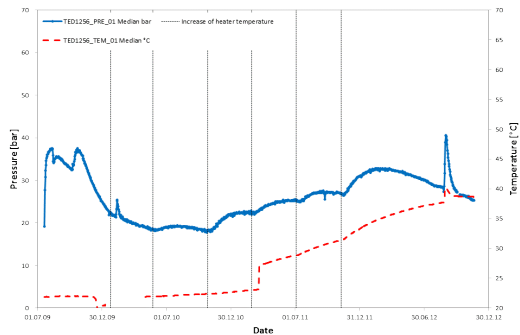


Fig. 3.22 TED1256 data

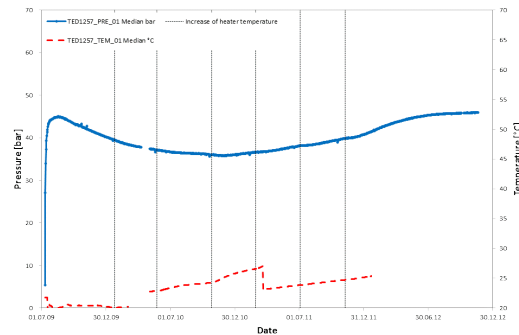


Fig. 3.23 TED1257 data

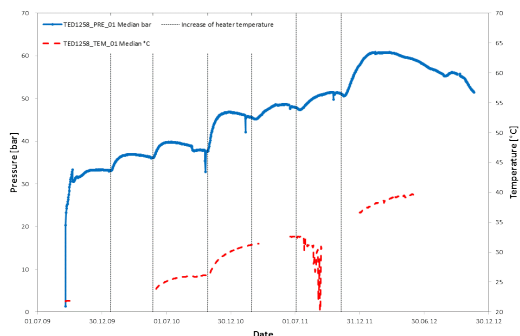


Fig. 3.24 TED1258 data

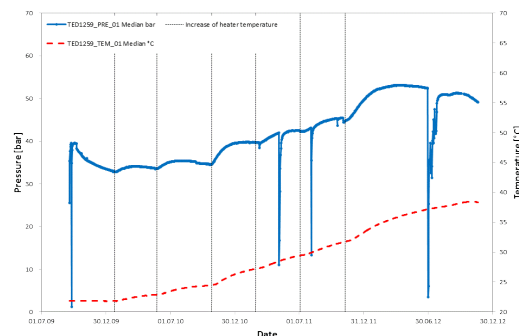


Fig. 3.25 TED1259 data

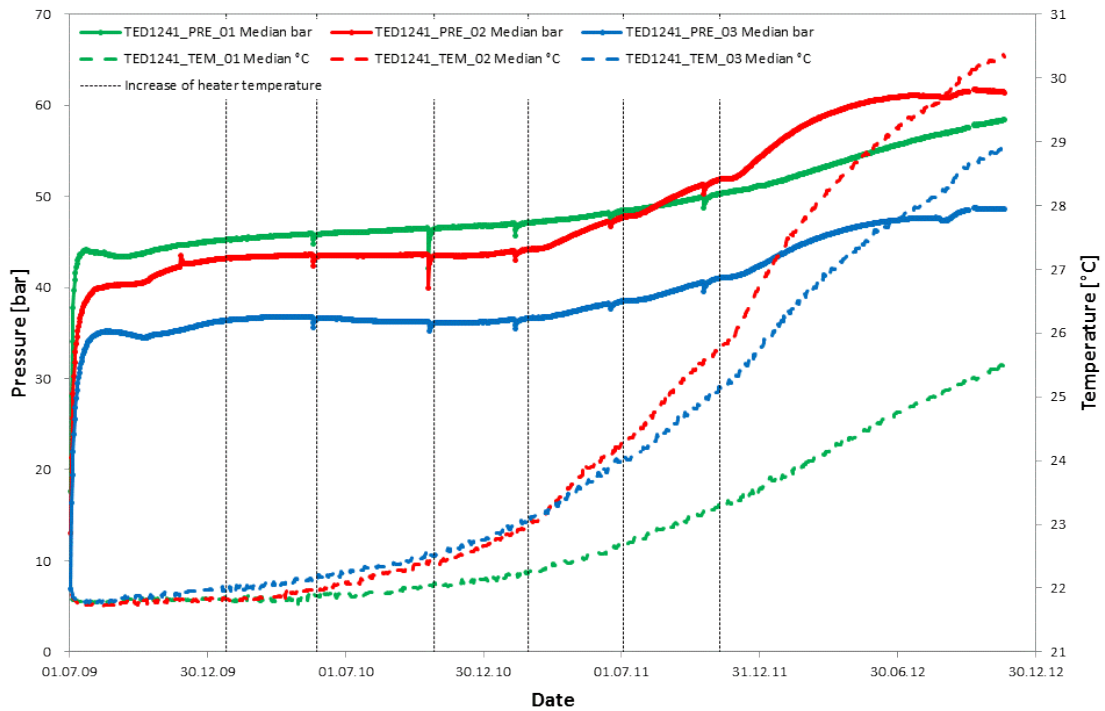


Fig. 3.26 In-situ measurement data for absolute pore pressure/temperature evolution at borehole TED1240 (parallel to heating borehole TED1203)

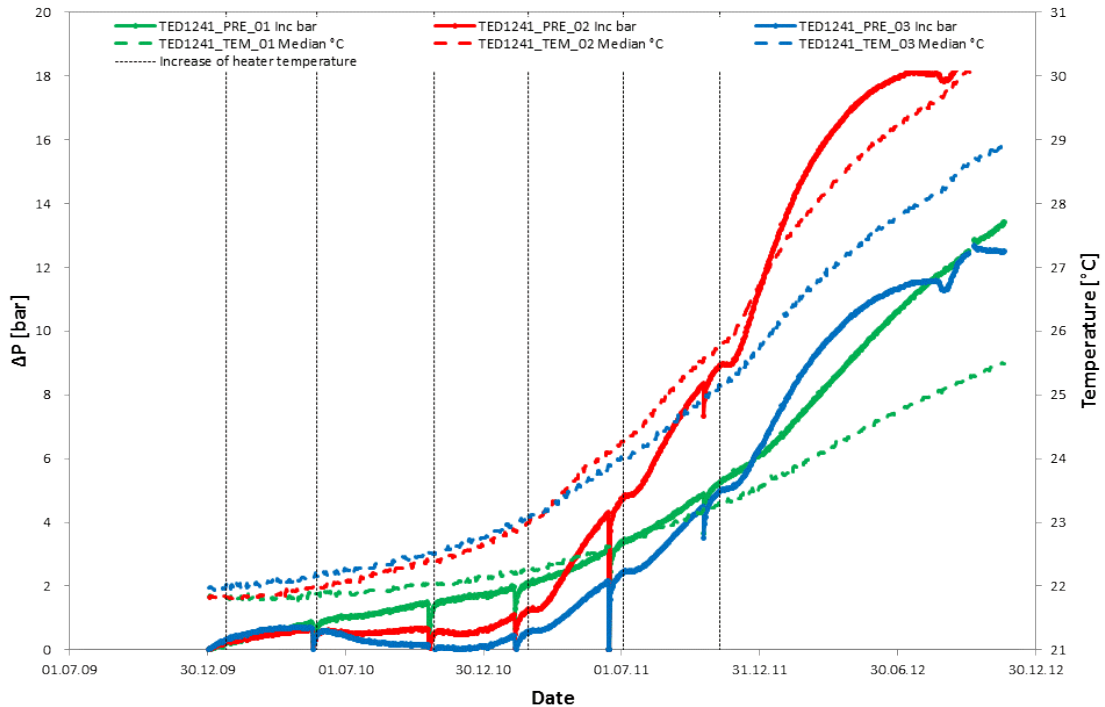


Fig. 3.27 In-situ measurement data for pore pressure increase at borehole TED1240 due to temperature evolution (effective data)

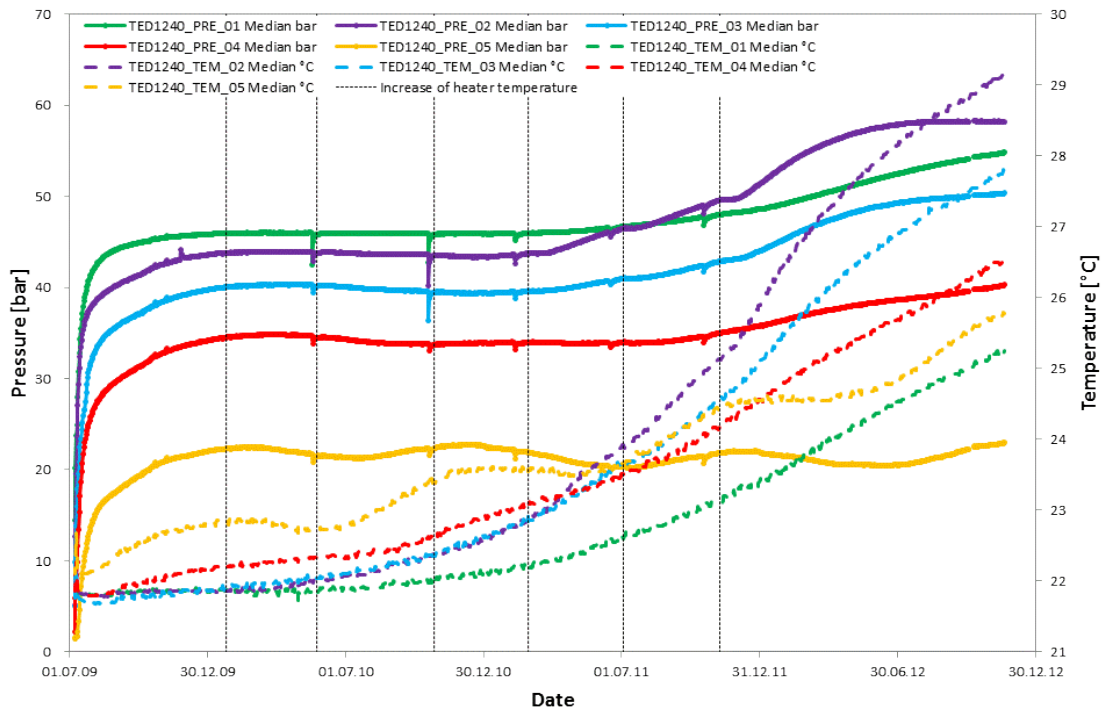


Fig. 3.28 In-situ measurement data for absolute pore pressure/temperature evolution at borehole TED1241 (parallel to heating borehole TED1202)

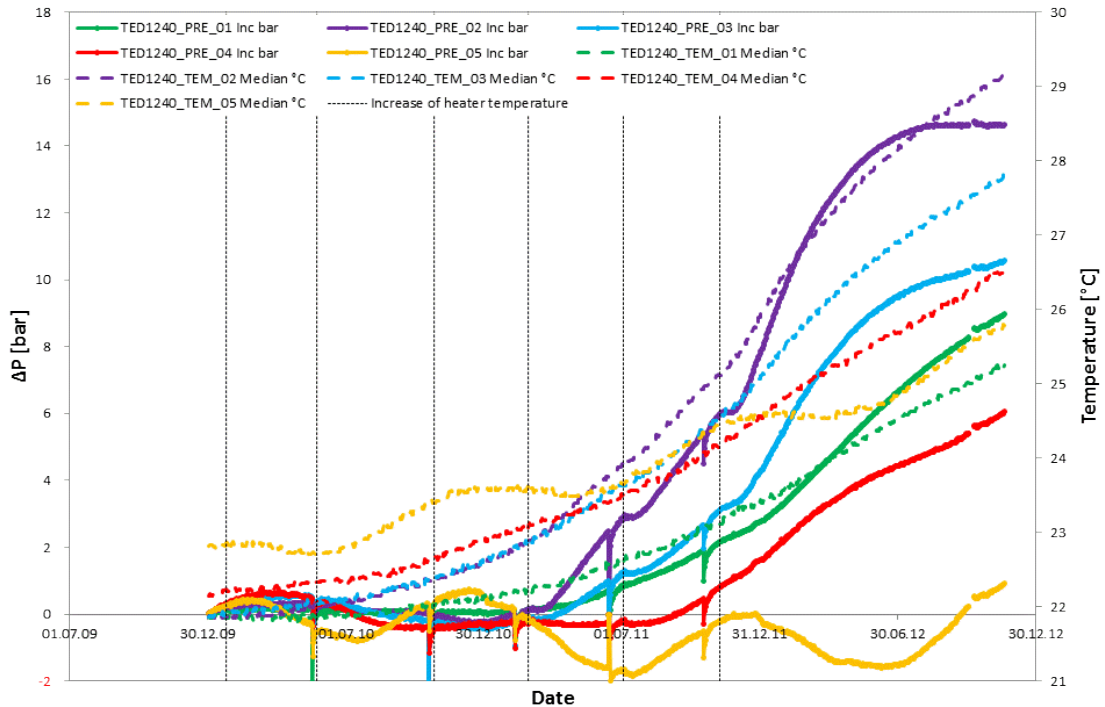


Fig. 3.29 In-situ measurement data for pore pressure increase at borehole TED1241 due to temperature evolution (effective data)

3.5 Conclusions drawn from the in-situ-experiment

The thermal impact on the COX claystone was experimentally studied and the results are summarized in the related status report /ZHA 2013/. With respect to these results the in situ measurement data have to be evaluated. Concerning borehole TED1202, it has to be noticed that from the beginning of the second thermal load level the sensors failed and the measured temperature values given do not reflect the actual temperature field in the surrounding rock.

4 Modelling

To gain experience with numerical modelling of coupled hydro-mechanical processes in clays, a number of scoping calculations were performed by GRS /ZHA 04/, /ZHA 07/, /ZHA 08/ using the computer programme CODE_BRIGTH developed by the Geotechnical Engineering Department of the Technical University of Catalonia in Barcelona for analysis of coupled THM phenomena in geological media /UPC 02/.

4.1 Physical modelling

Regarding the tight coupling between fluid flow processes and mechanical deformation in argillaceous rock mass a simplified approach of the recently developed argillite model was used, taking into account the anisotropic primary stress field without any damaging process as well as anisotropic hydraulic and mechanical response in case of 3D modelling. Prior to introducing the results of the numerical simulation a brief description of the formulation and the capabilities of the code used in the analysis as well as the used constitutive model and the depending material parameters are presented.

4.1.1 Theoretical framework

The computer programme CODE_BRIGTH handles coupled thermo-hydro-mechanical problems in porous media. The theoretical framework is composed of three main parts:

- balance equations,
- constitutive equations and
- equilibrium restrictions.

The subscripts identify the phase ('s' for solid, 'l' for liquid and 'g' for gas). The superscripts indicate the species ('h' for mineral, 'w' for water and 'a' for air). The liquid phase may contain water and dissolved air, and the gas phase may be a mixture of dry air and water vapour. Thermal equilibrium between phases is assumed. This means that the three phases are at the same temperature. A general and detailed description is given in /OLI 96/ and in the code manual /UPC 02/, according to the aforementioned literature only a brief description is given in the following section.

4.1.2 Balance equations

The balance equations are established for the porous medium as a whole. The compositional approach is adopted to establish the mass balance equations. It consists of balancing the species rather than the phases. The mass balance of solid present in the medium is written as:

$$\frac{\partial}{\partial t}(\rho_s(1-n)) + \nabla \cdot (j_s) = 0 \quad (4.1)$$

where ρ_s is the mass of solid per unit volume of solid, j_s is the flux of solid, t is time and ∇ is the divergence operator.

Water is present in liquid and gas phases. The total mass balance of water is expressed as:

$$\frac{\partial}{\partial t}(\theta_l^w S_l n + \theta_g^w S_g n) + \nabla \cdot (j_l^w + j_g^w) = f^w \quad (4.2)$$

where θ_l^w and θ_g^w are the masses of water per unit volume of liquid and gas, respectively. S_α is the volumetric fraction of pore volume, occupied by the alpha phase ($\alpha = l, g$). j_l^w and j_g^w denote the total mass fluxes of water in the liquid and gas phases (water vapour), with respect to a fixed reference system. f^w is an external supply of water per unit volume of medium.

Dry air is present in liquid and gas phases. The total mass balance of dry air is expressed as:

$$\frac{\partial}{\partial t}(\theta_l^a S_l n + \theta_g^a S_g n) + \nabla \cdot (j_l^a + j_g^a) = f^a \quad (4.3)$$

where θ_l^a and θ_g^a are the masses of dry air per unit volume of liquid and gas, respectively. S_α is the volumetric fraction of pore volume, occupied by the alpha phase ($\alpha = l, g$). j_l^a and j_g^a denote the total mass fluxes of dry air in the liquid and gas phases (water vapour), with respect to a fixed reference system. f^a is an external supply of dry air per unit volume of medium.

Thermal equilibrium between phases is assumed. This means that the three phases are at the same temperature. Consequently, the total internal energy, per unit volume

of porous media, is obtained adding the internal energy of each phase. Applying the balance equation to this quantity, the following equation is obtained:

$$\frac{\partial}{\partial t} (E_s \rho_s (1 - \phi) + E_l \rho_l S_l \phi + E_g \rho_g S_g \phi) + \nabla \cdot (\mathbf{j}_c + \mathbf{j}_{E_s} + \mathbf{j}_{E_l} + \mathbf{j}_{E_g}) = f^E \quad (4.4)$$

where E_s is the solid specific internal energy; E_l and E_g are specific internal energies corresponding to liquid and gas phase, respectively, ρ_s is the solid density; ρ_l and ρ_g are the liquid and gas phase densities; \mathbf{j}_c is the conductive heat flux; \mathbf{j}_{E_s} is the advective energy flux of solid phase with respect to a fixed reference system; \mathbf{j}_{E_l} and \mathbf{j}_{E_g} are the advective energy flux of liquid and gas phases, respectively, with respect to a fixed reference system; f^E is the energy supply per unit volume of medium.

The balance of momentum for the porous medium reduces to the equilibrium equation in total stresses:

$$\nabla \cdot \boldsymbol{\sigma} + \mathbf{b} = 0 \quad (4.5)$$

where $\boldsymbol{\sigma}$ is the stress tensor and \mathbf{b} is the vector of body forces.

4.1.3 Equilibrium restrictions

Equilibrium restrictions are given for the concentration of water vapour in gas and of dissolved air in water. The mass of water vapour per unit volume of gas (θ_g^w) is determined via the psychrometric law:

$$\theta_g^w = (\theta_g^w)^0 \exp \left[\frac{-(P_g - P_l) M_w}{R(273.15 + T) \rho_l} \right] \quad (4.6)$$

where P_l and P_g are liquid and gas pressures, respectively, $(\theta_g^w)^0$ is the vapour density in the gaseous phase in contact with a planar surface (i. e. when $P_g - P_l = 0$), M_w is the molecular mass of water (0.018 kg/mol), R is the gas constant (8.314 J/mol·K) and T is the temperature (in degree Celsius). $(\theta_g^w)^0$ is depending on temperature. The vapour partial pressure is computed by means of the ideal gas law.

The solubility of air in water is controlled by Henry's law:

$$\omega_1^g = \frac{P_a}{H} \cdot \frac{M_a}{M_w} \quad (4.7)$$

where ω_1^g is the mass fraction of air in the liquid, P_a is the partial pressure of air, M_a is the molecular mass of air (0.02895 kg/mol) and $H = 10000$ MPa is Henry's constant. According to the definition of partial density, $\theta_1^w = \omega_1^g \cdot \rho_1$.

4.1.4 Constitutive equations

The constitutive equations establish the link between the independent variables and the dependent variables. Concerning the hydraulic problem it is assumed that the liquid and gas flow follows Darcy's law:

$$q_\alpha = -\mathbf{K}_\alpha (\nabla P_\alpha - \rho_\alpha \mathbf{g}) \quad (4.8)$$

where $\mathbf{K}_\alpha = \mathbf{k} k_{r\alpha} / \mu_\alpha$ is the permeability tensor. The intrinsic permeability tensor (\mathbf{k}) depends on the pore structure of the porous medium. $k_{r\alpha}$ is the value of relative permeability that controls the variation of permeability in the unsaturated regime and μ_α denotes the dynamic viscosity. α stands either for l or g depending on whether liquid or gas flow is considered. \mathbf{g} is the gravity vector. The variation of intrinsic permeability with porosity is given by:

$$\mathbf{k} = \mathbf{k}_0 \cdot \frac{\phi^3}{(1-\phi)^2} \cdot \frac{(1-\phi_0)^2}{\phi_0^3} \quad (4.9)$$

where ϕ_0 is a reference porosity. The relative permeabilities of the liquid and gaseous phases are dependent on the degree of liquid saturation according to:

$$S_e = \frac{S_l - S_{lr}}{S_{ls} - S_{lr}} \quad (4.10)$$

and

$$k_{rl} = A \cdot S_e^\lambda \quad (4.11a)$$

$$k_{rg} = 1 - k_{rl} \quad (4.11b)$$

where S_l , S_{lr} , S_{ls} , S_e are the actual, residual, maximum and effective saturation of liquid, respectively, and A and λ are parameters.

It is necessary to define the retention curve of the materials relating to the degree of saturation to suction ($P_g - P_l$). The expression of Van Genuchten is selected:

$$S_e = \left[1 + \left(\frac{P_g - P_l}{P} \right)^{1/(1-\beta)} \right]^{-\beta} \quad (4.12)$$

where $P_g - P_l \geq 0$ and $P = P_0 \cdot \frac{\sigma}{\sigma_0}$; P_0 is a material parameter.

The molecular diffusion of vapour is governed by Fick's law:

$$\mathbf{i}_g^w = -\mathbf{D}_g^w \nabla \omega_g^w = -(\phi \rho_g S_g \tau \mathbf{D}_m^w \mathbf{I} + \rho_g \mathbf{D}'_g) \cdot \nabla \omega_g^w \quad (4.13)$$

where \mathbf{i}_g^w is the non advective mass flux of water in gas, \mathbf{D}_g^w is the dispersion tensor, ω_g^w is the mass fraction of water in gas, τ is the tortuosity and \mathbf{D}'_g is the mechanical dispersion tensor. Usually, a constant dispersion coefficient corresponding to the molecular diffusion of vapour in air is assumed:

$$D_m^w = \tau D \left(\frac{(273.15+T)^n}{P_g} \right) \quad (4.14)$$

where P_g is given in MPa. For τ a value equal to 0.8, for n a value of 2.3 and for D a value of 5.9E-12 has been adopted. \mathbf{D}'_g can be neglected if air flow is insignificant.

In saturated porous materials, mechanical behaviour is best understood in terms of effective stress $\boldsymbol{\sigma}' = \boldsymbol{\sigma} - P_l \mathbf{m}$, where \mathbf{m}^T is an auxiliary vector [1,1,1,0,0,0]. For unsaturated materials it is necessary to consider two independent stress variables: net stresses ($\boldsymbol{\sigma} - P_l \mathbf{m}$) and capillary suction $s = (P_g - P_l)$. The net stress is the excess of total stress over gas pressure. If full saturation is achieved, net stress becomes effective stress. The mechanical constitutive equation takes the incremental form:

$$d\boldsymbol{\sigma}' = \mathbf{D}d\boldsymbol{\varepsilon} + \mathbf{h}ds \quad (4.15)$$

where $\boldsymbol{\sigma}'$ is now used for net stresses, $\boldsymbol{\varepsilon}$ is the strain sensor. \mathbf{D} is the constitutive stiffness matrix, defined by Young's modulus E_i , shear modulus G and Poisson's ratio ν_i through the classical orthotropic linear elasticity with i depending on bedding plane orientation and \mathbf{h} is a constitutive vector relating changes of suction to changes in net stress.

For the Barcelona Basic Model (BBM) as the yield function a classical Modified Cam-Clay model is taken:

$$q^2 - M^2(p' + p_s)(p_o - p') = 0 \quad (4.16)$$

where M is a constant value characterising the critical failure state line

$$q = Mp' \quad (4.17)$$

where q is the deviatoric stress.

It is assumed that the apparent cohesion increases with suction by

$$p_s = p_{s_o} + k \cdot s \quad (4.18)$$

where p_{s_o} is the tensile strength in saturated conditions, k and p are parameters.

The net isotropic yield stress p_o is considered to be dependent on suction through

$$p_o = p^c \left(\frac{p_o^*}{p^c} \right)^{\frac{\lambda(o) - k_{i_o}}{\lambda(s) - k_{i_o}}} \quad (4.19a)$$

with

$$\lambda(s) = \lambda(o) [(1 - r) \exp(-\beta s) + r] \quad (4.19b)$$

where p_o^* is the net yield stress for saturated conditions, $\lambda(o)$, $\lambda(s)$ are the slopes of the virgin compression lines for saturated and unsaturated conditions, r is a constant related to the matrix stiffness, β provides the rate of change of $\lambda(s)$ with suction, k_{i_o} is the initial slope of the isotropic unloading-reloading paths for saturated conditions, p^c is a reference stress.

Hardening depends on plastic strain according to

$$\frac{dp_o^*}{p_o^*} = \frac{v}{\lambda(o) - k_{i_o}} d\varepsilon_v^p \quad (4.20)$$

where $v = 1 + e$ is the specific volume, e is the void ratio.

Volumetric elastic strains induced by changes of net mean stress and suction are given by

$$d\epsilon_v^e = d\epsilon_{vp}^e + d\epsilon_{vs}^e \quad (4.21a)$$

with

$$d\epsilon_{vp}^e = \frac{k_i}{v} \frac{dp'}{p'} \quad (4.21b)$$

$$k_i = k_{i0} (1 + \alpha_i s) \quad (4.21c)$$

$$d\epsilon_{vs}^e = \frac{k_s}{v} \frac{ds}{s + p_{at}} \quad (4.21d)$$

$$k_s = k_{s0} \left(1 + \alpha_{sp} \ln \left(\frac{p'}{p_{ref}} \right) \right) \exp(\alpha_{ss} s) \quad (4.21e)$$

where k_{i0} , k_i are the slopes of the isotropic unloading-reloading paths for saturated and unsaturated conditions, respectively, k_{s0} , k_s are the slopes of the wetting-drying paths for saturated and unsaturated conditions at a given stress p' in the elastic domain, p_{at} , p_{ref} are the atmospheric pressure and the reference pressure, α_i , α_{sp} , α_{ss} are parameters.

Deviatoric elastic deformations are computed through shear modulus G and the Poisson ratio ν :

$$d\epsilon_q^e = \frac{G}{3} dq \quad (4.22a)$$

with

$$G = \frac{3(1-2\nu)(1+e)}{2(1+\nu)} \frac{p'}{k_i} \quad (4.22b)$$

4.1.5 Material parameters

A number of parameters associated with the above equations are material specific parameters which are to be determined by laboratory and in situ experiments. Based on /ZHA 04/, /ZHA 07/, ZHA 08/ and /BOC 08/ the material parameters associated with the constitutive equations implemented in CODE_BRIGHT were determined for Opalinus clay and Callovo-Oxfordian Clay and used in the documented calculations. The values of the parameters are represented in Tab. 4.1 to 4.3.

Tab. 4.1 Physical properties determined Opalinus (OPA) clay and for Callovo-Oxfordian (COX) clay

Property	Symbol	Unit	OPA	COX
Grain density	ρ_s	kg/m ³	2710	2700
Dry density	ρ_d	kg/m ³	2340	2300
Void ratio	e_o	-	0.190	0.190
Porosity	ϕ_o	-	0.160	0.160
Water content	w_o	%	7.2	6.0
Initial suction	s_o	MPa	0	0
Degree of saturation	S_{I0}	%	100	100

Tab. 4.2 Hydraulic parameters determined Opalinus (OPA) clay and for Callovo-Oxfordian (COX) clay, associated with the constitutive equations

Parameter in equation	Symbol	Unit	OPA	COX
(4.9)	ϕ_o	-	0.16	0.16
(4.9)	k_o	m ²	$2 \cdot 10^{-20}$	$10^{-19} / 10^{-20}$
(4.10)	S_{I_r}	-	0.01	0.01
(4.10)	S_{I_s}	-	1.0	1.0
(4.11a)	A	-	1	1
(4.11a)	λ	-	5	5
(4.12)	β	-	0.4	0.37
(4.12)	P_o	MPa	20	28
(4.14)	τ	-	0.8	0.8

Tab. 4.3 Mechanical parameters determined for Opalinus (OPA) clay and for Callovo-Oxfordian (COX) clay, associated with the constitutive equations

Parameter in equation	Symbol	Unit	OPA	COX
(4.21c)	k_{io}	-	0.0035	0.0035
(4.21c)	α_i	-	0	0
(4.21e)	k_{so}	-	$4 \cdot 10^{-5}$	$4 \cdot 10^{-5}$
(4.21e)	α_{sp}	-		
(4.21e)	α_{ss}	MPa ⁻¹		
(4.21e)	p_{ref}	MPa		
(4.22b)	ν	-	0.33	0.30
Bulk modulus	K	MPa	3500	5830
Shear modulus	G	MPa	1340	2690
Young's modulus	E	MPa	3570	7000
(4.17)	M	-	1.5	1.5
(4.18)	k	-	-0.007	-0.007
(4.19a)	p^c	MPa	0.1	0.1
(4.19a)	p_o^*	MPa	20.0	20.0
(4.19a)	$\lambda(o)$	-	0.027	0.027
(4.19b)	r	-	0.6	0.6
(4.19b)	β	MPa ⁻¹	0.015	0.015

4.2 MB experiment

4.2.1 Numerical model

A 3-dimensional model with 40 m in height and in width was used for the numerical simulation (Fig. 4.1). In the centre of the model the MB niche is located. The Gallery 08 was abstracted and modelled as a part of the MB niche of 3 m in length to keep the model geometry simple.

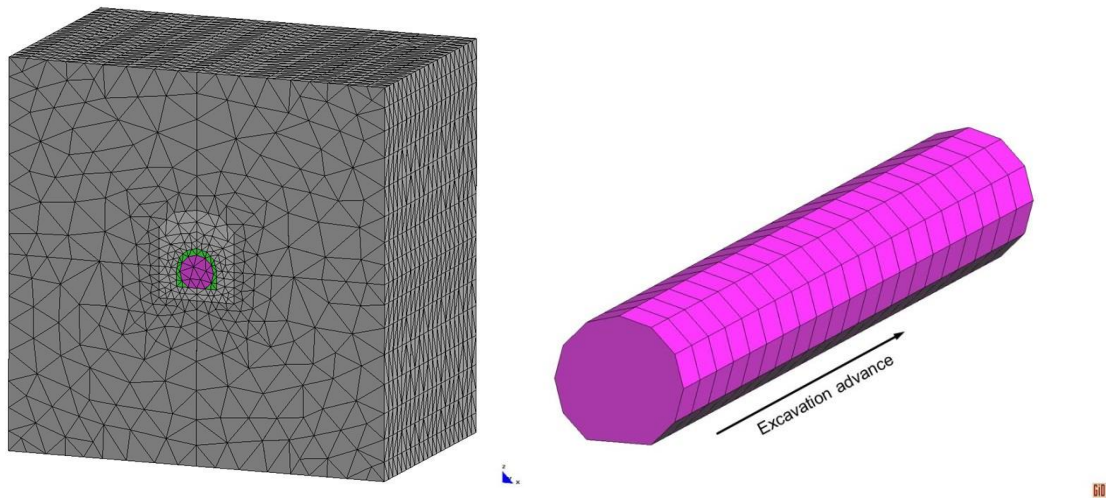


Fig. 4.1 FE model (3D) used for numerical simulation of the Mine-by test (left: full model, right: excavation steps)

The simulation process goes along with the realistic time schedule as far as possible, which means that after simulation of the excavation process of Gallery 08, about 6 months (from end of March 08 to the middle of October 08) of ventilation and associated desaturation of the whole system are simulated. Due to the capabilities of the adopted simplified approach without taking into account any damaging process, the development of an excavation damaged zone (EDZ) at the gallery contour is not simulated; the time-dependent desaturation process of the surrounding rock mass induced by ventilation is, however, modelled by setting the hydraulic boundary condition to a negative pore pressure of about -5 MPa. Consequently, the pore pressure field will vary with time.

On 13th October 2008 the excavation process of the MB niche is simulated stepwise (1.5 m per step) according to the time schedule shown in Fig. 4.2. The excavation process is finished on the 8th October 2008 after 273 days of simulation time. The shotcrete advance is not simulated in the model.

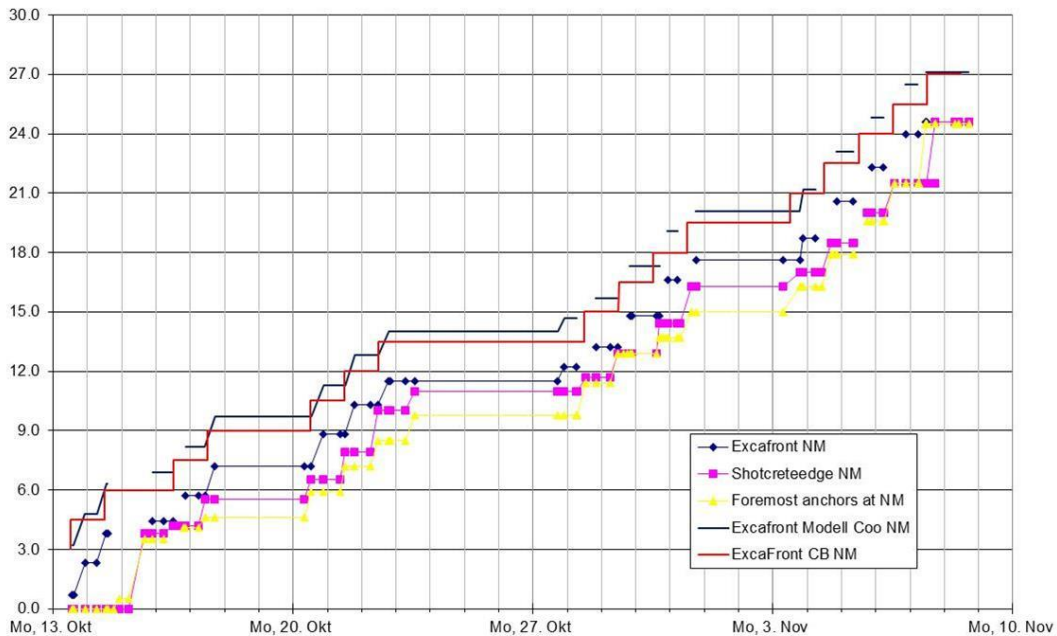


Fig. 4.2 Excavation process

4.2.2 Modelling results

Figure 4.3 shows the pore pressure propagation as a result of hydro-mechanical coupled numerical simulation when the excavation process is completed. The detailed view shows the symmetric distribution due to the inclined bedding planes and the resulting anisotropic hydraulic conductivity.

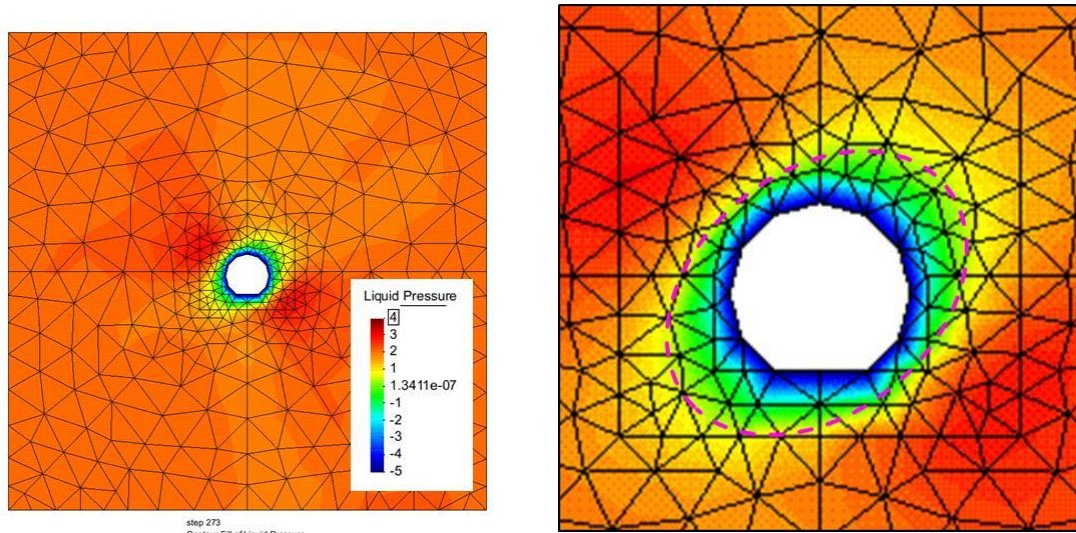


Fig. 4.3 Pore pressure propagation as a result of hydro-mechanical coupled numerical simulation after excavation (left: full model, right: detailed view)

4.2.3 Modelling calibration and interpretative calculations

Figure 4.4 shows selected measurement results of pore pressure evolution in BMB-15 sensor I4 and I5 versus simulation results. Both sensors show a significant increase in pore pressure when the excavation front reaches a distance of approx. 2 m. Their hydraulic time-dependent behaviour is strongly influenced by the excavation-induced stress redistributions: when the excavation process stopped for several days the pore pressure peak at sensor I4 dissipated to the level observed before the peak. After dissipation the pore pressure level is constant, although the distance of the sensor I4 and the excavation front is only 2 m. In case of sensor I5 where the excavation front had already passed the sensor location before the break a further decrease in pore pressure is measured. With respect to the results of the numerical simulation, this effect of time-dependent hydraulic behaviour is underestimated in the modelling. Similar hydraulic behaviour can be observed in Fig. 4.5 at sensor I1 and I2, when the excavation process stopped at the beginning of November.

The simplified hydro-mechanical coupled modelling approach used for numerical simulation of the MB experiment is not able to capture the change in pore pressure in its total value and the time-dependent behaviour derived from the in situ measurements results. Further modelling activities in the frame work of the EZ-G experiment will focus on these aspects.

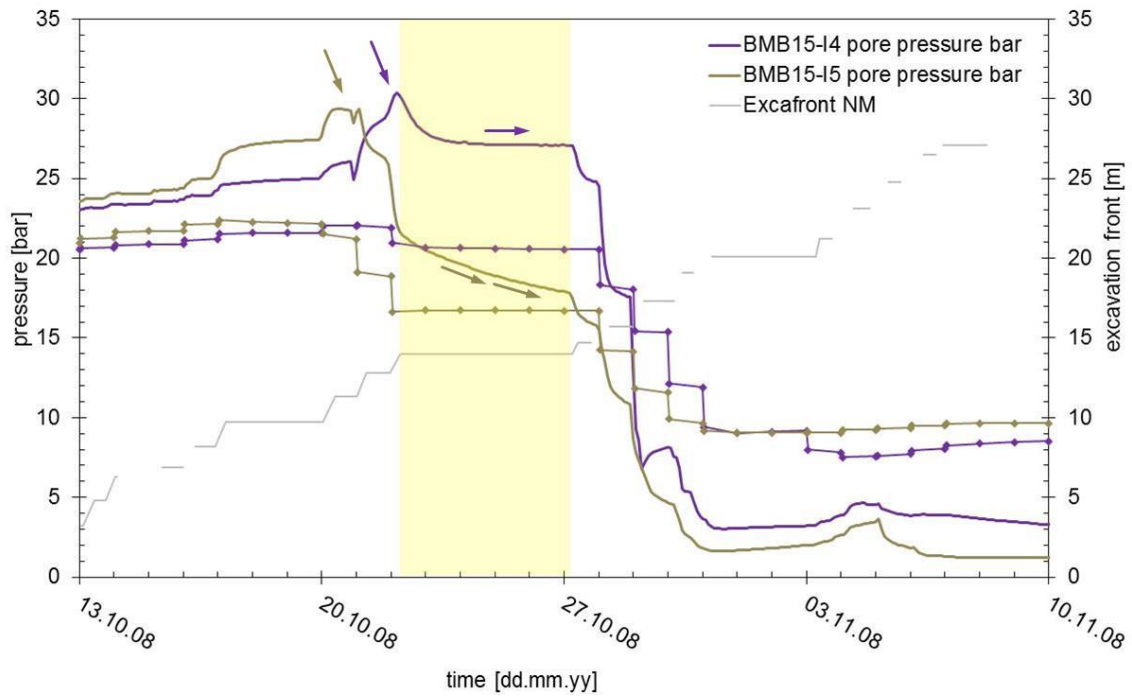


Fig. 4.4 Selected measurement results of pore pressure evolution in BMB-15 sensor I4 and I5 versus simulation results (dotted lines)

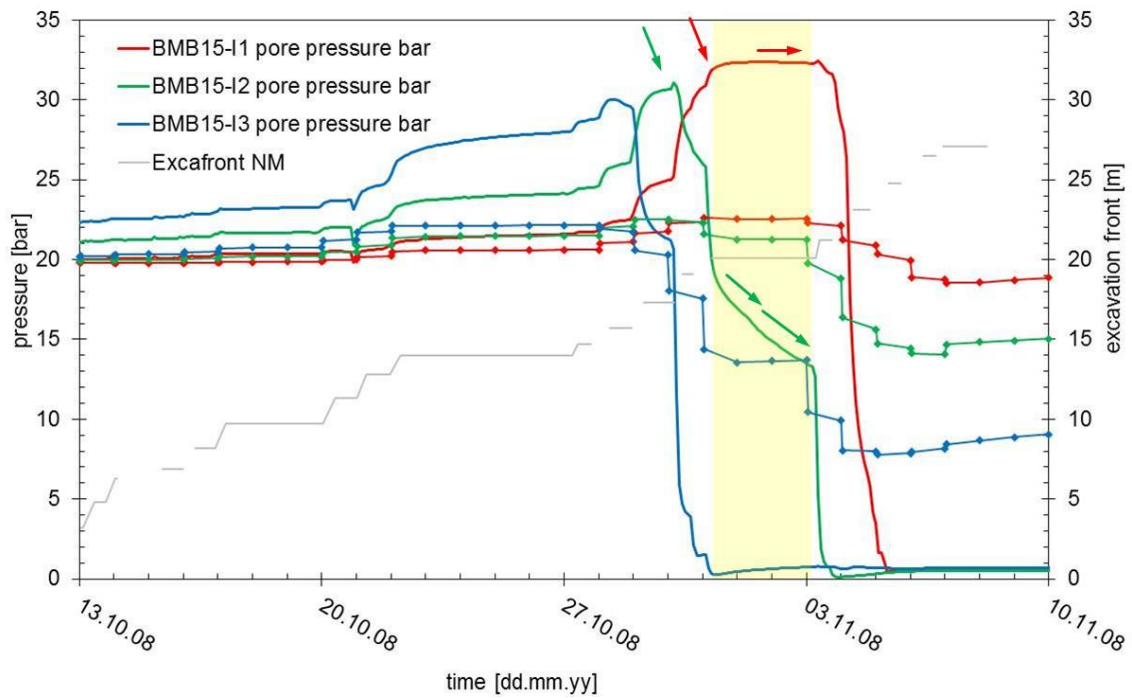


Fig. 4.5 Measurement results of pore pressure evolution in BMB-15 sensor I1 – I3 versus simulation results (dotted lines)

4.3 EZ-G experiment

Usually, initial values of pore pressure for model calculations are derived from in-situ measurements within the pre-excavation phase and used as input parameters for the interpretative calculation. The calculation effort that has been made within the EZ-G experiment shows the need for explicit modelling of the pore pressure sensors and the behaviour of the relevant rock mass prior to excavation. The following phases have to be separated and investigated step by step:

- Pre-excavation phase (2D and 3D-model)
- Gallery08 excavation process (3D-model)
- Post-excavation phase (2D-model)

This approach provides the basics for further success in interpretative modelling.

4.3.1 Numerical model

For interpretative modelling of the EZ-G experiment two different FE models were used. A 2-dimensional approach with explicit modelling of the different sensors to get information on the primary pore pressure field in the vicinity of the Gallery 04 and a 3-dimensional approach to capture the excavation induced stress redistributions and the related pore pressure evolution in advance to the Gallery 08 excavation front.

A 3-dimensional model with 50 m in height and in width and 25.5 m in length was used for the numerical simulation (Fig. 4.6, right). In the centre of the model the Gallery 08 is located. The Gallery 04 was abstracted and modelled as a part of the excavation drift of 3 m in length to keep the model geometry simple (Fig. 4.7 a). The dimensions of the 2D-model were chosen analogue to the 3D-model, but size and geometry of the pore pressure sensors BEZ-G6/7/8 were modelled explicitly (Fig. 4.6, left).

Prior to the EZ-G experiment, the excavation process of Gallery 04 (at least 3 m in length) and about 4 years (from June 04 to June 08) of ventilation and associated desaturation of the whole system were simulated. The excavation process of the Gallery 08 was enclosed and simulated stepwise Fig. 4.7, using 1.5 m per step (analogue to the approach used in the MB experiment, chapter 4.2).

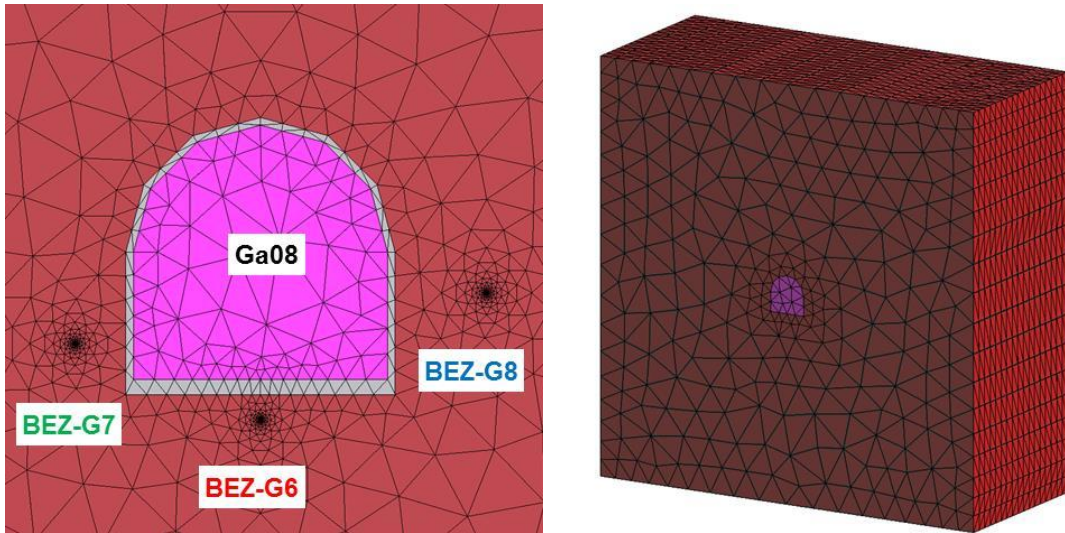
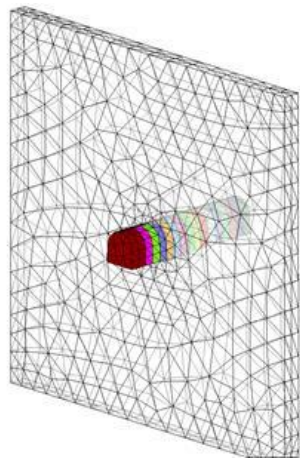
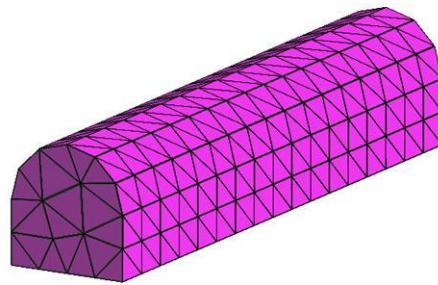


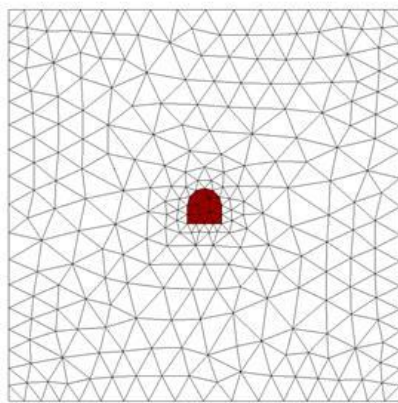
Fig. 4.6 FE models used for numerical simulation of the EZ-G experiment (left: 2D model, right: 3D model)



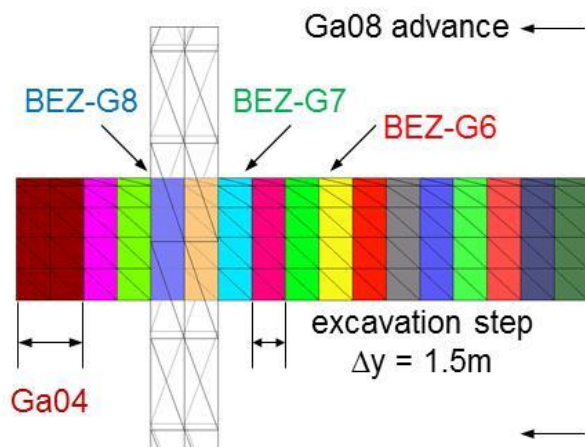
(a) part of Ga04 (idealized, 3 m)



(b) excavation drift (Ga08)



(c) front view



(d) side view

Fig. 4.7 Details of the 3D model, showing the gallery geometry and the individual excavation steps

4.3.2 Modelling results

Figure 4.8 shows measurement results of pore pressure evolution at BEZ-G6/7/8 versus simulation results of the 2-dimensional approach for the pre-excitation phase. The measurement results show that the pore pressure close to the Gallery 04 was reduced already before the Gallery 08 excavation front advances. Referring to the conclusions drawn from in-situ measurements in chapter 2.4 an initial pore pressure of 1.5 MPa was used in the model. Due to the capabilities of the adopted simplified approach, the time-dependent desaturation process of the surrounding rock mass induced by ventilation is modelled by setting the hydraulic boundary condition to a negative pore pressure of about -5 MPa. Consequently, the pore pressure field will vary with time.

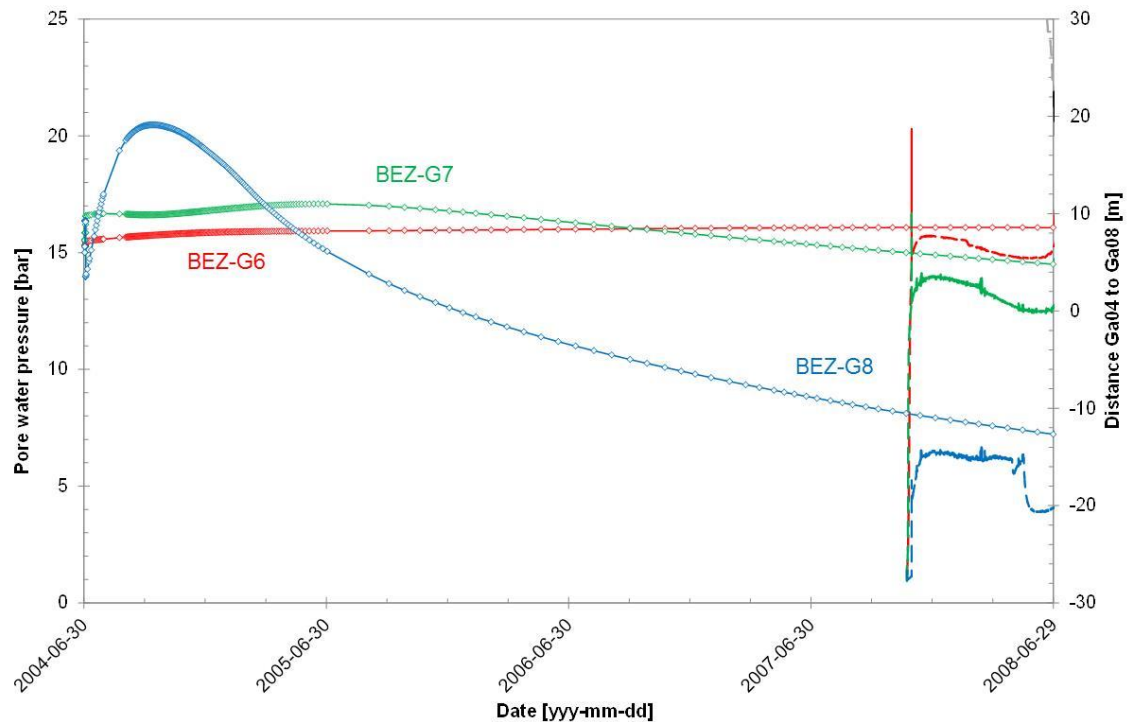


Fig. 4.8 Measurement results of pore pressure evolution at BEZ-G6/7/8 versus simulation results (dotted lines, 2D) – pre-excitation phase

The simulation results clearly show the deviating behaviour of BEZ-G8 after 4 years of possible drainage, when compared to the other sensors located further away from Gallery 04. Hence, the different levels of pore pressure at BEZ-G6/7/8 can be explained by the varying distance to the Gallery 04 face.

Following the above explained modelling strategy, the 3-dimensional simulation process starts with the excavation of Gallery 04 (Fig. 4.9 a). To capture the excavation in-

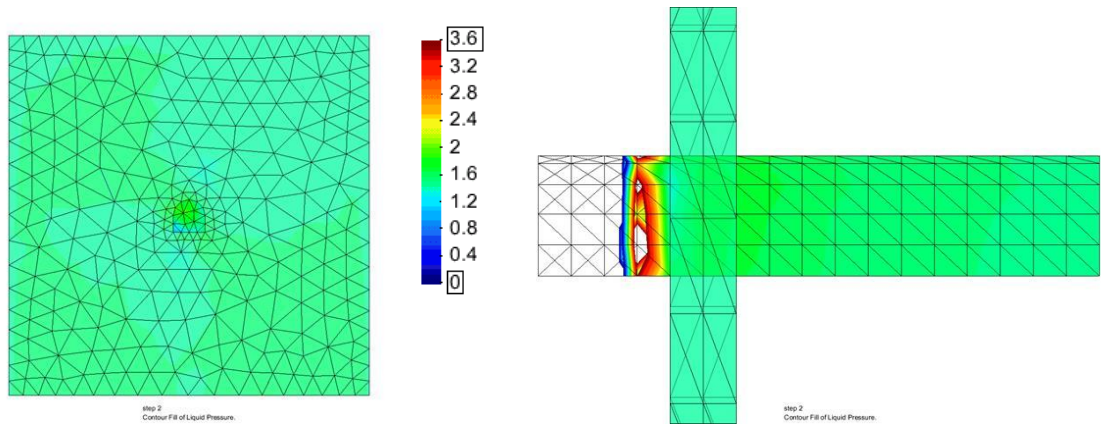
duced stress redistributions and the related pore pressure evolution and to make them visible, two different perspectives were used in Fig. 4.9 and Fig. 4.10: the front view in the plane of sensor BEZ-G8 at a distance of about 3 m to the Gallery 04 (left) and the side view of the excavation advance (right) are shown in terms of pore pressure propagation. The shown pore pressure values are limited to a range between atmospheric pressure and 3.6 MPa for clarity. Calculation values above or below this limit are not shown in the figures. The de-saturated zones with high pressures in suction are not coloured, consequently.

Figure 4.9a shows the pore water propagation due to the excavation process of the Gallery 04 at the beginning of July 2004. The excavation induced stress redistributions cause compressive deformation in the rock mass ahead of the excavation front. Following the simplified hydro-mechanical coupled modelling approach this deformation state leads to relatively high overpressures (twice the primary value, coloured in red), since rock mass damage is not considered. Within the next 4 years the pore pressure dissipates leading to desaturation in the vicinity of Gallery 04 (Fig. 4.9b, coloured in blue). This process even reaches the plane of the BEZ-G8 sensor.

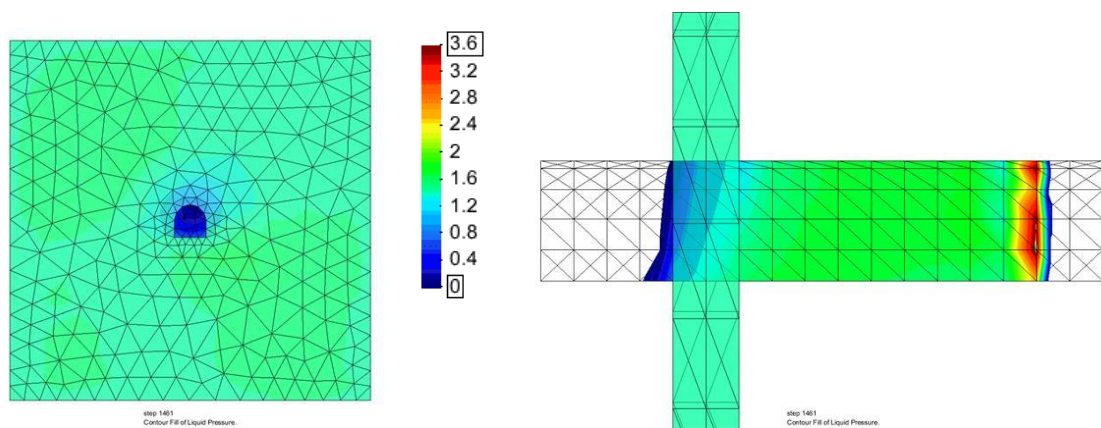
From the beginning of July 2008 the excavation process of Gallery 08 is simulated stepwise ($\Delta y = 1.5$ m) and the pore pressure propagation in the rock mass ahead of the excavation front follows the trend of previous excavation activities, without having any influence on the sensor at BEZ-G8 (Fig. 4.9c).

When the pillar between the Galleries reaches a distance of less than 9 m (twice the diameter) in the model, a minor influence of the excavation advance on the measurements at sensor BEZ-G8 becomes visible (Fig. 4.10a). The on-going excavation advance (Fig. 4.10b) leads to pore pressure increase high above the primary value of 1.5 MPa. Finally, the “break-through” is simulated at 26th August 2008 in the model and the calculation results show a constant de-saturated zone of about 1 m in depths circumferential around the gallery contour.

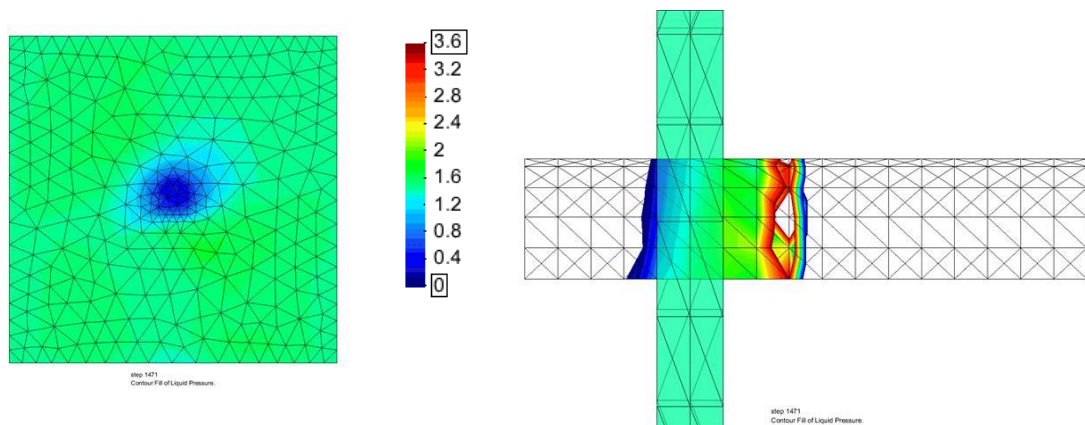
According to the anisotropic secondary stress field, in the vicinity of the side walls at more than 1 m depths, where the rock mass is already saturated, compressive deformation leads to pore pressure increase, whereas in the roof and the invert area pore pressure decrease takes place.



(a) Gallery 04 excavation process (2nd July 2004)

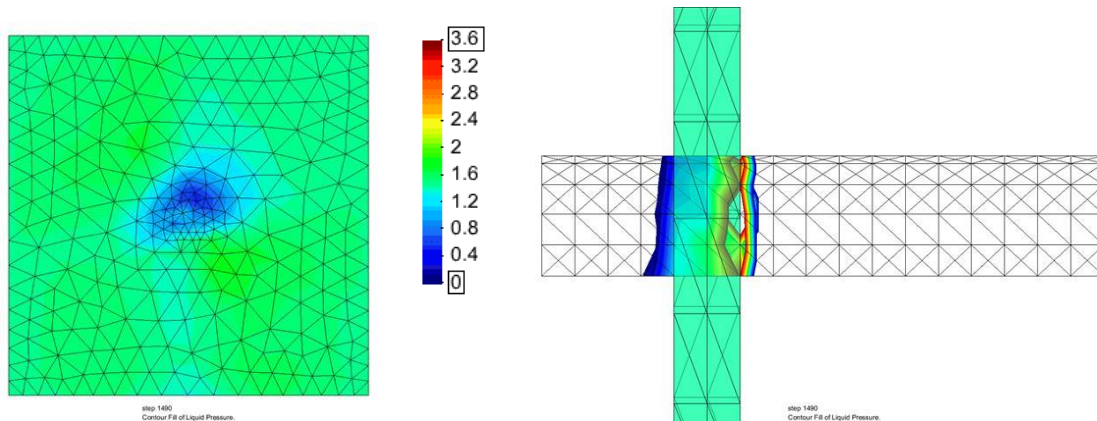


(b) Gallery 08 excavation process (1st July 2008)

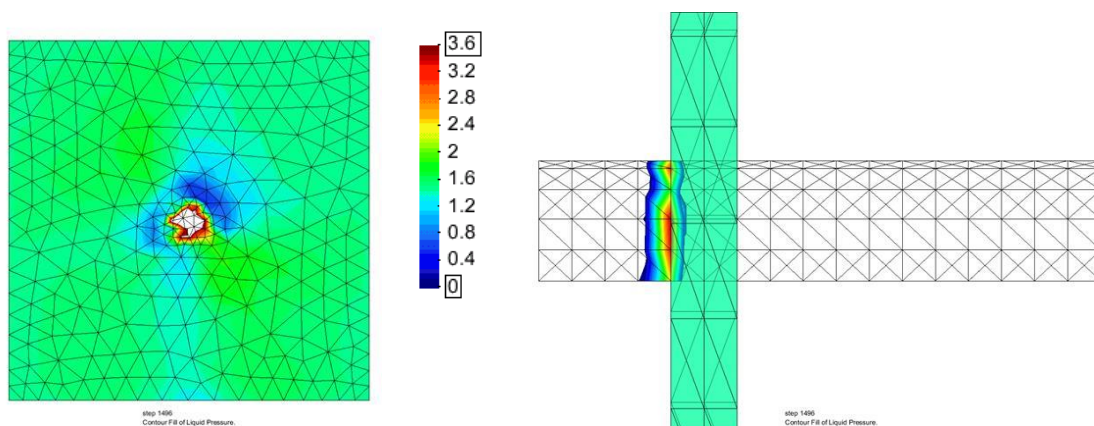


(c) Excavation advance at BEZ-G6 (11th July 2008)

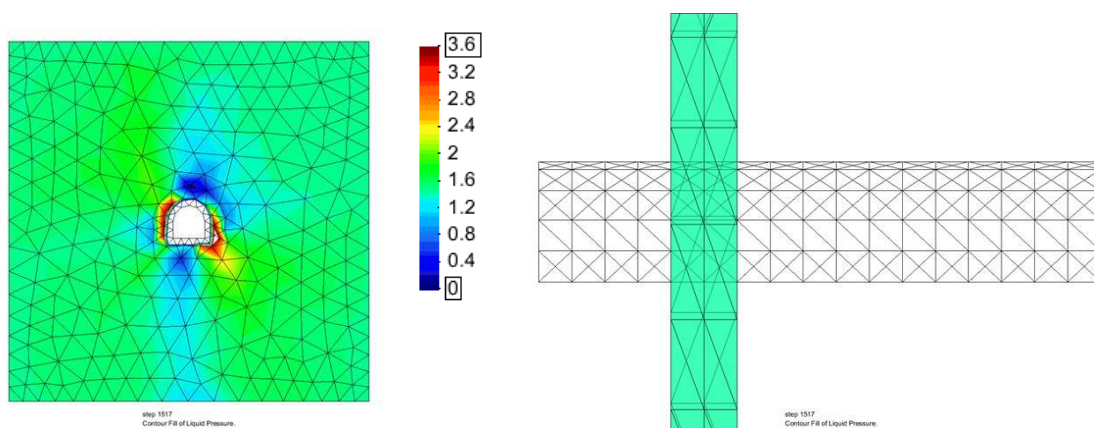
Fig. 4.9 Pore pressure propagation as a result of 3-dimensional hydro-mechanical coupled numerical simulation (2nd July 2004, 1st July 2008 and 11th July 2008)



(a) Excavation advance at BEZ-G7 (30th July 2008)



(b) Excavation advance before the break (5th August 2008)



(c) Final break through (26th August 2008)

Fig. 4.10 Pore pressure propagation as a result of 3-dimensional hydro-mechanical coupled numerical simulation (30th July 2008, 5th August 2008 and 26th August 2008)

4.3.3 Model calibration and interpretative calculations

Figure 4.11 and 4.12 show measurement results at sensors BEZ-G6/7/8 versus simulation results of the 3-dimensional approach for the Gallery 08 excavation phase in terms of pore pressure evolution. In addition, the advance of the excavation front is shown on the secondary ordinate in terms of distance from Gallery 04 to Gallery 08.

Referring to chapter 2.4 the measurement results show that during excavation a pressure concentration zone as elastic reaction evolves in front of the excavation face. Close to the excavation face, pore pressure is reduced as a consequence of unloading and potential damage. The calculation results follow the general trend of the measurements concerning pore pressure increase and decrease depending on the distance to the excavation advance, although the effect of time-dependent hydraulic pressure response is overestimated in the modelling.

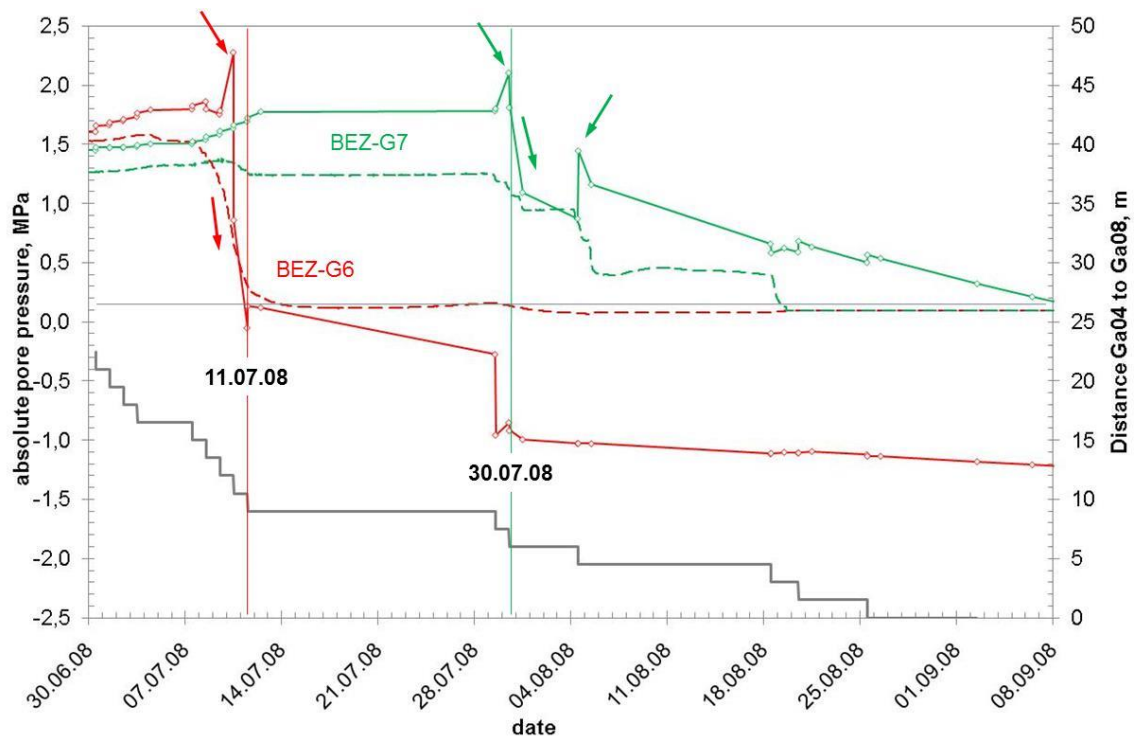


Fig. 4.11 Measurement results of pore pressure evolution in BEZ-G6 & 7 versus simulation results (dotted lines, 3D) – Ga08 excavation phase

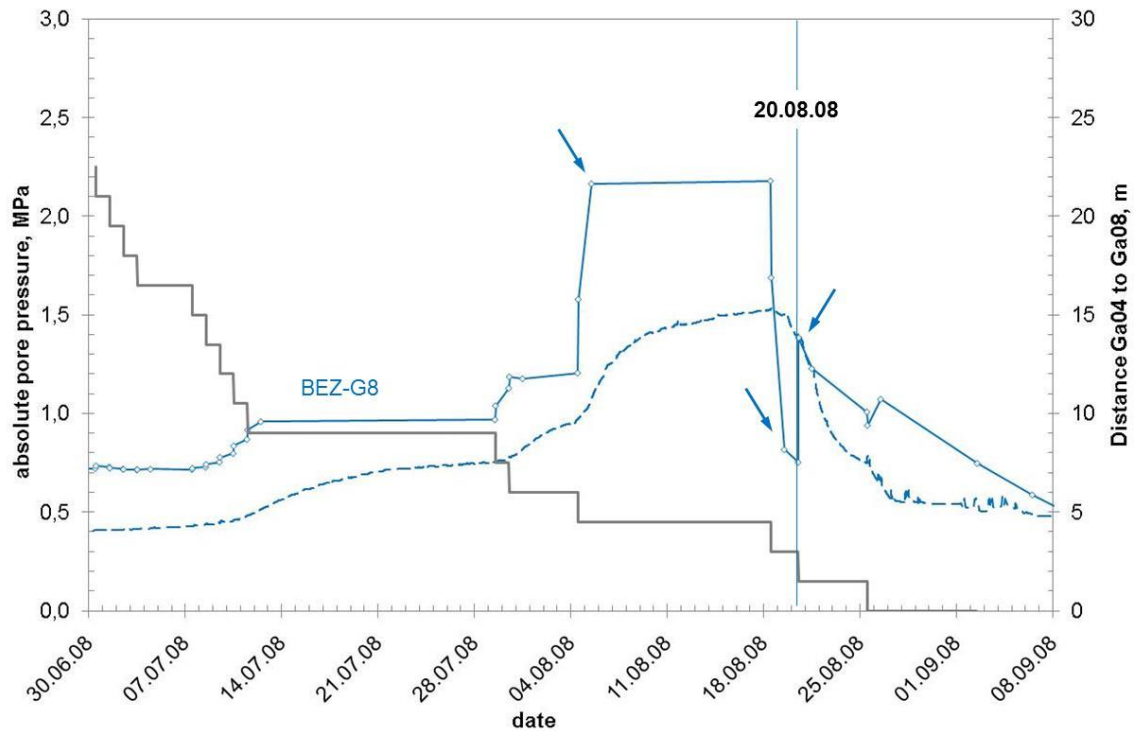


Fig. 4.12 Measurement results of pore pressure evolution in BEZ-G8 versus simulation results (dotted lines, 3D) – Ga08 excavation phase

Both, the MB experiment as well as the EZ-G experiment have been performed within the framework of the extension of the Mont Terry Rock Laboratory. The experimental work was intended to collect data about stress redistributions and related pore pressure evolution in the vicinity of the excavation advance and investigate the hydro-mechanical coupled material behaviour during the excavation process of the new Gallery in 2008. The simplified hydro-mechanical coupled modelling approach used for numerical simulation of the EZ-G experiment is able to capture the change in pore pressure in general, but probably not in its total value.

While the data obtained in these experiments are valuable for characterising the response of the rock mass to short-term stress redistributions, they are of limited suitability with respect to the investigation of long-term time-dependent behaviour. Therefore, further modelling activities in the framework of the DM-A experiment focus on this aspect.

4.4 DM-A experiment

4.4.1 Numerical model

A 2-dimensional plane strain model with 106 m in height and in width was used for the numerical simulation (Fig. 4.13). In the centre of the model the Gallery 04 is located. The dilatometer probe was abstracted and modelled as a cylindrical borehole of 11 cm in diameter without explicit modelling of the instrumentation to keep the calculation effort low. The dilatometer probe is located at about 17 m distance to Gallery 04.

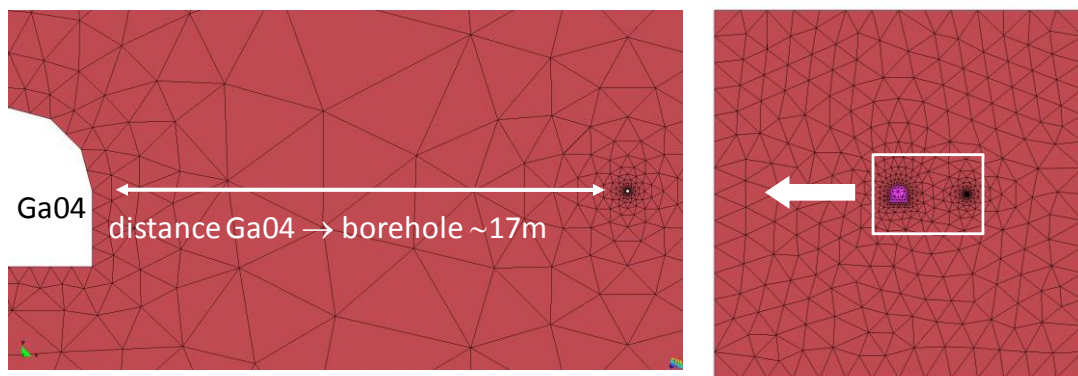


Fig. 4.13 FE model (2D) used for numerical simulation of long-term borehole deformation (right: full model, left: detail)

The simulation process goes along with the realistic time schedule as far as possible, which means that after simulation of the excavation process of Gallery 04, about 5 years (from end of June 04 to beginning of May 09) of ventilation and associated desaturation of the whole system are simulated. Due to the capabilities of the adopted simplified approach without taking into account any damaging process the development of an excavation damaged zone (EDZ) at the gallery contour is not simulated; the time-dependent desaturation process of the surrounding rock mass induced by ventilation is, however, modelled by setting the hydraulic boundary condition to a negative pore pressure of about -5 MPa. Consequently, the pore pressure field will vary with time.

Since Gallery 04 was only modelled to provide the hydraulic boundary condition and deformation measurements have only been performed in the dilatometer borehole 17 m away, neglecting damage around the gallery is no constraint for the simulation.

4.4.2 Modelling results

On May 5th, 2009 the borehole was excavated and prepared for probe installation. Figure 4.14 shows the negative pore pressure propagation as a result of hydro-mechanical coupled simulation for the sensor reference measurements on June 23rd, 2009 (left) and for the end of March 2010 (right).

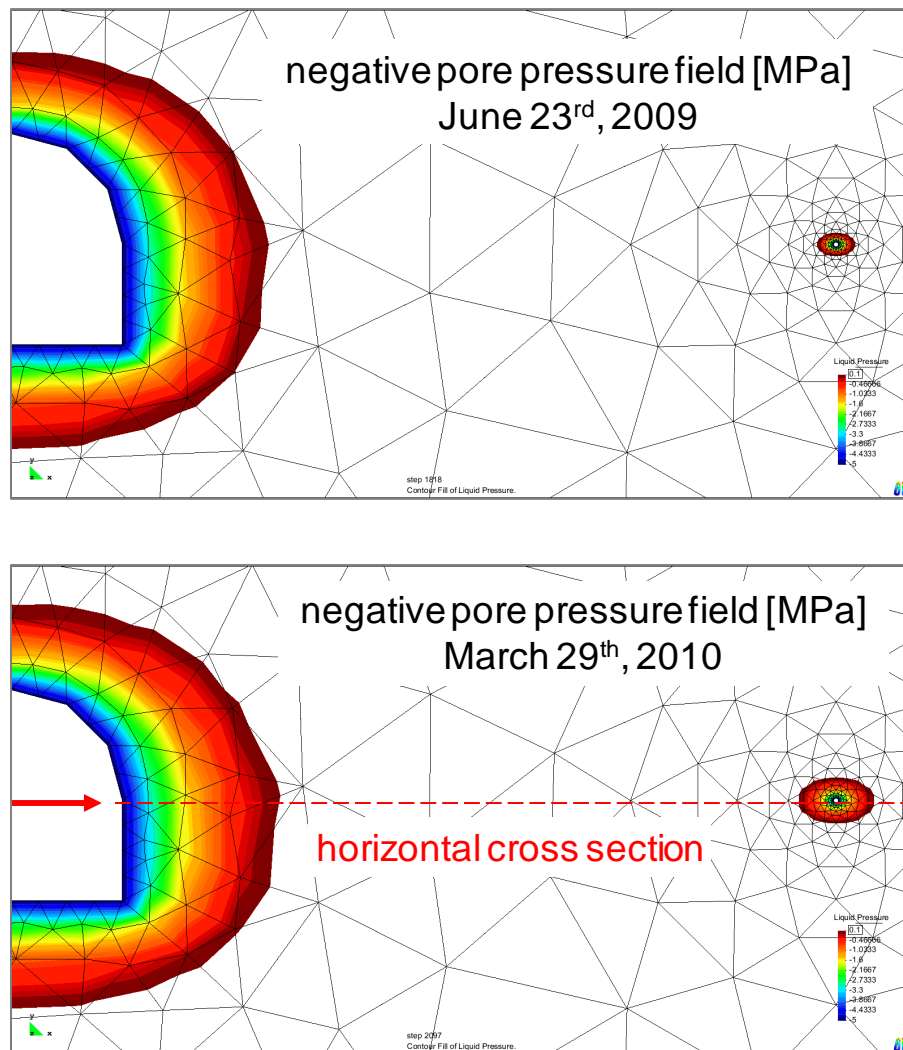


Fig. 4.14 Negative pore pressure propagation as a result of hydro-mechanical coupled numerical simulation for the sensor reference measurements on June 23rd, 2009 (above) and for the end of March 2010 (below)

In addition, Fig. 4.15 gives an impression of the calculated pore pressure values in a horizontal cross section, showing the total pressure values in small scale and the resulting deviation values with respect to sensor reference measurement (June 23rd, 2009) in large scale. The figure shows that the pore pressure redistribution process around the dilatometer probe is still active due to the hydraulic boundary condition of

negative pore pressure of about -5 MPa whereas the changes around the gallery are less pronounced.

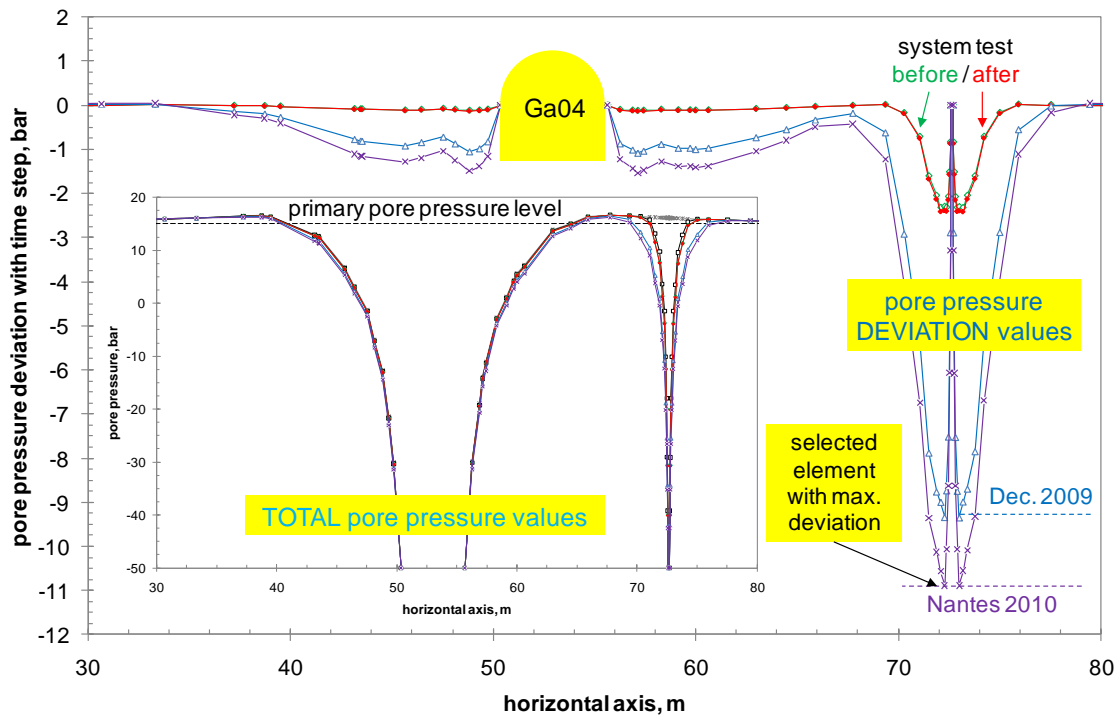


Fig. 4.15 Calculation results in a horizontal cross section – total pore pressure values (small scale) and the resulting pore pressure deviation values with respect to sensor reference measurement

To identify potential driving mechanisms for hydro-mechanical coupled time-dependent deformation in the argillaceous rock a single element, the one showing the highest deviation, is taken for further evaluation of stress and pore pressure.

In fact the highest values are expected to develop at the contour zone along with the borehole excavation process. Due to the time passed until the reference measurement is conducted, the main part of the pore pressure redistribution near the borehole contour has already happened and the zones showing pore pressure decrease have enlarged with time. Therefore the selected element is at a distance of about 30 cm to the borehole contour.

For this selected element the calculation results on time-dependent principal stress and pore pressure deviation with respect to borehole excavation and sensor installation sequence are shown in Fig. 4.16. As a reference value for mechanical loading the figure

shows the deviatoric *VON MISES* stress as a function of the second invariant calculated due to equation 4.23:

$$\sigma_{VM} = \sqrt{3 \cdot I_2^D} = \sqrt{\frac{1}{2} \cdot \sqrt{(\sigma_1 - \sigma_2)^2 + (\sigma_2 - \sigma_3)^2 + (\sigma_3 - \sigma_1)^2}} \quad (4.23)$$

During the time before the reference measurement the deviatoric *VON MISES* stress shows an increase due to the excavation process of the borehole and the induced stress redistribution. The excavation induced change of the hydraulic boundary condition at the contour zone provides the possibility of a desaturation of the adjacent rock mass. Due to the fact that the main part of the pore pressure redistribution near the borehole contour occurs in short time the principal stress variables show a change in their absolute values as well.

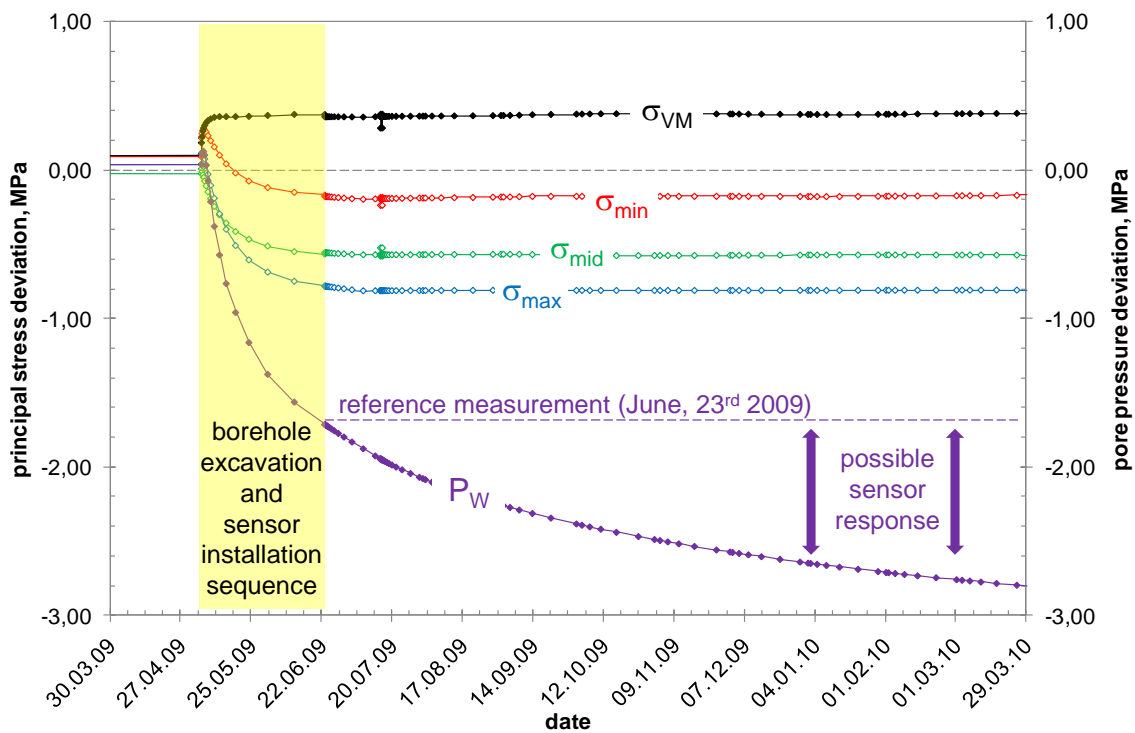


Fig. 4.16 Calculation results of the selected element on time-dependent principal stress and pore pressure deviation during and after borehole excavation and sensor installation

At the time of the reference measurement the stress redistribution process in the regarded area is nearly finished, meaning that a change in deviatoric stress is no longer visible. Besides, the desaturation process in the selected element is still active, associated with the pore pressure change with time.

Regarding the calculated borehole contour deformation with time shown in Fig. 4.17 an ovalization process develops as expected due to the anisotropic primary stress approach and the corresponding secondary stress field after borehole excavation. To make the calculated results visible within the selected scale with respect to the initial borehole diameter of 110 mm, the deformation values have been re-sized with a multiplier of 1/150 mm.

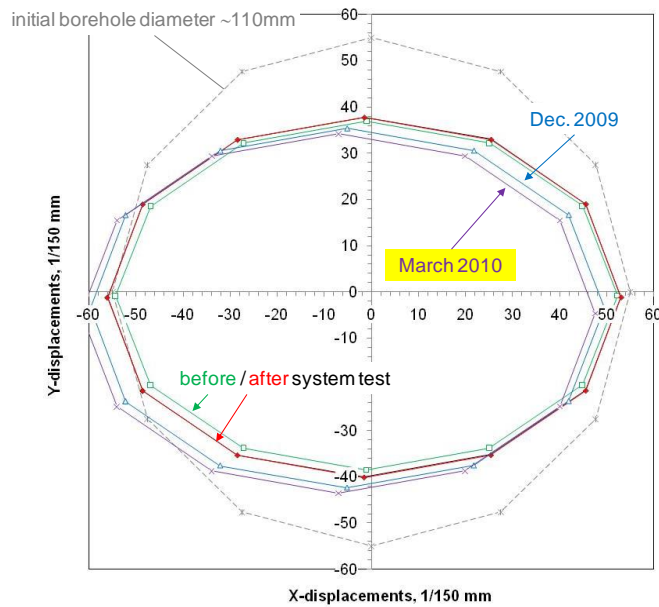


Fig. 4.17 Calculation results on time-dependent borehole contour deformation due to pore pressure redistribution

With regard to the calculation results mentioned above it is quite obvious that time-dependent deformation processes of the borehole contour which have been observed could partially be caused by pore pressure redistribution.

In the next step the hydro-mechanical coupled calculation results using the simplified constitutive model are compared to the observed long-term borehole measurement results

4.4.3 Model calibration and interpretative calculations

Obviously the geomechanical physical approach is of main importance for predictive modelling of argillaceous rocks, especially when large time scales are considered (post closure phase of a repository), /CZA 09/. For rock salt formations a marginal and negli-

gible creep limit is assumed, which means that any kind of deviatoric stress leads to creep deformation. For argillaceous rock formations that exhibit an anisotropic primary stress state the question about the presence of a creep limit and its absolute value is still open. On one hand viscous deformation processes could start when a deviatoric stress state is imposed that is different to the primary anisotropic one. On the other hand it is obvious that fluid flow processes are related to redistribution of pore pressures induced by volumetric deformation due to mechanical loading.

Fig. 4.18 shows the hydro-mechanical coupled calculation results with the simplified constitutive model as discussed above in comparison to the observed long-term borehole measurement results of the dilatometer probe located at Niche DR at the Mont Terri URL. The results are interpreted in terms of deformation rates that are determined about once a month.

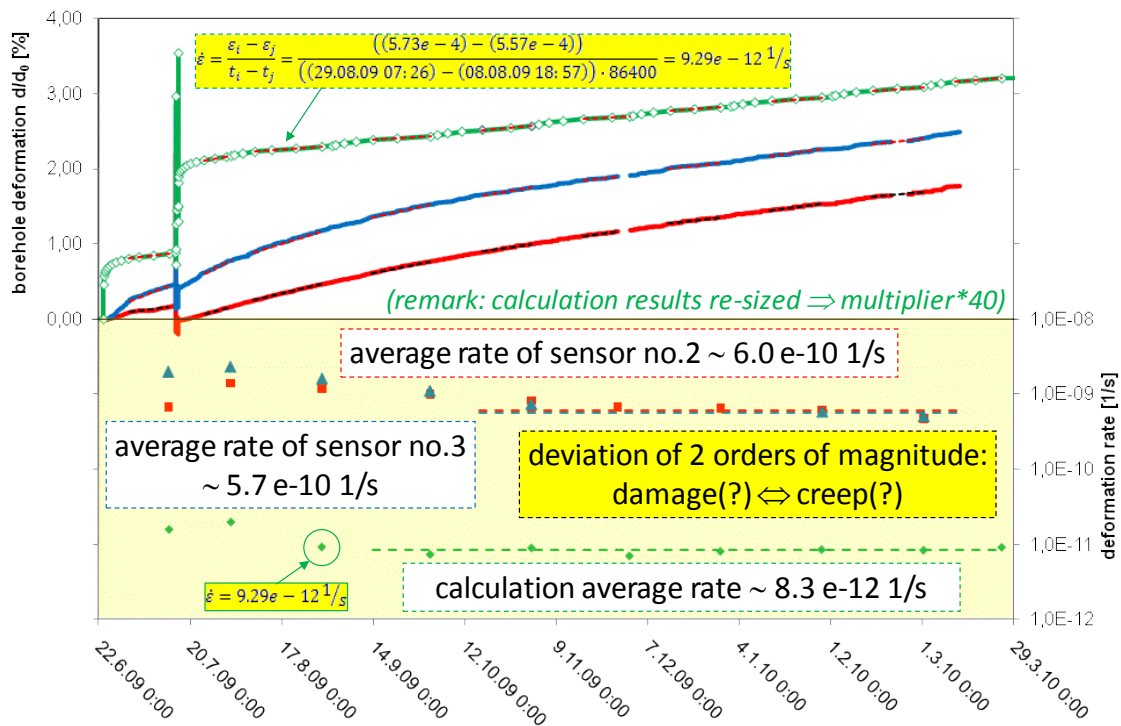


Fig. 4.18 Average borehole deformation rates – experimental findings vs. calculation results

As an example, equation 4.24 shows the mathematic formulation to determine a deformation rate $\dot{\epsilon}$ for August 2009 on the basis of the achieved effective borehole deformations ($\epsilon_i = d_i/d_0$):

$$\dot{\varepsilon} = \frac{\varepsilon_i - \varepsilon_j}{t_i - t_j} = \frac{((5.73e-4) - (5.57e-4))}{((29.08.09\ 07:26) - (08.08.09\ 18:57)) \cdot 86400} = 9.29e - 12\ 1/s \quad (4.24)$$

The monthly derived deformation rates as well as a calculated linear average value for the simulation results are shown in figure 4.18 and compared to the values determined on the basis of the measurement results.

As indicated in Fig. 4.18, the average values for the hydro-mechanical coupled simulation results ($\dot{\varepsilon}_{cal} = 8.3e - 12\ 1/s$) and for the measurement data of the dilatometer probe ($\dot{\varepsilon}_{in\ situ} = 6.0e - 10\ 1/s$) show a deviation by two orders of magnitude. This difference could either be interpreted by time-dependent damage processes or by assuming that viscous creep deformation processes take place. In fact it could even be a combination of both concepts.

As a result, it can be stated that pore pressure change is not sufficient to explain the time-dependent deformation of the rock around the borehole, in fact, it plays a rather insignificant role in this configuration /CZA 13/. This may be different with other geometries (e. g., open galleries), but for the sealed dilatometer probe borehole pore pressure redistribution is not the major driving force of deformation. With regard to modelling, additional calculations including viscous deformation and possibly damage are needed. This will require additional work in the field of development of constitutive laws and parameter identification.

4.5 TED experiment

To study the thermo-hydro-mechanical effects of the early thermal phase on the clay host rock, ANDRA has performed an in-situ heating test (see chapter 3). The TED experiment was designed to estimate the overpressure generated by the heat load imposed by several heaters and to study the evolution of the damaged zone due to heating.

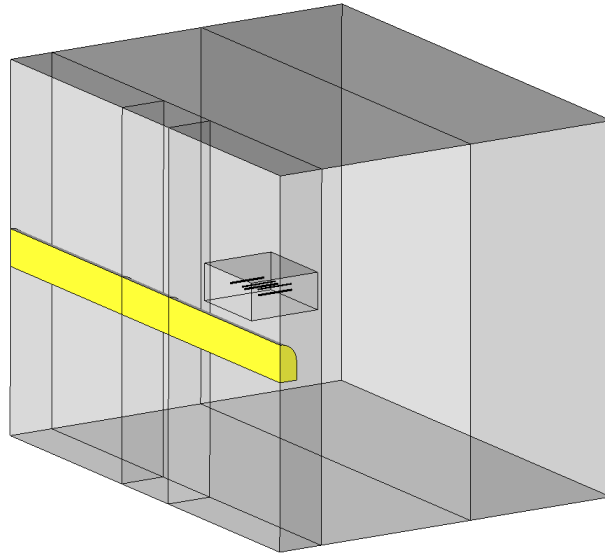
4.5.1 Numerical model

For interpretative modelling of the TED experiment a 3-dimensional approach was used with explicit modelling of 5 selected boreholes, the boreholes TED1201/02/03 that were used to install the heater elements and the 2 ones TED1230/31, that were used for extensometer measurements and therefore lead to permanent desaturation of the rock since installation.

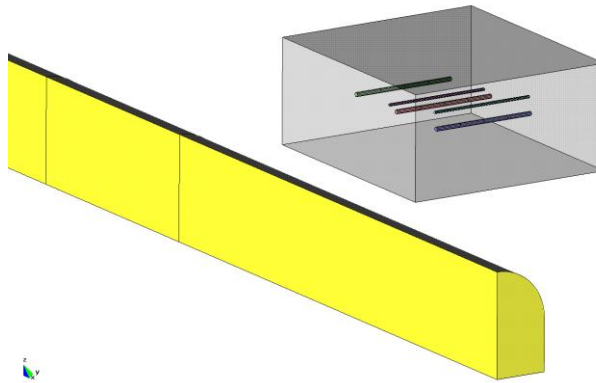
A 3-dimensional model with 40 m in height and in width and 52 m in length was used for the numerical simulation, Fig. 4.19. In the centre of the model the explicitly modelled boreholes are located. To get information on the primary pore pressure field in the vicinity of the GED Gallery half of the drift was modelled and the excavation induced drainage process was simulated via constant capillary pressure of -5 MPa at the gallery wall.

Prior to the TED experiment, the excavation process of the GED Gallery and about 10 months (from September 08 to July 09) of ventilation and associated desaturation of the whole system were simulated. The excavation process of the boreholes was enclosed and simulated stepwise. The boreholes used for extensometer measurements TED1230/31 were drilled at 20th July and atmospheric pressure was set at the borehole wall. In Oktober, the heater boreholes TED1203/02/01 were drilled at 5th, 8th and 12th day of the month and kept constant at atmospheric pressure.

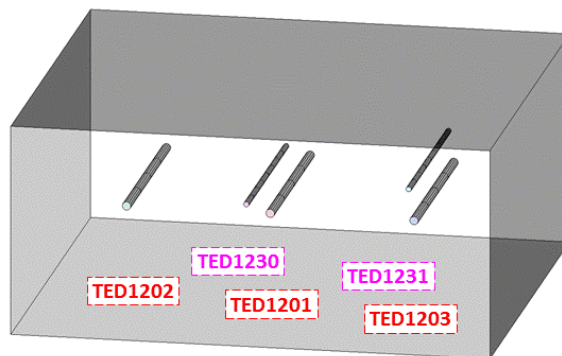
Then from January 25th, 2010 the heating procedure started with the stepwise increase of heating power (150/300/600 W) of the heater element in borehole TED1201, see chapter 3. A similar procedure was started from March 1st, 2010 for the boreholes TED1202 and TED1203. Finally, after 999 days of heating the heat input was reduced stepwise (50 W per step) in all 3 boreholes.



(a) 3-dimensional model



(b) GED gallery



(c) boreholes, used for heating and extensometer measurements

Fig. 4.19 FE model used for numerical simulation of the TED experiment (3D model)

4.5.2 Modelling results

The following figures show selected calculation results versus measurement data (see chapter 3.4) for the temporal evolution at the different heating boreholes TED1201 (Fig. 4.21a), TED1202 (Fig. 4.21b) and TED1203 (Fig. 4.21c). The temperature measurements in the TED1202 do not represent the real temperature around the borehole, since the sensors failed during the second thermal load step. The measurements show, with respect to the sensor location (Fig. 4.20) a deviation of 20 °C within the third heating phase and a maximum value of 120 °C at TED1201. The variation in the TED1201 and TED1203 are due to the insufficient contact between the sensors and the casing. This effect cannot be taken into account in the simulation.

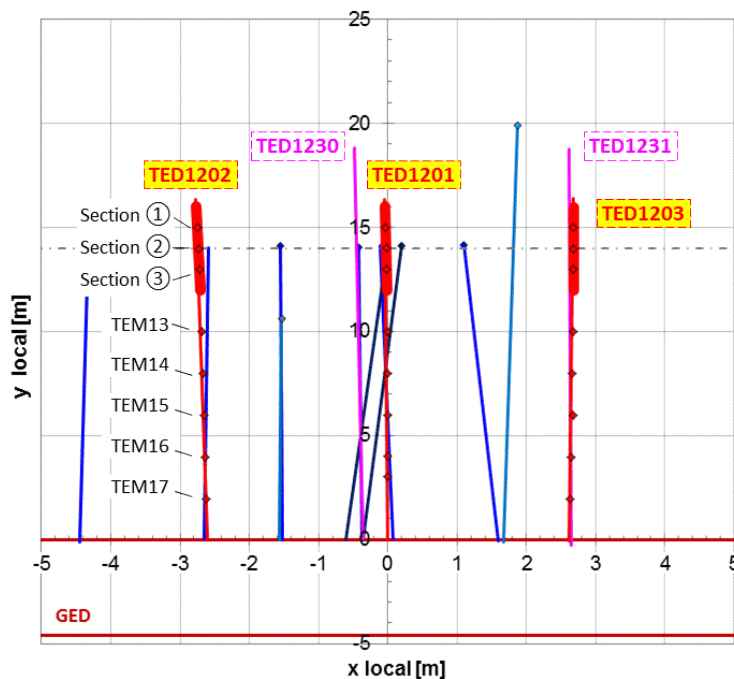
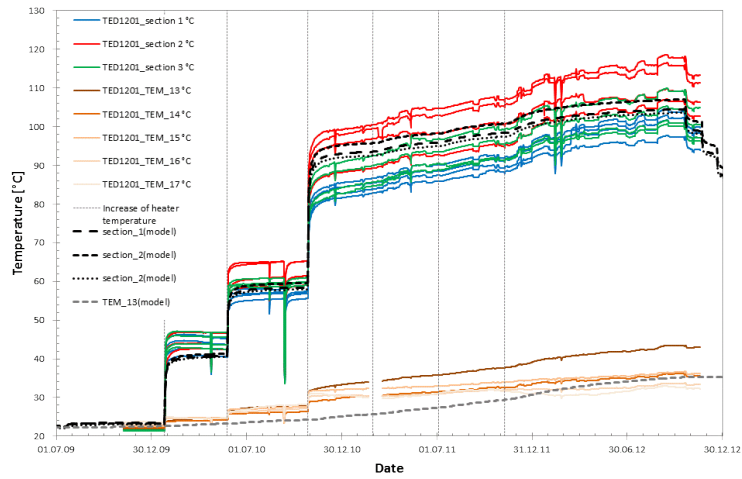
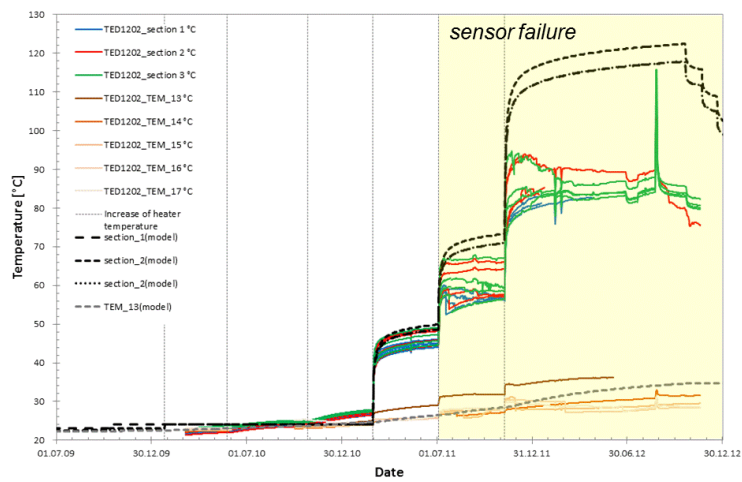


Fig. 4.20 Sensor location at the heating boreholes of the TED experiment (top view)

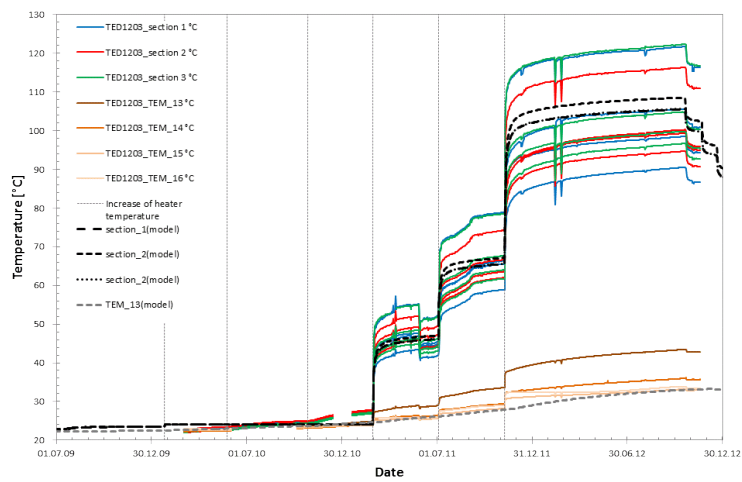
In the reality the thermal load is applied by constant power. For simulation purposes the load was applied using a temperature boundary condition. Therefore, a maximum value of 110 °C is reached in the calculation for TED1201, which covers the trend of the measurements. As a consequence of the sensor failure, the temperature measurement at TED1202 is overestimated in the modelling, Fig. 4.21b. For the third heater in borehole TED1203 a median trend of the temperature evolution is reached by the modelling exercise. It is difficult to reproduce the reality with temperature loading. In TED experiment the temperatures in the heater boreholes are the results of the power applied (which is constant) and depend a lot of the surrounding environment.



(a) TED1201



(b) TED1202 (with sensor failure at second thermal load level)



(c) TED1203

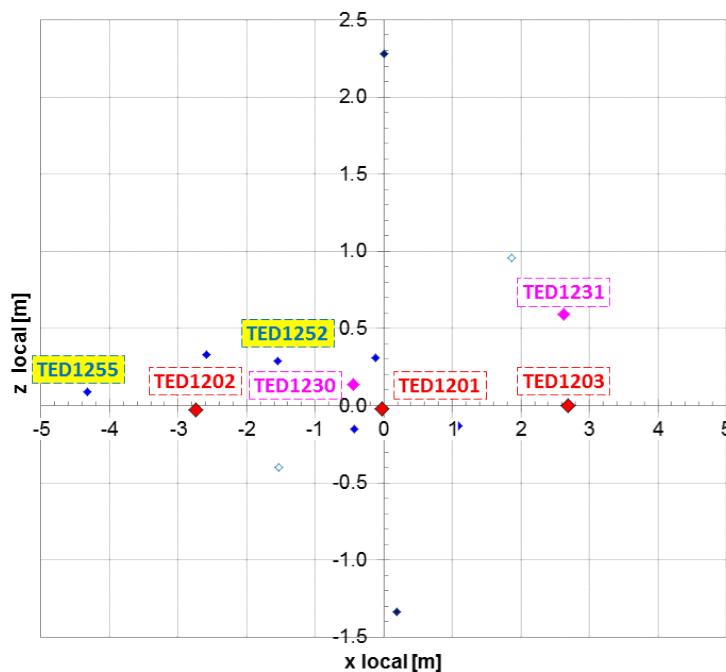
Fig. 4.21 Selected measurement results of temperature evolution versus simulation results (dotted lines)

4.5.3 Model calibration and interpretative calculations

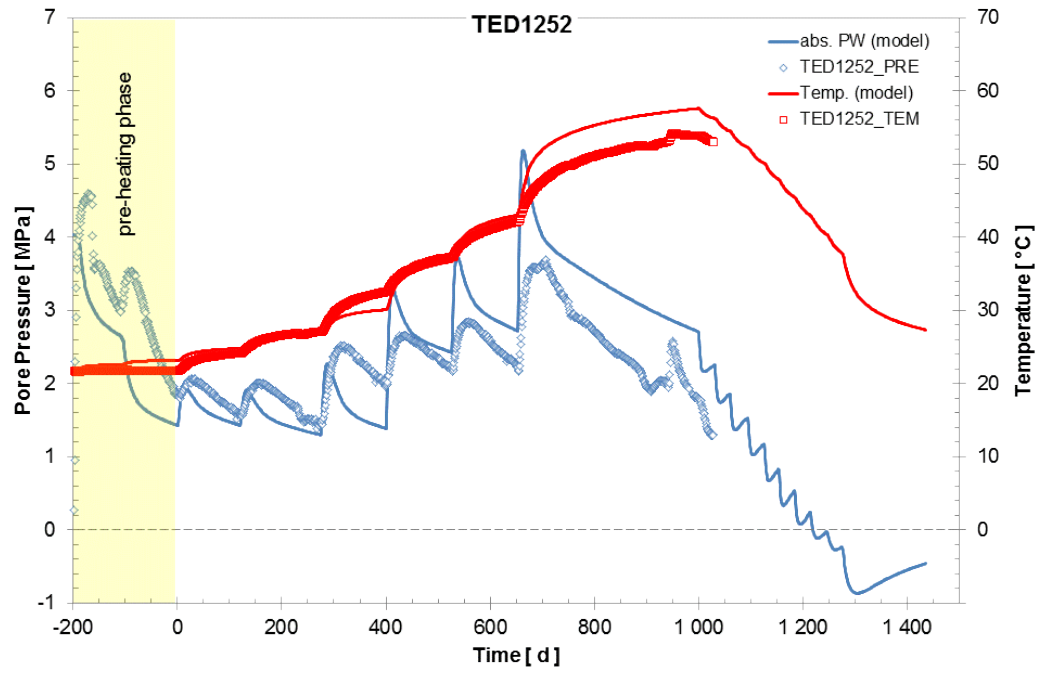
The TED experiment was designed to estimate the overpressure generated by the thermal load imposed by several heaters. To study the thermo-hydro-mechanical effects of the early thermal phase on the clay host rock selected measurement results at borehole sensors TED125x are shown in the following and compared to calculation results. These sensors record the absolute pore pressure together with the temperature evolution. In the calculation, the sensors were not explicitly modelled to keep the calculation effort manageable. Hence, the calculation values are taken from the respective position inside the mesh.

Temperature and absolute pore pressure evolution with time

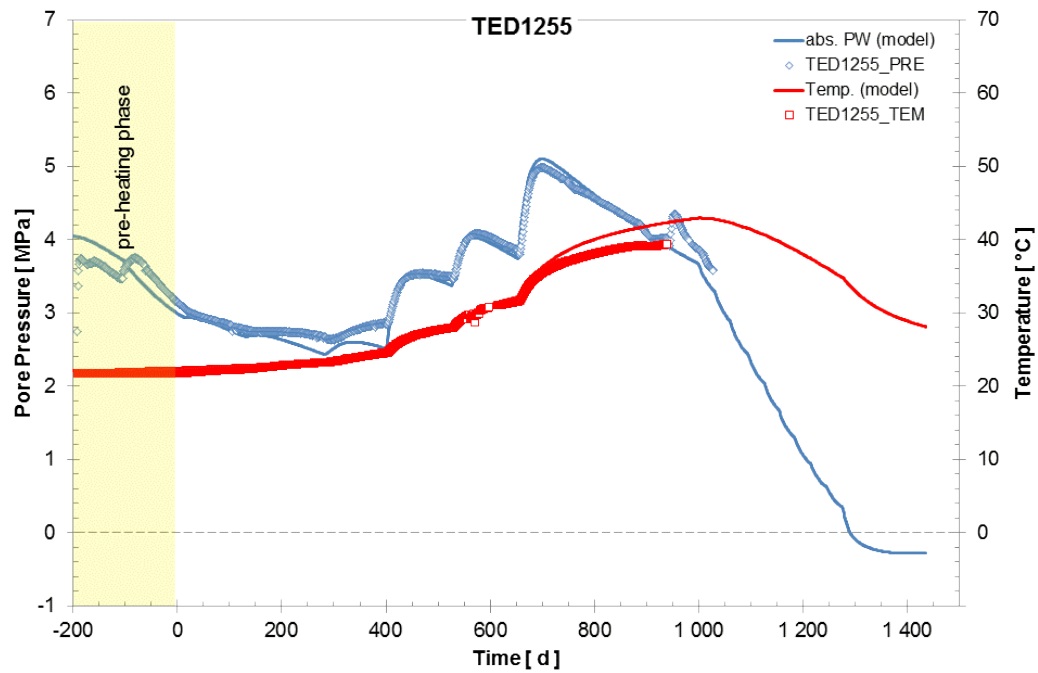
Fig 4.22 gives an impression of the evolution of the temperature and the absolute pore pressure with time at the sensors at borehole TED1252 and TED1255. While, the calculation results for the temperature evolution follow the general trend of the measurements for the first 700 days, the temperature increase in the last load sequence ($t > 700$ d) is overestimated in both sensors. For borehole TED1255, which lies outside the central part between the heater boreholes TED1202 and TED1203 the calculation results for the absolute pore pressure evolution perfectly match the measured results, while the pore pressure increase following the thermal load sequence is overestimated in borehole TED1252.



(a) sensor location



(b) TED1252



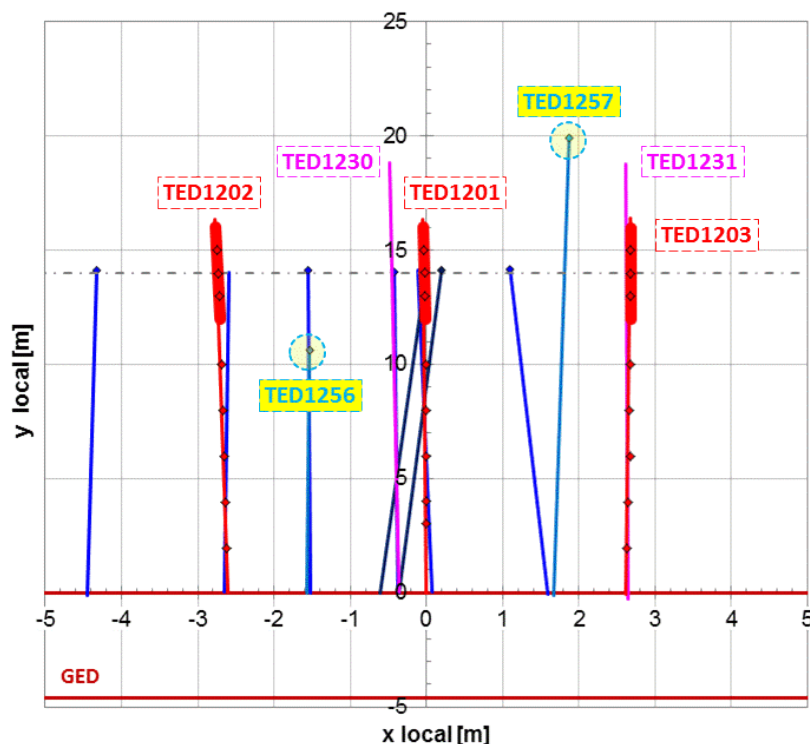
(c) TED1255

Fig. 4.22 Measurement results of absolute pore pressure and temperature evolution at sensor TED1252 and TED1255 versus calculation results

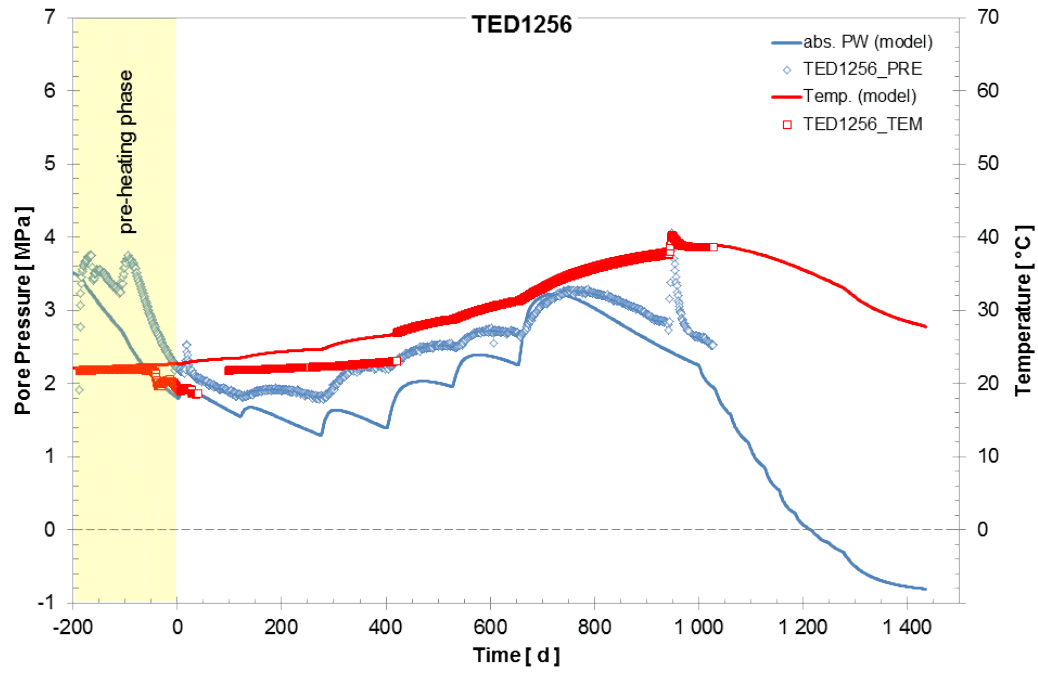
Gallery GED drainage effect

To get information on the primary pore pressure field in the vicinity of the GED Gallery half of the drift was modelled and the excavation induced drainage process was simulated via constant capillary pressure of -5 MPa at the gallery wall. To capture the influence of the GED gallery on the absolute pore pressure evolution near the heater 2 sensors were located at 10 m (TED1256) and at 20 m (TED1257) distance to the gallery contour. The distance has a visible effect on the pore pressure niveau shown in Fig. 4.23.

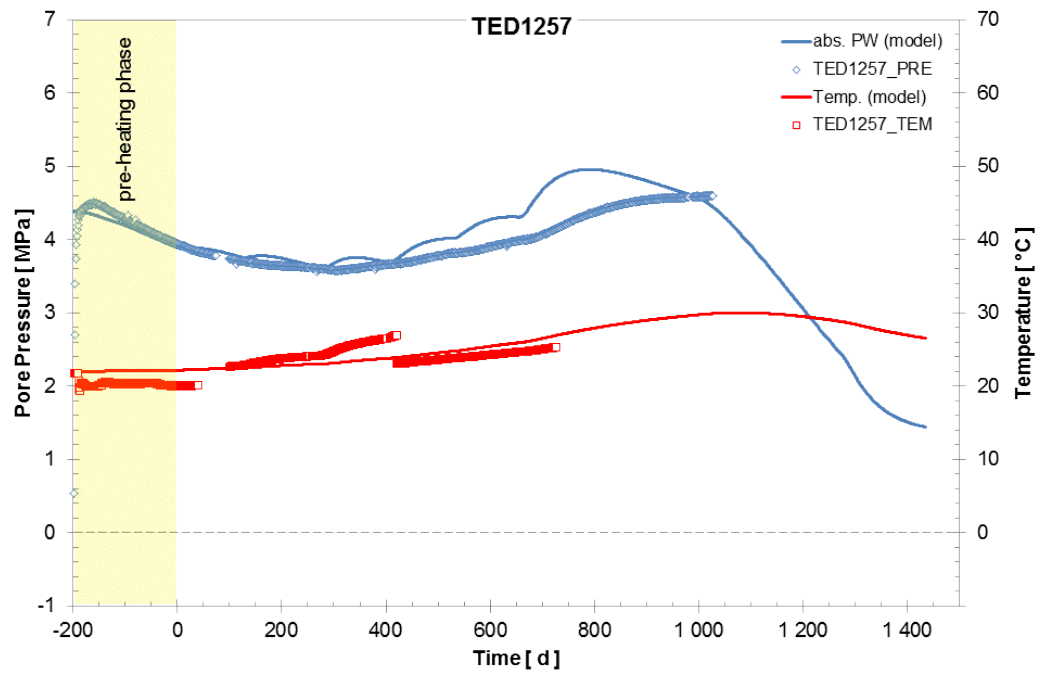
After the pre-heating phase of about 200 days, both, the measured data as well as the calculated results for absolute pore pressure in borehole TED1256 show values of 2 – 3 MPa (half the primary value). Whereas, the decrease in absolute pore pressure at borehole TED1257 is even less (pore pressure level of about 4 MPa). Following the heating sequence, the deviation of the calculation results and the measurement results is in an acceptable range.



(a) sensor location



(b) TED1256



(c) TED1257

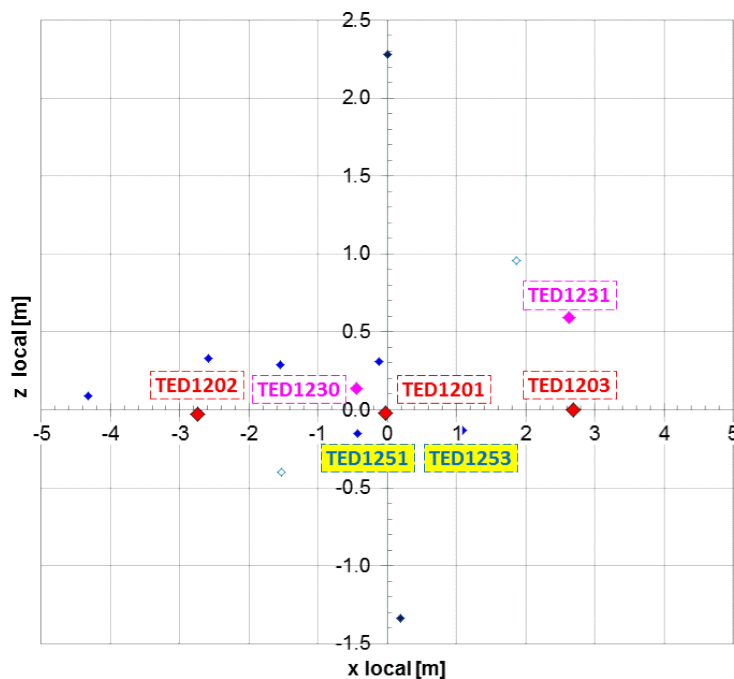
Fig. 4.23 Measurement results of absolute pore pressure and temperature evolution at sensor TED1256 and TED1257 versus calculation results

Borehole drainage effect

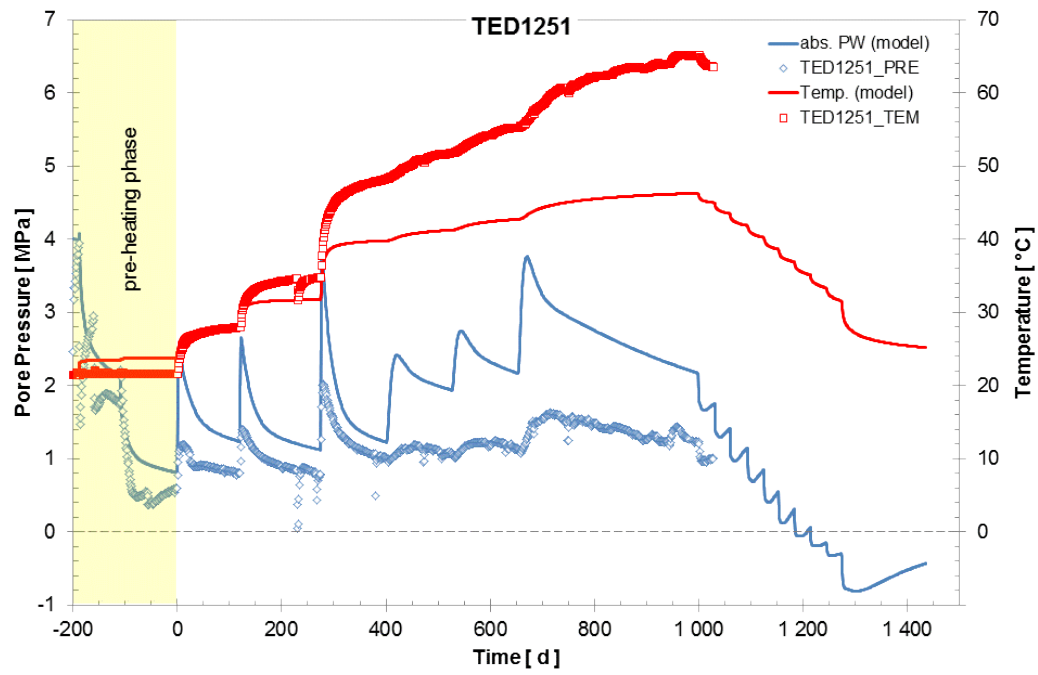
For interpretative modelling of the TED experiment a 3-dimensional approach was used with explicit modelling of the boreholes TED1230 and TED1231, that were used for extensometer measurements and therefore, lead to permanent desaturation of the rock since installation in July 09.

The desaturated part of the rock has a lower thermal conductivity than the saturated one. Therefore, the achieved temperature is higher in TED1251. With respect to the measured data, the results of the calculation do not reflect this behaviour. While the calculation values for pore pressure exceed the measured values by more than 1 MPa, the temperature evolution of the respective sensor is highly underestimated.

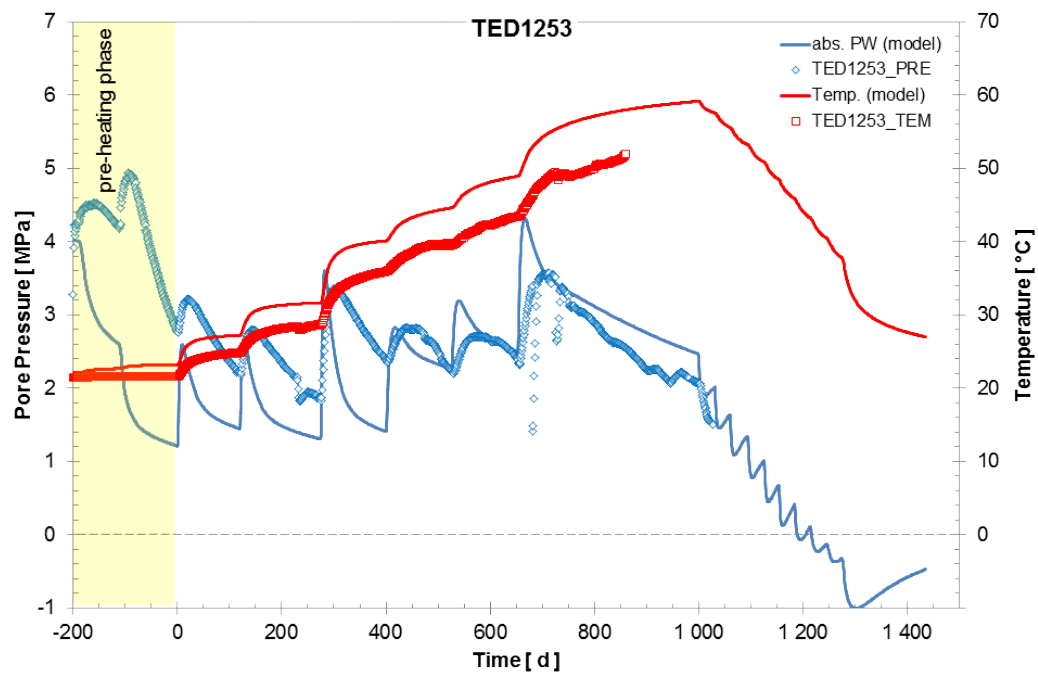
The comparison of measured and calculated values for TED1253 follows the trend of TED1252 showing marginal overestimations.



(a) sensor location



(b) TED1251



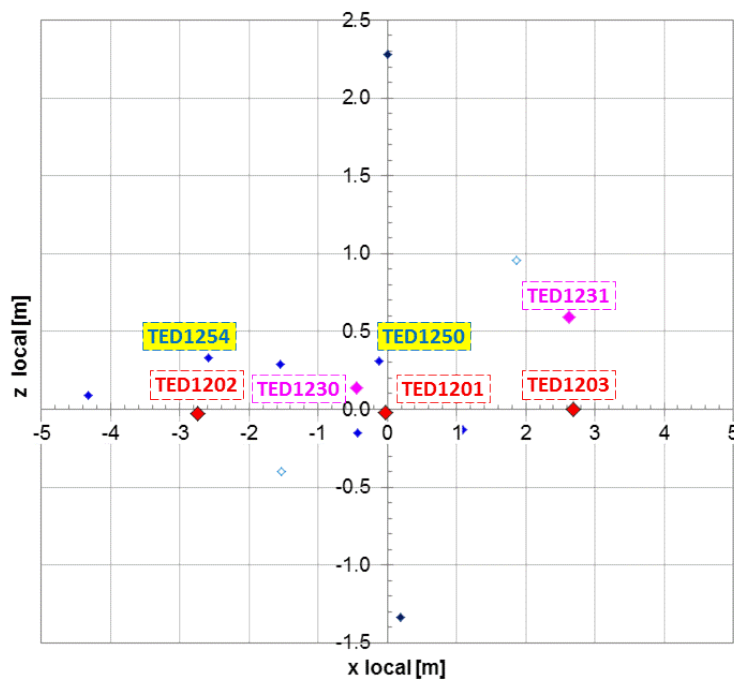
(c) TED1253

Fig. 4.24 Measurement results of absolute pore pressure and temperature evolution at sensor TED1251 and TED1253 versus calculation results

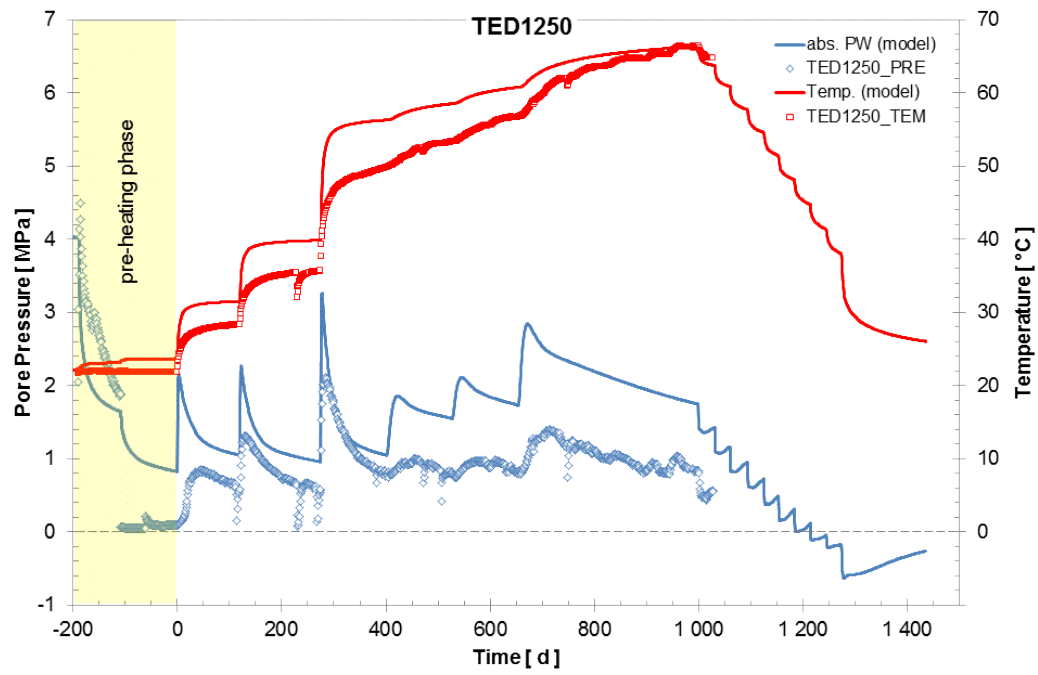
Overestimated thermal loading

In the simulation the sequence for increasing the thermal load at different time steps was done by increasing temperature and not as conducted in reality by increasing power. Therefore, the temperature evolution at TED1202 is overestimated in the modelling, Fig. 4.25. Especially, the calculated values for TED1254 show above-average pore pressure increase, going together with the high thermal load.

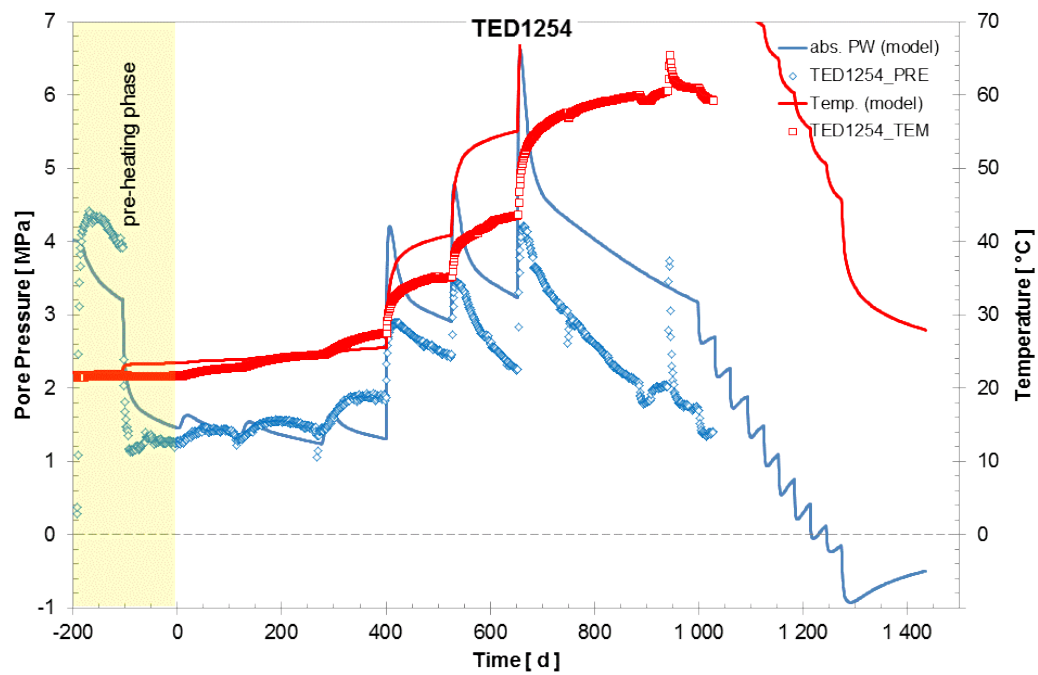
Analogue to the system behaviour of TED1252 and TED1253, TED1250 follows the trend showing marginal overestimations of the respective values for temperature and absolute pore pressures.



(a) sensor location



(b) TED1250



(c) TED1254

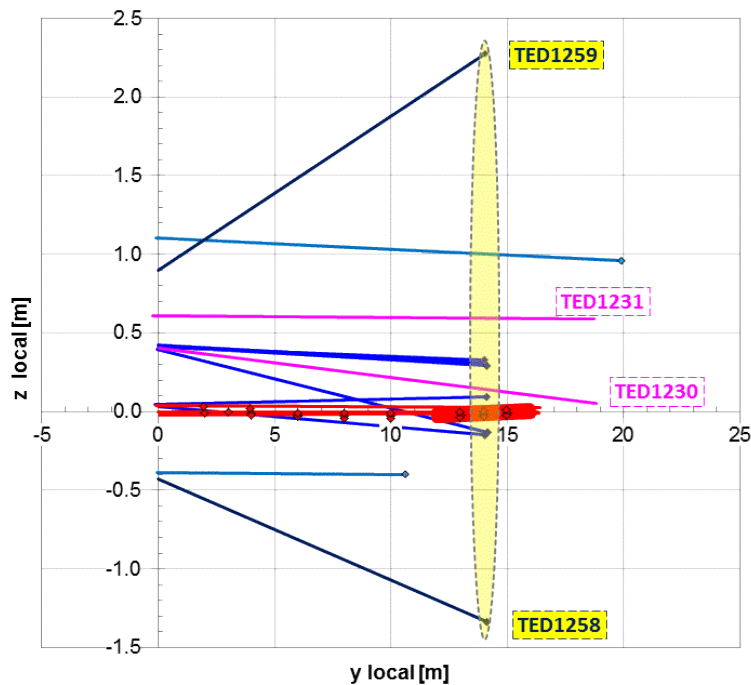
Fig. 4.25 Measurement results of absolute pore pressure and temperature evolution at sensor TED1250 and TED1254 versus calculation results

Anisotropic material behaviour

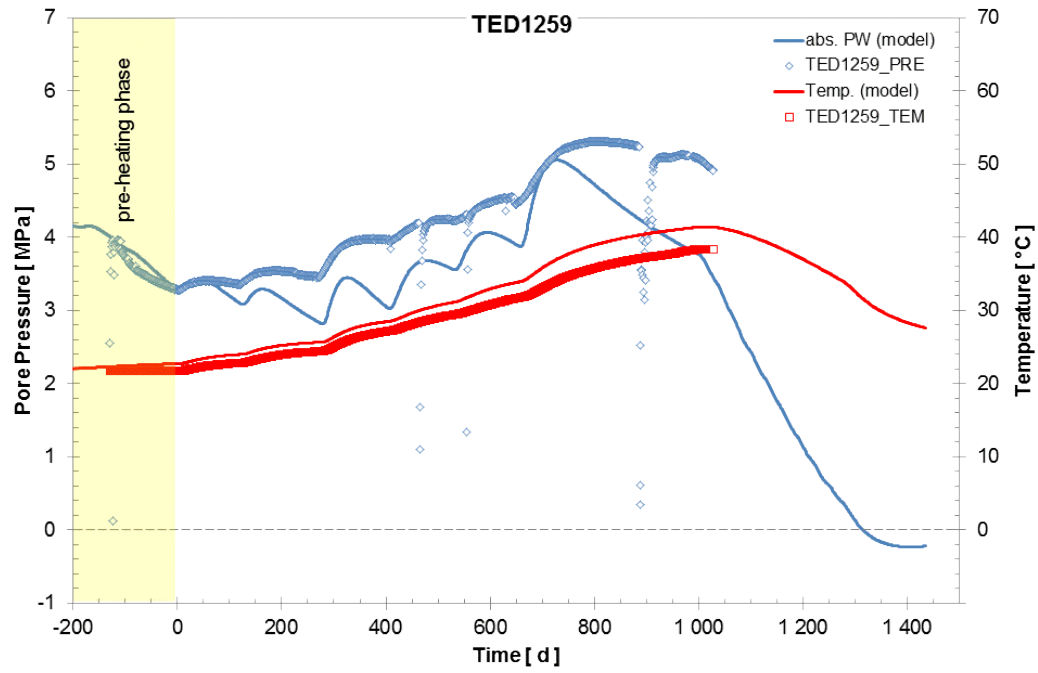
The thermal impact on the COX claystone in relation to the anisotropic material behaviour was experimentally studied and the results are summarized in the related status report /ZHA 2013/. With respect to these results the in situ measurement data have to be evaluated. The anisotropic heat transfer capacity of the rock and its inadequate reproduction with the used modelling approach here, is illustrated by the data set for TED1258 and TED1259 in Fig. 4.26.

The sensor in TED1259 is located more than 2 m above the heater borehole TED1201, which is normal to the bedding planes. While the level of the measured temperature and absolute pore pressure is reached by the calculation values, the time for pore pressure decrease is overestimated in the modelling.

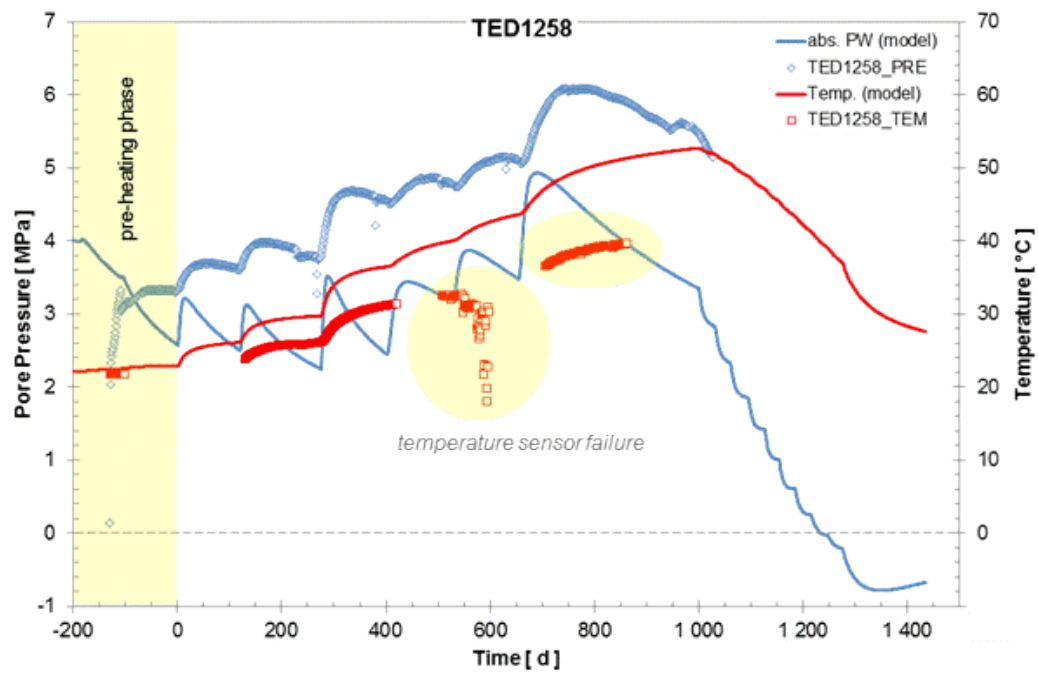
For sensor TED1258 the situation is even worse: The temperature evolution is highly overestimated and the level of absolute pore pressure is underestimated by values of 2 MPa.



(a) sensor location



(b) TED1259



(c) TED1258

Fig. 4.26 Measurement results of absolute pore pressure and temperature evolution at sensor TED1259 and TED1258 versus calculation results (temperature sensor failure after 400 days at TED1258)

4.6 Conclusions drawn from physical modelling and numerical simulation

The simplified hydro-mechanical coupled modelling approach used for numerical simulation of the MB and EZ-G experiments is able to capture the change in pore pressure in general, but derived from the in situ measurement results probably not in its total value. Consequently, interpretative calculations for the TED experiment exhibited the expected shortcomings.

After several exercises in 2-dimensional modelling, the TED experiment was the first time that GRS has used a full 3D model with thermo-hydraulic-mechanical coupling. For simulation purposes the load was applied using a temperature boundary condition. It was difficult to reproduce the reality with temperature loading. In TED experiment the temperatures in the heater boreholes are the results of the power applied (which is constant) and depend a lot on the surrounding environment. The calculations have shown that this coupling effect is not easy to handle (parameter set, varying boundary conditions with time). In fact, we had to use the calculation results from TH-coupled modelling for reporting (without mechanical deformations, instead of the originally planned THM-coupled ones).

Another aspect is that we have used an isotropic approach for modelling the thermal conductivity. For the future an anisotropic approach should be used.

With respect to the long-term time-dependent behaviour the available data is of limited suitability. Therefore, further modelling activities in the frame work of the DM-A experiment focused on this aspect. As a result, it can be stated that pore pressure change is not sufficient to explain the time-dependent deformation of the rock around the borehole, in fact, it plays a rather insignificant role in this configuration. This may be different with other geometries (e. g., open galleries), but for the sealed dilatometer probe borehole pore pressure redistribution is not the major driving force of deformation.

With regard to modelling, additional calculations including viscous deformation and possibly damage are needed. This will require additional work in the field of development of constitutive laws and parameter identification.

5 Summary and conclusions

In the frame of the MB and EZ-G experiments stress redistribution and related pore pressure evolution as a consequence of excavation activities were investigated. Successful measurements were performed, and simplified hydro-mechanical coupled models used for numerical simulation of the MB and EZ-G experiments were able to capture the change in pore pressure in general and especially to explain the initial pore pressure distribution, but showed some deviations from the in situ measurement results. Two mechanisms neglected in the simplified models, viscous deformation and damage, can be offered as explanation for the deviations.

With respect to the long-term time-dependent behaviour the data from MB and EZ-G are of limited suitability. Therefore, the time-dependent deformation of the rock around the borehole has been measured in the frame of the DM-A experiment, which involves long-term measurements with a dilatometer probe installed in a borehole. Additional pore pressure sensors were installed during the course of the experiment. The measurements show that for this configuration, too, viscous deformation or damage is needed to explain the results.

To study the thermo-hydro-mechanical effects of the early thermal phase on the clay host rock, ANDRA has performed an in-situ heating test called TED experiment. The aim of the TED experiment is to measure the evolution of the temperature, deformation and pore pressure field around several heaters and to back-analyse the thermo-hydro-mechanical properties of the rock. Selected measurement results at borehole sensors are shown and compared to calculation results for this purpose. With regard to the previous modelling exercise on Opalinus clay, the COX related calculations exhibited the expected shortcomings.

In order to achieve reliable physical modelling of all these experiments, simulations including viscous deformation and possibly damage are considered necessary. The required additional work in the field of development of constitutive laws and parameter identification is actually in progress in the framework of the extension of the THM-Ton project.

Acknowledgement

The work described in this report was funded by the German Federal Ministry of Economics and Technology (BMWi) under contract number 02 E 10377. The authors would like to thank for the support.

We also would like to thank our colleagues from the Mont Terri Project and from the French Agence Nationale Pour la Gestion de Déchets Radioactifs (ANDRA) for providing the test material and for the fruitful cooperation throughout the entire run time of the experiment.

References

- /AND 05/ ANDRA: DOSSIER (2005): Synthesis – Evaluation of the feasibility of a geological repository in an argillaceous formation
- /AND 06/ ANDRA (2006): Expression of need concerning coupled processes involved in the mechanical behaviour of repository structures, ANDRA internal report -CCCASMG060034
- /AND 09/ ANDRA (2009): Note technique – Localisation des capteurs de temperature et de pression dans les forages peripheriques de l' experimentation TED, DNTAMFS090064
- /BMW 07/ Bundesministerium für Wirtschaft und Technologie (BMWi) – Referat III B 3 und PTKA-WTE (2007): Schwerpunkte zukünftiger FuE-Arbeiten bei der Endlagerung radioaktiver Abfälle (2007 – 2010) – Förderkonzept des Bundesministerium für Wirtschaft und Technologie
- /BOC 08/ Bock, H. (2008): RA Experiment – Updated Review of the Opalinus Clay at the Mont Terri URL based on Laboratory and Field testing. 2008, TR 2008-04
- /BOC 10/ Bock, H., Dehandschutter, B., Martin, C.D., Mazurek, M., Haller, A.D., Skoczylas, F., Davy, C. (2010): Self-Sealing of Fractures in Argillaceous Formations in the Context of Geological Disposal of Radioactive Waste – Review and Synthesis, Clay Club Report, OECD, NEA No. 6184
- /CON 11/ Conil, N., Gatmiri, B., Armand, G.: Expérimentation TED - Analyse à un an de chauffe, Centre de Meuse/Haute-Marne, DRPAMFS0110039, 2011
- /CON 12a/ Conil, N., Armand, G., Garitte, B., Jobmann, M., Jellouli, M., Filippi, M., De La Vaissière, R., Morel, J.: In-situ heating test in Callovo-Oxfordian claystone: Measurement and interpretation. ANDRA 5th international meeting on “Clays in Natural and Engineered Barriers for Radioactive Waste Confinement”, Montpellier, October 22-25, 2012

- /CON 12b/ Conil, N., Morel, J., Armand, G.: Expérimentation TED , Bilan de la deuxième année de chauffe, Centre de Meuse/Haute-Marne, D.RP.AMFS.12.0031, 2012
- /CZA 09/ Czaikowski, O., Lux, K.-H. (2009): Laboratory and modelling research into HM interactions in claystone rock mass. EC-TIMODAZ-THERESA THMC conference, Luxembourg, Sept. 2009
- /CZA 13/ Czaikowski, O., Wieczorek, K. (2013): Identification of potential driving mechanisms for HM coupled time-dependent deformation of argillaceous rocks. *Physics and Chemistry of the Earth*, Vol. 65 (2013), 11-19
- /DAV 03/ Davies, C., Bernier, F. (2003): Impact of the Excavation Disturbed or Damaged Zone (EDZ) on the Performance of Radioactive Waste Geological Repositories. *Proceedings of an European Commission Cluster Conference and Workshop Luxembourg*, 3 to 5 November 2003, EUR 21028 EN
- /DEL 07/ Delay, J., Vinsot, A., Krieguer, J.M., Rebours, H., Armand, G. (2007): Making of the underground scientific experimental programme at Meuse/Haute-Marne underground research laboratory, north eastern France. *Physics and Chemistry of the Earth* 32, 2-18
- /DOP 12/ DOPAS – EC project: Full Scale Demonstration of Plugs and Seals, FP7-Fission-2012, Project number 323273
- /FOR 13/ FORGE –Fate of Repository Gases Project (2013): Gas Generation and Migration, *International Symposium and Workshop*, 5-7 February 2013, Luxembourg
- /LEB 10/ Lebon, P., Landais, P. (2010): On the Way to Siting and Licensing a Deep Disposal: What about the Research Programme on the Callovo-Oxfordian Formation, on the 4th international meeting – Clays in Natural & Engineered Barriers for Radioactive Waste Confinement, Nantes
- /MAD 08/ Madritsch, H. & T. Vietor Mine By Experiment (MB) Excavation history of Niche 2 and results of structural geological tunnel mapping. *Mont Terri Project Technical Note 2010-xx November 2008*

- /MAR 03/ Martin, C.D., Lanyon, G.W., Blümling, P. (2003): Measurement of in-situ stress in weak rocks at Mont Terri Rock Lab. *International Journal of Rock Mechanics and Mining Sciences*, 40, p.1077 – 1088
- /MAZ 08/ Mazurek, M., Gautschi, A., Marschall, P., Vigneron, G., Lebon, P., Delay, J. (2008): Transferability of geoscientific information from various sources (study sites, underground rock laboratories, natural analogues) to support safety cases for radioactive waste repositories in argillaceous formations. *Physics and Chemistry of the Earth*, Vol. 33 (2008), 95-105
- /MIH 10/ Mieke, R., Czaikowski, O., Wieczorek, K. (2010): BET – Barrier Integrity of the Isolating Rock Zone in Clay Formations, Final Report, GRS-261, Gesellschaft für Anlagen- und Reaktorsicherheit (GRS) mbH, August 2010
- /MTP 10/ Mont Terri Project, Work Programme in Phase 16 (July 2010 – June 2011), September 30, 2010
- /NAG 02/ NAGRA (2002): Project Opalinus Clay, Models, Codes and Data for Safety Assessment – Demonstration of disposal feasibility for spent fuel, vitrified high-level waste and long-lived intermediate-level waste
- /OLI 96/ Olivella, S., Gens, A., Carrera, J., Alonso, E.E. (1996): Numerical Formulation for a Simulator (CODE_BRIGHT) for the Coupled Analysis of Saline Media. *Engineering Computations*, 1996, Vol. 13, No 7, pp 87-112
- /SU 07/ Su, K. (2007): Synthesis of the EC MODEX-REP project – Development and Validation of the Constitutive Hydro-mechanical Models for the Callovo-Oxfordian Argillites, FIKW-CT2000-00029
- /TD 06/ Mont Terri Project: Extension of Rock Laboratory – Results and recommendation by rock mechanics analyses group, TD154, 7 Nov. 2006
- /THM 07/ THM-TON Projekt zur Untersuchung der THM-Prozesse im Nahfeld von Endlagern in Tonformationen, GRS – Vorhabensbeschreibung, Juli 2007

- /TSA 05/ Tsang, C.-F. , Bernier, F. (2005): Definitions of excavation disturbed zone and excavation damaged zone, in Davies, C. and Bernier, F. (eds.): Impact of the excavation disturbed zone (EDZ) on the performance of radioactive waste geological repositories, EUR 21028 EN: 5-8, Brussels
- /TSA 12/ Tsang, C.F., Barnichon, J.D., Birkholzer, J., Li, X.L., Liu, H.H., Sillen, X. (2012): Coupled thermo-hydro-mechanical processes in the near field of a high-level radioactive waste repository in clay formations, International Journal of Rock Mechanics & Mining sciences 49, 31-44
- /UPC 02/ UPC (2002): A 3-D program for thermo-hydro-mechanical analysis in geological media
- /VIE 06/ Vietor, T., Blümling, P., Armand, G. (2006): Failure mechanisms of the Opalinus Clay around underground excavations. EUROCK 2006 ISRM regional symposium on multiphysics coupling and long-term behaviour in rock mechanics, May 2006, Liège, Belgium
- /WIE 13/ Wieczorek, K., Czaikowski, O., Zhang, C.-L. (2013): Porewater Pressure and Permeability Measurements during Gallery 08 Excavation. Coupled HM Simulation and Comparison with Pore Pressure Readings. Mont Terri. Technical Note 2010-41/42, November 2013
- /ZHA 04/ Zhang, C.-L., Rothfuchs, T., Moog, H., Dittrich, J., Müller, J. (2004): Thermo-Hydro-Mechanical and Geochemical Behaviour of the Callovo-Oxfordian Argillite and the Opalinus Clay. June 2004, GRS-202, ISBN 3-931995-69-0
- /ZHA 07/ Zhang, C.-L., Rothfuchs, T., Jockwer, N., Wieczorek, K., Dittrich, J., Müller, J., Hartwig, L., Komischke, M. (2007): Thermal Effects on the Opalinus Clay – A Joint Heating Experiment of ANDRA and GRS at the Mont Terri URL (HE-D Project). March 2007, GRS-224, ISBN 978-3-931995-98-0
- /ZHA 08/ Zhang, C.-L., Rothfuchs, T., Dittrich, J., Müller, J. (2008): Investigations on Self-sealing of Indurated Clay. March 2008, GRS-230, ISBN 978-3-939355-04-5

/ZHA 13/ Zhang, C.-L., Czaikowski, O., Rothfuchs, T., Wiczorek, K. (2013): Thermo-Hydro-Mechanical Processes in the Nearfield around a HLW Repository in Argillaceous Formations (THM-Ton), FKZ 02E10377, Volume I: Laboratory Investigations. Report for phase I from 05.2007 to 05.2013. Gesellschaft für Anlagen- und Reaktorsicherheit (GRS) mbH, June 2013

List of tables

Tab. 3.1	Basic mechanical characteristics of the different geological zones of the Callovo-Oxfordian formation /AND 05/, /SU 07/	47
Tab. 4.1	Physical properties determined Opalinus (OPA) clay and for Callovo-Oxfordian (COX) clay.....	70
Tab. 4.2	Hydraulic parameters determined Opalinus (OPA) clay and for Callovo-Oxfordian (COX) clay, associated with the constitutive equations	70
Tab. 4.3	Mechanical parameters determined for Opalinus (OPA) clay and for Callovo-Oxfordian (COX) clay, associated with the constitutive equations	71

List of figures

Fig. 1.1	Coupled THM processes in the nearfield around a HLW disposal borehole	2
Fig. 2.1	Mont Terri motorway tunnel and location of the Mont Terri Rock Laboratory (left centre of the picture)	9
Fig. 2.2	Geological profile along the motorway tunnel showing the location of the Mont Terri Rock Laboratory	10
Fig. 2.3	Geometry of the Mont Terri Rock Laboratory, perspective view /MTP 10/, showing the location of the MB, EZ-G and DM-A experimental sites (MB preceding pore water pressure measurements were performed during Gallery 08 excavation).....	11
Fig. 2.4	Geological map of the Mont Terri Rock Laboratory with location of main boreholes /MTP 10/ showing the location of the MB, EZ-G and DM-A experimental sites.....	11
Fig. 2.5	Perspective view of the MTRL showing the locations of the four long PWP boreholes drilled from the HE-E niche (yellow: existing galleries, pink: planned Gallery 08 with niches).....	13
Fig. 2.6	Sliding-end minipackers used for the PWP measurements in the long boreholes during Gallery 08 excavation	13
Fig. 2.7	Pressure recordings of BMB 1 – BMB 4.....	15
Fig. 2.8	Temperature recordings of BMB 1 – BMB 4.....	16
Fig. 2.9	Pressure evolution at BMB 1 and BMB 2 during Gallery 08 excavation, together with excavation progress.....	17
Fig. 2.10	Excavation sequence and support installation	20
Fig. 2.11	Typical configuration of the MB support system.....	20

Fig. 2.12	Plan view of Mine-by Niche showing the layout of the instrumentation.....	21
Fig. 2.13	Example of the excavation-induced fractures, /MAD 10/ (observed during the excavation of Gallery08 as well as in the face of niche excavation; but perpendicular to the tunnel axis)	22
Fig. 2.14	Pore pressure response and excavation advance over time /VIE 10/.....	23
Fig. 2.15	Pore pressure response related to excavation advance /VIE 10/	23
Fig. 2.16	Radial extensometer response normal to bedding at BMB-30 related to excavation advance /VIE 10/.....	25
Fig. 2.17	Radial extensometer response sub-parallel to bedding at BMB-28 related to excavation advance /VIE 10/.....	25
Fig. 2.18	Reverse head extensometer response related to excavation advance /VIE 10/.....	26
Fig. 2.19	Magnetic head extensometer response related to excavation advance /VIE 10/.....	27
Fig. 2.20	Chain inclinometer response related to excavation advance (inclination changes converted into vertical displacements) /VIE 10/	29
Fig. 2.21	Chain inclinometer response related to excavation advance - Symmetric evolution of angular strain in segments near entrance /VIE 10/.....	29
Fig. 2.22	EZ-G test site showing the pore pressure measurement boreholes (yellow: existing galleries, pink: planned Gallery 08 with niches).....	31
Fig. 2.23	Orientation of boreholes for pore pressure measurement	32
Fig. 2.24	GRS minipiezometer for pore pressure measurement	32
Fig. 2.25	Early pressure evolution in the test intervals: equilibration phase and water injection testing	34

Fig. 2.26	Measured pressure data and WELTEST fit for the shut-in phase of the injection test at EZ-G6	34
Fig. 2.27	Pressure evolution in the test intervals over the complete monitoring period	35
Fig. 2.28	Pressure evolution in the test intervals during excavation of the last 43 m of Gallery 08, together with excavation progress.....	36
Fig. 2.29	Temperature evolution in the test intervals during excavation of the last 43 m of Gallery 08, together with excavation progress	37
Fig. 2.30	Installation process of the borehole dilatometer on-site (above) and the schematic sketch of the probe (left: longitudinal view showing the packer and the temperature/humidity sensors, right: cross section showing the orientation of the deformation sensors, hatching = bedding plane position).....	39
Fig. 2.31	Packer pressure tests on July 15 th and 16 th , 2009 and response of the borehole deformation sensors.....	40
Fig. 2.32	Experimental results of the dilatometer probe: (a) packer pressure (above) and borehole deformation (below) as well as (b) relative humidity (above) and temperature (below); Experimental results of the minipiezometer in DM-A (B01-03) in (c) pore-water pressure.....	41
Fig. 2.33	Sketch of the geometrical boundary conditions of (a) the new boreholes DM-A (B01-03) and (b) the orientation of the bedding planes.....	43
Fig. 3.1	Geological cross section of the Meuse/Haute Marne site /AND 05/	45
Fig. 3.2	Mineralogy of the Callovo-Oxfordian argillaceous formation /AND 05/	46
Fig. 3.3	Geomechanical properties of the Callovo-Oxfordian argillaceous formation /SU 07/.....	46

Fig. 3.4	Layout of the TED heating experiment with three heaters installed in horizontal boreholes showing also the measuring boreholes /AND 09/	49
Fig. 3.5	TED heating procedure /CON 12a/	50
Fig. 3.6	TED heating boreholes and boreholes for measurement of temperature, pore pressure and deformation	51
Fig. 3.7	In-situ measurement data for temperature evolution at heating borehole TED1201.....	52
Fig. 3.8	In-situ measurement data for temperature evolution at heating borehole TED1202 (sensor failure during second thermal load level)	53
Fig. 3.9	In-situ measurement data for temperature evolution at heating borehole TED1203.....	53
Fig. 3.10	In-situ measurement data for temperature evolution at borehole TED1219 (parallel to heating borehole TED1201).....	54
Fig. 3.11	In-situ measurement data for temperature evolution at borehole TED1210 (perpendicular to heating borehole TED1201).....	54
Fig. 3.12	In-situ measurement data for temperature evolution at borehole TED1215 (parallel to heating borehole TED1201).....	55
Fig. 3.13	In-situ measurement data for temperature evolution at borehole TED1213 (perpendicular to heating borehole TED1201).....	55
Fig. 3.14	In-situ measurement data for temperature evolution at borehole TED1217 (parallel to heating borehole TED1202).....	56
Fig. 3.15	In-situ measurement data for temperature evolution at borehole TED1216 (parallel to heating borehole TED1203).....	56
Fig. 3.16	In-situ measurement data for pore pressure/temperature evolution at borehole TED1251 (parallel to heating borehole TED1201).....	57

Fig. 3.17	In-situ measurement data for pore pressure/temperature evolution at borehole TED1250 (perpendicular to heating borehole TED1201).....	57
Fig. 3.18	TED1252 data	58
Fig. 3.19	TED1253 data	58
Fig. 3.20	TED1254 data	58
Fig. 3.21	TED1255 data	58
Fig. 3.22	TED1256 data	58
Fig. 3.23	TED1257 data	58
Fig. 3.24	TED1258 data	58
Fig. 3.25	TED1259 data	58
Fig. 3.26	In-situ measurement data for absolute pore pressure/temperature evolution at borehole TED1240 (parallel to heating borehole TED1203)	59
Fig. 3.27	In-situ measurement data for pore pressure increase at borehole TED1240 due to temperature evolution (effective data)	59
Fig. 3.28	In-situ measurement data for absolute pore pressure/temperature evolution at borehole TED1241 (parallel to heating borehole TED1202)	60
Fig. 3.29	In-situ measurement data for pore pressure increase at borehole TED1241 due to temperature evolution (effective data)	60
Fig. 4.1	FE model (3D) used for numerical simulation of the Mine-by test (left: full model, right: excavation steps)	72
Fig. 4.2	Excavation process.....	73

Fig. 4.3	Pore pressure propagation as a result of hydro-mechanical coupled numerical simulation after excavation (left: full model, right: detailed view)	74
Fig. 4.4	Selected measurement results of pore pressure evolution in BMB-15 sensor I4 and I5 versus simulation results (dotted lines)	75
Fig. 4.5	Measurement results of pore pressure evolution in BMB-15 sensor I1 – I3 versus simulation results (dotted lines)	75
Fig. 4.6	FE models used for numerical simulation of the EZ-G experiment (left: 2D model, right: 3D model,)	77
Fig. 4.7	Details of the 3D model, showing the gallery geometry and the individual excavation steps	77
Fig. 4.8	Measurement results of pore pressure evolution at BEZ-G6/7/8 versus simulation results (dotted lines, 2D) – pre-excavation phase	78
Fig. 4.9	Pore pressure propagation as a result of 3-dimensional hydro-mechanical coupled numerical simulation (2 nd July 2004, 1 st July 2008 and 11 th July 2008)	80
Fig. 4.10	Pore pressure propagation as a result of 3-dimensional hydro-mechanical coupled numerical simulation (30 th July 2008, 5 th August 2008 and 26 th August 2008).....	81
Fig. 4.11	Measurement results of pore pressure evolution in BEZ-G6 & 7 versus simulation results (dotted lines, 3D) – Ga08 excavation phase.....	82
Fig. 4.12	Measurement results of pore pressure evolution in BEZ-G8 versus simulation results (dotted lines, 3D) – Ga08 excavation phase	83
Fig. 4.13	FE model (2D) used for numerical simulation of long-term borehole deformation (right: full model, left: detail)	84

Fig. 4.14	Negative pore pressure propagation as a result of hydro-mechanical coupled numerical simulation for the sensor reference measurements on June 23 rd , 2009 (above) and for the end of March 2010 (below)	85
Fig. 4.15	Calculation results in a horizontal cross section – total pore pressure values (small scale) and the resulting pore pressure deviation values with respect to sensor reference measurement	86
Fig. 4.16	Calculation results of the selected element on time-dependent principal stress and pore pressure deviation during and after borehole excavation and sensor installation	87
Fig. 4.17	Calculation results on time-dependent borehole contour deformation due to pore pressure redistribution	88
Fig. 4.18	Average borehole deformation rates – experimental findings vs. calculation results	89
Fig. 4.19	FE model used for numerical simulation of the TED experiment (3D model)	92
Fig. 4.20	Sensor location at the heating boreholes of the TED experiment (top view)	93
Fig. 4.21	Selected measurement results of temperature evolution versus simulation results (dotted lines).....	94
Fig. 4.22	Measurement results of absolute pore pressure and temperature evolution at sensor TED1252 and TED1255 versus calculation results....	96
Fig. 4.23	Measurement results of absolute pore pressure and temperature evolution at sensor TED1256 and TED1257 versus calculation results....	98
Fig. 4.24	Measurement results of absolute pore pressure and temperature evolution at sensor TED1251 and TED1253 versus calculation results..	100

Fig. 4.25	Measurement results of absolute pore pressure and temperature evolution at sensor TED1250 and TED1254 versus calculation results..	102
Fig. 4.26	Measurement results of absolute pore pressure and temperature evolution at sensor TED1259 and TED1258 versus calculation results (temperature sensor failure after 400 days at TED1258).....	104

**Gesellschaft für Anlagen-
und Reaktorsicherheit
(GRS) mbH**

Schwertnergasse 1
50667 Köln

Telefon +49 221 2068-0

Telefax +49 221 2068-888

Forschungszentrum

85748 Garching b. München

Telefon +49 89 32004-0

Telefax +49 89 32004-300

Kurfürstendamm 200

10719 Berlin

Telefon +49 30 88589-0

Telefax +49 30 88589-111

Theodor-Heuss-Straße 4

38122 Braunschweig

Telefon +49 531 8012-0

Telefax +49 531 8012-200

www.grs.de

ISBN 978-3-939355-92-2